2017

SPARSE SAMPLING AND ARRAY IN SIGNAL PROCESSING

Na Wu

SPARSE SAMPLING AND ARRAY IN SIGNAL PROCESSING

by

NA WU

Presented to the Faculty of the Graduate School of

The University of Texas at Arlington in Partial Fulfillment

of the Requirements

for the Degree of

DOCTOR OF PHILOSOPHY

THE UNIVERSITY OF TEXAS AT ARLINGTON

May 2017

ACKNOWLEDGEMENTS

Firstly, I would like to thank my supervisor, Dr. Qilian Liang, for constantly motivating and encouraging me, and also for his invaluable advice during the course of my doctoral studies. During these years, he spends a lot of time helping me with research problems and also teaches me the truth of life. His enthusiasm and attitude toward research have deeply influenced me and helped me to do better research.

Besides, I want to thank the faculty members in Electrical Engineering at UTA for the contribute they make to this department. In particular, I want to express my gratitude to Dr. Jonathan Bredow, Dr. Ioannis Schizas, Dr. Jean Gao, Dr. Alice Sun for taking time to serve in my proposal committee.

I am grateful to all the teachers who taught me during the years I spent in school, first in China, then in UT Arlington in the Unites States. I would like to thank Dr. Schizas for teaching me digital communications and estimation theory. Also my acknowledgment to Dr. Peter Wang, who taught me wireless communications and Dora for teaching me information theory. I also want to thank my colleagues and visiting scholars in our lab: Ji Wu, Junjie Chen, Zhuo Li, Xin Wang, Qiong Wu, Ishrat Maherin, Shitong Yuan, Hao Liang, Ganlin Zhao, Dr. Rui Min, Yingxi Zheng. I'm so lucky to learn a lot of things from you!

Last but not least, I would like to express my deep gratitude to my family. My parents always unconditionally support my decisions and sponsored my undergradu-

ate and graduate studies. My husband Hai Huang keeps encouraging and inspiring me to pursue graduate studies. I also thank several of my friends who have helped me throughout my career.

This work was supported in part by U.S. Office of Naval Research (ONR) under Grant N00014-13-1-0043 and National Science Foundation (NSF) under Grant CNS-1247848.

April 19, 2017

ABSTRACT

SPARSE SAMPLING AND ARRAY IN SIGNAL PROCESSING

Na Wu, Ph.D.

The University of Texas at Arlington, 2017

Supervising Professor: Qilian Liang

Sparse sampling and sparse arrays have attracted lots of interests in recent years. In this dissertation, we firstly apply nested sampling and co-prime sampling to ultra-wideband radar, which require us to extend the algorithms from stationary signals to non-stationary signals. After that, the synthetic aperture radar data is compressed through singular-value QR-decomposition algorithm.

The dissertation also proposes an approach to turn low resolution images into high resolution (HR) images. We extend co-prime sampling structure to interpolation in order to improve the resolution of reconstructed images through compressive sensing (CS). Compared to the direct CS method and conventional interpolation method, the new co-prime interpolated compressive sensing (CopCS) approach could tremendously reduce the RMSE and improve the PSNR. Besides, in high compression ratio scenario, CS exhibits a poor resolution due to the included black dots, while CopCS can recover the image without introducing dots. Moreover, we also test CopCS approach on the Greenland bed elevation raw data set (very sparse sampled).

In addition, the augmented matrix approach from the minimum redundancy array (MRA) is extended to the sparse arrays – nested array and co-prime array for

direction-of-arrival estimation. Especially when the background of the system model is in underwater environment and the sensors are considered as moving passive sonars. Numerical examples of how to construct these new structures of the non-uniform array are elaborated.

Moreover, as sparse arrays cost fewer elements, two sparse cylindrical arrays are proposed in this dissertation. According to the characteristic of cylindrical array, it can be seen as a linear array whose elements are the identical circular arrays. Therefore the co-prime linear array and nested linear array could be combined with circular arrays. Based on the beam pattern of uniform cylindrical array, 1D and 2D beam pattern of co-prime cylindrical array and nested cylindrical array are derived respectively. Besides, when more than one sources are coming from arriving directions, the performance of sparse arrays are analyzed and compared. The new proposed sparse cylindrical arrays not only reduce the number of elements, but also improves the resolution in comparison with an equal length uniform cylindrical array. Since in massive MIMO, antennas at the base station usually scale up greater than 100, the performance of the sparse cylindrical arrays in massive MIMO scenario is analyzed. Three modified structures of sparse cylindrical antenna array are proposed. As it shows in the examples, when channel capacity is unchanged, sparse cylindrical array could save about 30% of real antennas by calculating the virtual antennas via difference co-array.

TABLE OF CONTENTS

LIST OF ILLUSTRATIONS

LIST OF TABLES

CHAPTER 1

Introduction

Radar target detection often needs to process a great amount of data. In principle, if the signal can be recovered after down sampling, the sampling rate should be larger than the Nyquist sampling rate. However, Nyquist sampling is less efficient in the background of big data. As a consequence, sub-Nyquist sampling has been studied for many years, because it can reduce the complexity and cost of computation significantly. Here we consider two types of radars, one is ultra-wideband (UWB) radar and the other one is synthetic aperture radar (SAR). UWB radar has been employed in foliage environment because of the exception range resolution coupled with penetrating capability and low power [1][2]. Target detection in forest environment attracted a lot of interest since it not only benefits military area, but also helps the detection in other scenarios, such as sense-through-wall. In existing works of UWB radar detection of targets in foliage, [3] and [4] applied two methods, in the aspect of frequency domain and time domain respectively. Synthetic aperture radar (SAR) is an on-board radar system that can provide high-resolution images for remote objectives even in a bad weather situation. The research of SAR is mainly focused on image and target recognition algorithm. There are several different strategies to reduce the capacity of the data. The author in [5] compared different algorithms for on-board SAR raw data reduction. In [6], Gabor transform is proposed for SAR image compression and in [7][8], compressive sensing (CS) algorithms are applied. Xia [9] and Li et al [10], used co-prime sampling for estimating multiple frequencies and imaging of moving targets with SAR.

High resolution (HR) image is highly desirable in many areas, such as graphic applications and image processing. The advantage of HR image is that it can provide more details with a high pixel density. This is very critical and helpful in medical diagnosis or pattern recognition. Nevertheless, the resolution is often limited in practical by various reasons, like bad weather condition and outdated hardware. Although a lot of research has been studied on CS [11]-[13], none of it is on bed map resolution improvement. The bed elevation and basal conditions of the Greenland and Antarctic ice sheets are important to numerical modeling of these ice sheets, but its difficult to collect data over these large ice sheets with airborne radars to generate a high resolution bed map. Furthermore, processing with a large number of data sets would be a major problem. Co-prime sampling is usually applied in under-sampling process and calculating correlation, while there is another property of co-prime sampling – orthogonality, which could be used to complementary combine two co-prime images [14].

Underwater source localization has received lots of research interests since it plays an important role in military intelligence, navigation and ocean exploitation. The design purpose is to detect more targets through fewer sensors. [15] introduces the minimum redundancy array (MRA), which can reduce the number of redundant sensors present in the array. Besides, the author in [16][17] proposes two new structures of non-uniform arrays – nested array and co-prime array. Direction of arrival (DoA) estimation has been studied over 1D, 2D and multiple dimensional arrays [18]-[20]. Design of the array involves trade-offs among the geometry and the number of sensors. High resolution of the array needs large aperture while keeping the spacing of the sensors less than half-wavelength. How to successfully detect all the sources in underwater scenario with less sensors is still an open question. Furthermore, the array sometimes is placed on a moving platform, such as autonomous underwater vehicle

(AUV). In order to minimize the number of physical sensors on the moving platform, an algorithm based on space-domain sensor synthesis (SDS) is proposed. Considering the phase shift in the signal, a gradient descent algorithm is applied before SDS algorithm.

Conformal arrays are valuable in many applications, such as underwater sonar arrays and antenna arrays in wireless communication systems. Conforming the array to the surface not only saves the space, but also makes the elements less visually intrusive by integrating it into existing objects. Cylindrical array is one type of conformal arrays. A cylindrical array contains of elements in three directions and this provides wide cover in both the azimuth plane and the elevation plane, so it's widely used in wireless communication. One big difference between conformal array and traditional array is that the beam pattern can not be obtained by the product of array factor and element pattern. However, since the cylindrical array consists of a series of identical circular arrays, the whole array can be seen as a linear array whose elements are these identical circular arrays. How to design antenna arrays plays an important role in wireless communications, especially when there're hundreds of antennas at the transmitter. In massive MIMO, if the number of antennas and RF chains are increasing, the channel capacity and transmission efficiency could be obviously improved as well. Since in massive MIMO, antennas at the base station (BS) usually scale up greater than 100, the complexity and hardware requirement of the system are also increased. Many studies in massive MIMO are focused on the analysis of channel capacity, precoding and etc, few are about the sparse antenna array deployment. Based on the sparse linear array structures as indicated by previous literatures, three new arrays namely co-prime cylindrical array (CCA), nested cylindrical array (NCA) and sparse nested cylindrical array (SNCA) are proposed. Compared to the traditional uniform

cylindrical array (UCA), the proposed arrays vastly reduce the number of antennas used at the BS.

1.1 Preliminaries to sparse sampling

1.1.1 Nested sampling

Nested sampling has been applied in beam-forming and DoA [16], which is obtained by down sampling a set of data using two or more uniform linear arrays. This structure can generate N^2 degrees of freedom with N physical sensors. For a two-level nested sampling of $x_c(t)$, the level 1 samples and level 2 samples are separately located at N_1 and N_2, and satisfy

$$1 \leq l \leq N_1 \tag{1.1}$$

$$(N_1 + 1)m, \quad 1 \leq m \leq N_2 \tag{1.2}$$

In Figure 1.1, we give an example of two-level nested sampling.

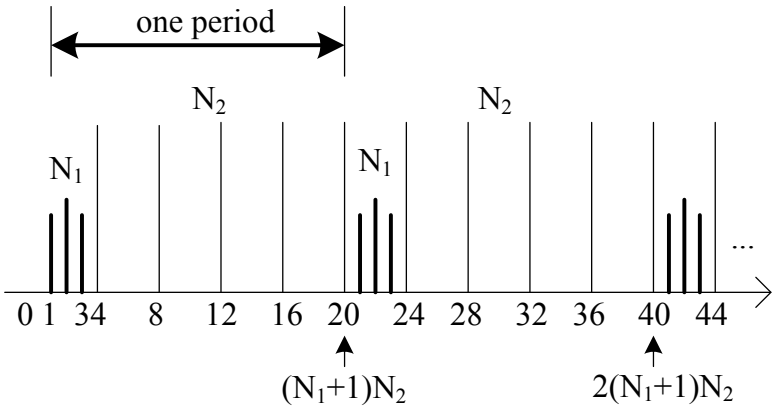

Figure 1.1. two-level nested sampling with $N_1 = 3, N_2 = 5$.

For simplicity of describing nested sampling, several properties of nested sampling are concluded as follows:

Property 1. *Given the cross-difference* $k_n = (N_1+1)m-l,\ 1 \leq m \leq N_2, 1 \leq l \leq N_1$, *the range of cross-differences lies in* $-[(N_1+1)N_2-1] \leq k_n \leq [(N_1+1)N_2-1]$.

Property 2. *There are some 'holes' in the range of cross-difference, such as* $(N_1+1), 2(N_1+1), ..., (N_2-1)(N_1+1)$, *which can be calculated by self differences* $(N_1+1)(m_1-m_2),\ 1 \leq m_1, m_2 \leq N_2$.

Property 3. *For spatially wide sense stationary signal, the correlation at all lags before nested sampling will be equal to that after nested sampling. If the signal is non-stationary, for a small period, this equality still holds.*

The proofs of property 1 and 2 can be referred in [17], and property 3 is derived from the theory of Short-time Fourier transform (STFT).

The period of nested sampling is represented as $(N_1+1)N_2$, for example, $N_1 = 3$ and $N_2 = 5$. It means that in each period, there are 20 values which are indicated by 8 numbers. The average sampling rate is

$$f_s = \frac{N_1+N_2}{(N_1+1)N_2} \approx \frac{1}{N_1} + \frac{1}{N_2} \tag{1.3}$$

With the increasing of N_1 and N_2, the sampling rate will be smaller than the Nyquist sampling, thus causing nested sampling a Sub-Nyquist sampling.

1.1.2 Co-prime sampling

Different from nested sampling, co-prime sampling deals with a set of data into two sets of uniformly spaced samplers MT and NT, where M and N must be mutual co-prime numbers. Co-array can also generate MN freedoms with $M+N$ sensors. The instance is shown in Figure 1.2. After co-prime sampling, the WSS signal $x_c(t)$ is divided into:

$$\begin{aligned} x_c(t) &= x(Mn) \\ x_c(t) &= x(Nn) \end{aligned} \tag{1.4}$$

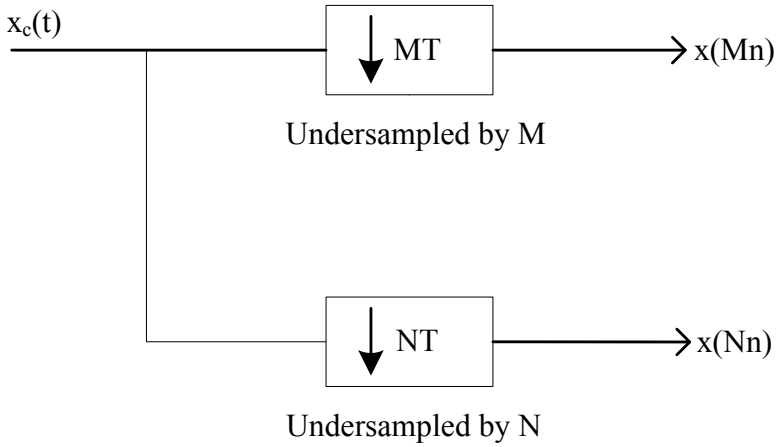

Figure 1.2. Co-prime sampling in the time domain using M, N.

and the difference between two sets is

$$k_c = Mn_1 - Nn_2 \tag{1.5}$$

which is defined as difference co-array.

From [17], we know that the range of k_c should be between

$$-MN + 1 \leq k_c \leq MN - 1 \tag{1.6}$$

There are also several properties of co-prime sampling:

Property 4. *If* $0 \leq n_1 \leq N-1$ *and* $0 \leq n_2 \leq M-1$, *then* $x(n_1, n_2) = Mn_1 - Nn_2$ *can achieve* MN *distinct values in the previous range of* k_c.

Property 5. *There are 'holes' in the difference co-array. In order to generate full range of* $[-MN+1, MN-1]$, *the ranges of* n_1 *and* n_2 *are defined as* $0 \leq n_1 \leq N-1$, $-M+1 \leq n_2 \leq M-1$, *and the self-difference* $Mi_1 - Mi_2$, $Ni_1' - Ni_2'$ *are considered.*

The average sampling rate of co-prime sampling is

$$f_s = \frac{M+N}{MN} \approx \frac{1}{M} + \frac{1}{N} \tag{1.7}$$

when $T = 1$.

1.2 Preliminaries to sparse arrays

1.2.1 One-dimensional nested array and co-prime array

Nested linear array is constructed by a nested pair (N_1, N_2), where the sensors are placed with two-level density, and level 1 has N_1 sensors, level 2 has N_2 sensors [16],

$$\begin{aligned} & 1 \leq l_1 \leq N_1 \\ & (N_1+1)l_2, \quad 1 \leq l_2 \leq N_2 \end{aligned} \tag{1.8}$$

The difference co-array of the 1D nested array is defined as

$$d_n = (N_1+1)l_2 - l_1, 1 \leq l_1 \leq N_1, 1 \leq l_2 \leq N_2 \tag{1.9}$$

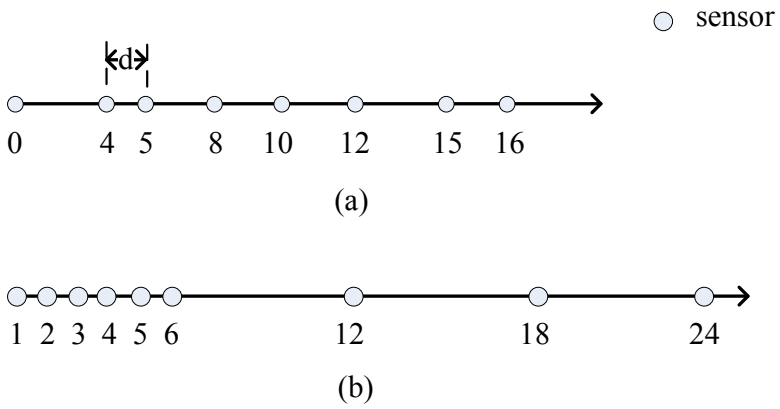

Figure 1.3. Example of co-prime linear array and nested linear array, (a) co-prime pair $(4, 5)$, (b) nested pair $(5, 4)$. .

Co-prime linear array interleaves two uniform subarrays which are sampled by two prime integers P, Q, and the locations of the elements are in set $\mathbf{K} = \{\mathbf{K}_1, \mathbf{K}_2\}$, where

$$\mathbf{K}_1 = \{0, Q, 2Q, 3Q, \ldots, (P-1) \times Q\}$$
$$\mathbf{K}_2 = \{0, P, 2P, 3P, \ldots, (Q-1) \times P\} \tag{1.10}$$

While in a co-prime array, if the two prime numbers are (P, Q), the difference co-array is

$$d_c = Pn_1 - Qn_2, 0 \leq n_1 \leq Q-1, 0 \leq n_2 \leq P-1 \tag{1.11}$$

In Figure 1.3(a), it plots an example of co-prime linear array with co-prime integers $(4, 5)$, and in Figure 1.4(b), it shows the example of nested linear array with pair $(5, 4)$.

1.2.2 Two-dimensional Nested Array

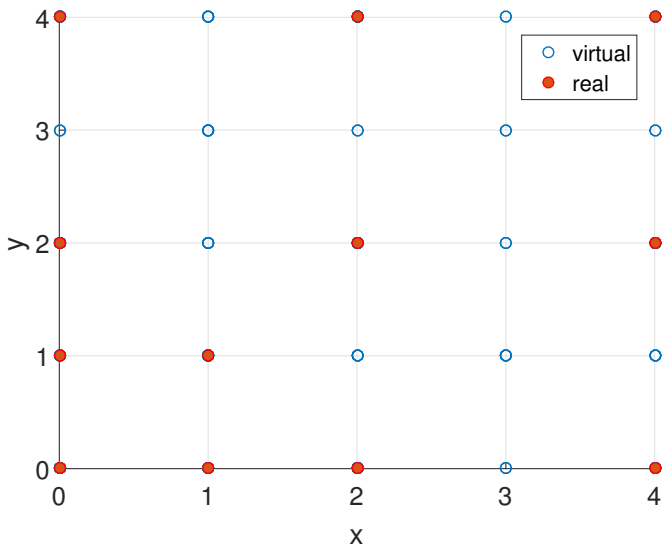

Figure 1.4. Example of two-dimensional nested array .

In this work, the multiple dimensional sparse cylindrical array is built similarly to the rectangular nested array. As a consequence, the definition of the 2D nested array is provided here.

Definition 1. *2D nested array [18]: A two-dimensional nested array consists of a dense array and a sparse array, which are described by a random generated* 2×2 *nonsingular matrix* $\boldsymbol{N}^{(d)}$*, an integer matrix* $\boldsymbol{P}$*, the number of elements in sparse array is* $N^{(s)}$ *and in dense array is* $N^{(d)} = det(\boldsymbol{P})$*.*

(1) The sensor locations in dense array is generated by $\{\boldsymbol{N}^{(d)}\boldsymbol{n}^{(d)}, \boldsymbol{n}^{(d)} \in FPD(\boldsymbol{P})\}$*.* FPD *is the fundamental parallelepiped.*

(2) The sensor locations in sparse array is $\boldsymbol{N^{(s)}}[m_1\ m_2]^T$*, with* m_1, m_2 *in the range* $[0, N_1^{(s)}]$*,* $[0, N_2^{(s)}]$ *respectively and* $N_1^{(s)}N_2^{(s)} = N^{(s)}$*.*

For example, let $\boldsymbol{N^{(d)}} = \begin{pmatrix} 1 & 0 \\ 0 & 1 \end{pmatrix}$, $\boldsymbol{P} = \begin{pmatrix} 2 & 0 \\ 0 & 2 \end{pmatrix}$, $N_1^{(s)} = 3$, $N_2^{(s)} = 3$. We illustrates this 2D nested array in Figure 1.4. There're 12 real sensors which are plotted in red dots and 13 virtual sensors in blue dots.

1.3 Organization

The rest of this dissertation is organized as follows:

Chapter 2 implements sparse sampling and singular-value-QR decomposition to compress the UWB radar data and SAR data. Chapter 3 extends co-prime sampling structure to interpolation in order to improve the resolution of Greenland bed map. In Chapter 4, 1D and 2D sparse arrays are applied in underwater DoA detection. Then in Chapter 5, the moving 1D co-prime sensor array based on the proposed space-domain sensor synthesis is studied. In Chapter 6, we evaluate spatial resolution and channel capacity of sparse cylindrical arrays for massive MIMO. Finally, some future work is provided in Chapter 7.

CHAPTER 2

Data Compression for UWB Radar and SAR

2.1 Introduction

Big data is a hot topic recently, and due to its large size, data compression becomes very important. However, data compression will cause a loss of information and affect the resolution of the radar image. Sub-Nyquist sampling has been studied for many years, because it can reduce the complexity and cost of computation significantly. Recently, a new sub-Nyquist sampling algorithm mentioned in [16] is systematically nesting two or more uniform linear arrays and [17] proposed co-prime sampling afterward. One advantage of nested sampling and co-prime sampling is that wide-sense stationary (WSS) signals sampled by these two sub-Nyquist sampling algorithms can keep the same second-order statistics and achieve enhanced degrees of freedom. Because of its property in second-order statistics, we want to prove these under-sampling methods would be helpful for detecting target in foliage environment. Another data reduction method, singular-value decomposition-QR (SVD-QR) algorithm is proposed in [21]. SVD-QR algorithm has been used in reducing the redundancy of wireless sensor network [22][23] for its advantage of low complexity. SVD-QR selects several independent data sets which minimize the residual error in a least-square sense. In wireless sensor networks, since the sensors are densely deployed and the information collected among adjacent sensor nodes is possible alike with each other, this approach can be very efficient. The SAR images formed from the phase histories are also spatially overlapped, taking advantage of this property, we apply SVD-QR method in synthetic aperture radar in a similar way.

This chapter is organized as follows. Section 2.2 and section 2.3 gives a brief overview of the implementation of ultra-wideband rada (UWB) and the basic concepts of SVD-QR algorithm respectively. In section 2.4, we apply the data compression algorithm in two types of radars, in which section 2.4.1 shows the nested sampling and co-prime sampling in sense-through-foliage target detection and Section 2.4.2 provides raw data reduction for SAR based on SVD-QR method. Section 2.5 summarizes the results.

2.2 Implementation in Ultra-wideband Radar (UWB)

Forests environment is a strong clutter background. As a result, target-detection in foliage situation is more challenging and requires extensive data to process. Besides, the channel in this environment is time-varying and non-stationary. Because nested sampling and co-prime sampling are based on the premise of wide-sense stationary signal, they can't directly applied on the radar echoes. Short-time Fourier transform (STFT) has been widely applied on non-stationary signals. In this paper, we propose two improved STFT methods namely nested sampling based STFT (NS-STFT) algorithm and coprime sampling based STFT (CS-STFT) algorithm.

2.2.1 Sense-through-foliage Experimental Settings

Our data is from the experiment based on the radar-based sense-through-foliage in late summer and fall. The measurements were conducted by Virtual Machines Company in Holliston, Massachusetts [26]. Because of the limited rainfall, late summer foliage involved decreased water content. Late fall and winter measurements involved largely defoliated but dense forest. There are two sets of data used, good quality and poor quality. In Figure 2.1, we plot the good quality signal with target and without target.

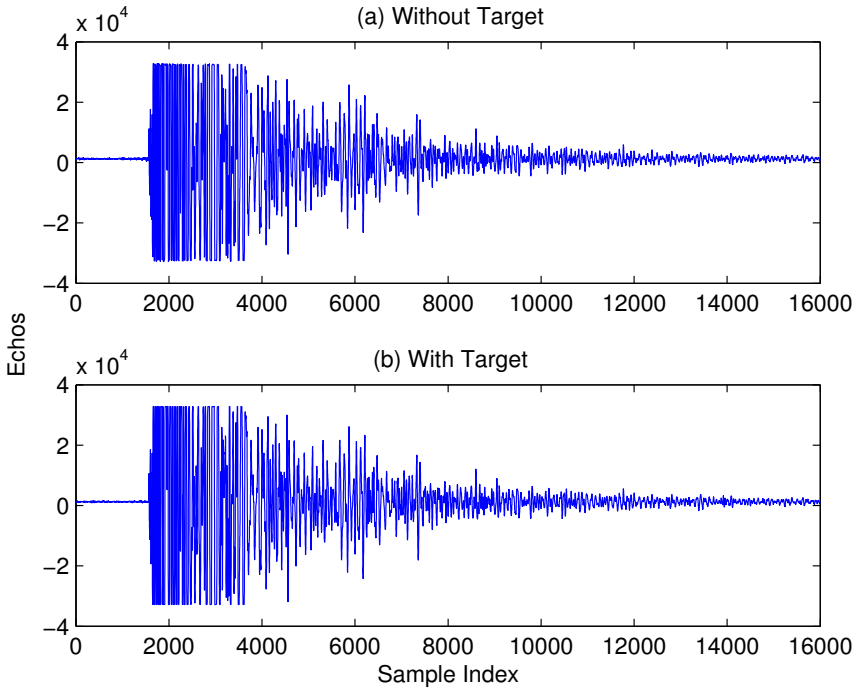

Figure 2.1. Measurement with very good quality signal and 100 pulses average, (a) no target on range, (b) with target on range (target appears at around sample 14,000).

The experiment is constructed on a seven-ton man lift which had a total lifting capacity of 450 kg [27]. The principle pieces of equipment secured on the lift are: Barth pulser, Tektronix model 7704B oscilloscope, dual antenna mounting stand, two antennas, rack system, IBM laptop, HP signal Generator, Custom RF switch and power supply and Weather shield (small hut).

In this experiment, a Barth pulse source (Barth Electronics, Inc. model 732 GL) was used. The pulse generator uses a coaxial reed switch to discharge a charge line for a very fast rise time pulse outputs. The model 732 pulse generator provides pulses of less than 50 picoseconds (ps) rise time, with amplitude from 150 V to greater than 2 KV into any load impedance through a 50 ohm coaxial line. The generator is capable of producing pulses with a minimum width of 750 ps and a maximum

of 1 microsecond. This output pulse width is determined by charge line length for rectangular pulses, or by capacitors for 1/e decay pulses. The interval of each sample is 50 picoseconds, and each set of data contains 16,000 samples for a total time duration of 0.8 microseconds at the rate about 20 Hz. The Barth pulse source was operated at low amplitude and 35 pulses reflected signal were averaged for each collection. Some existing works about sense-through-foliage target detection based on these data were reported in [28][29].

In Figure 2.1, good quality signal with target and without target are plotted but it's difficult to tell the difference. If we expand views from sample 13001 to 15000, it's shown in Figure 2.2. When there is target in the range, the difference of Figure 2.2(a) and 2.2(b) will be the response of target, which is Figure 2.2(c). Based on the knowledge of appearance of target, we can tell that the target is around at sample 14,000. But in practice, we obtain clutter echoes without acquiring the knowledge about target, so the problem is how can we detect the target only rely on Figure 2.2(b)? Moreover, if the signal quality is poor, it would be more difficult to find the position of the target.

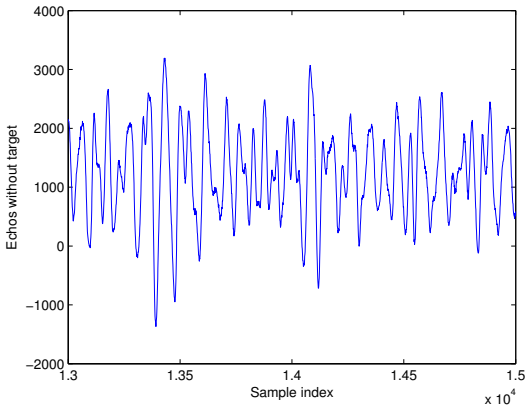

(a)

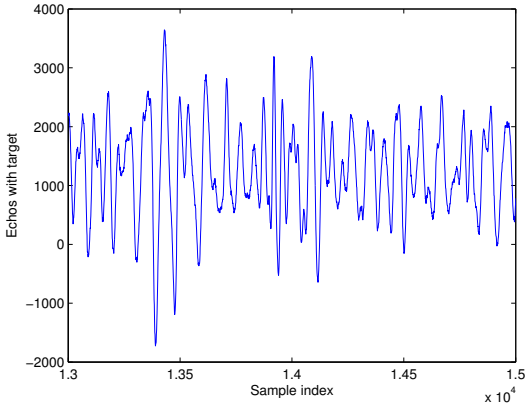

(b)

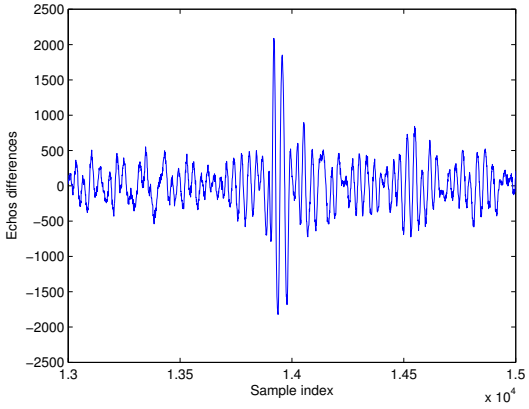

(c)

Figure 2.2. Measurement with very good quality signal and 100 pulses average. (a) Expanded view of no target on range, (b) expanded view of target on range, (c) difference between (a) and (b).

2.2.2 Theoretical Analysis

From Wiener-Khinchin Theorem, the relationship between auto-correlation function and power spectral density (PSD) for wide-sense stationary signal is defined below.

For discrete signal $x[n]$,

$$S(f) = \sum_{k=-\infty}^{+\infty} R_x(k) e^{-i2\pi fk} \tag{2.1}$$

where

$$\begin{aligned} R_x(k) &= E[x(n)x^*(n-k)] \\ &= \begin{cases} \frac{1}{N}\sum_{n=0}^{N-k-1} x(n)x^*(n-k), & 0 \le k \\ R_x(-k), & k < 0 \end{cases} \end{aligned} \tag{2.2}$$

and N is the length of echo x.

Another way to calculate PSD of $x(n)$ is through the N-point discrete Fourier transform (DFT),

$$X(f) = \sum_{n=0}^{N-1} x(n) e^{-i2\pi/Nkn} \tag{2.3}$$

$$S(f) = |X(f)|^2 \tag{2.4}$$

From property 1, the cross difference is given in the range $-[(N_1+1)N_2 - 1] \le k \le [(N_1+1)N_2 - 1]$ and thus the estimate of auto-correlation of nested sampling for all lags k can be obtained by

$$\hat{R}_n(k_n) = E[x(n)x^*(n-k)] = \frac{1}{P}\sum_{p=0}^{P-1} x(n)x^*(n-k) \tag{2.5}$$

and for co-prime sampling, the estimate autocorrelation is [17]

$$\hat{R}_c(k_c) = \frac{1}{P}\sum_{p=0}^{P-1} x(M(n_1+Np))x^*(N(n_2+Mp)) \tag{2.6}$$

When target appears, the sample strength changes more abruptly, which implies that the echo contains more AC values than that without targets. In [30], the author introduced short time Fourier-transform to deal with the non-stationary signal. For a continuous-time signal, the definition of STFT is

$$Y(m,w) = \int_{-\infty}^{+\infty} x(t)w(t-m)e^{-jwt}dt \tag{2.7}$$

Here, $x(t)$ is the echo signal and $w(t)$ is the window function. $Y(m,w)$ represents sinusoidal values in every window at time position m. When moving the window, $x(t)$ is supposed to be stationary in corresponding window duration. The window's interval defines the frequency resolution of the STFT analysis, as a result, we should choose the window's length short so that it can approximate the signal's spectrum well.

If the signal is discrete, (2.7) is expressed as

$$Y(m,w) = \sum_{n=0}^{N-1} x(n)w(n-m)e^{-iwn} \tag{2.8}$$

There are different kinds of windows to choose, such as Gaussian window and rectangular window. No matter what kind of window is chosen, the result only represents that the PSD of the signal is changing with time. In this work, we apply a rectangular window, with the length L and step size M,

$$w(n) = \begin{cases} 1 & if \;\; 0 \le n \le L-1 \\ 0 & otherwise \end{cases} \tag{2.9}$$

After each step of STFT, we cumulate the power of AC values as following:

$$P(m) = \sum_{w=4}^{L-1} |Y(m,w)|^2 \tag{2.10}$$

Combining (2.4) and (2.8), $P(m)$ of NS-STFT and CS-STFT can be expressed as

$$P_n(m) = \sum_{m=4}^{L-1} S_n(m,w), w = 2\pi f \tag{2.11}$$

Table 2.1. Variables used in this section

Notations	Meaning
(M, N)	co-prime pair used in the sampling
P	number of period of nested sampling or co-prime sampling
$x(n)$	discrete echo signal
$R(k)$	Autocorrelation of the discrete signal
$\hat{R}_n(k)$	Autocorrelation of the nested sampling signal
$\hat{R}_c(k)$	Autocorrelation of the co-prime sampling signal
$S_n(m,w), S_c(m,w)$	Power spectral density
$P_n(m), P_c(m)$	power of AC values

$$P_c(m) = \sum_{m=4}^{L-1} S_c(m,w), w = 2\pi f \tag{2.12}$$

where

$$\begin{aligned} S_n(m,w) &= \sum_{n=0}^{N-1} \hat{R}_n(k_n) w(n-m) e^{-iwk} \\ &= \sum_{n=0}^{N-1} \{ \frac{1}{P} \sum_{p=0}^{P-1} x(n) x^*(n-k) w(n-m) e^{-iwk} \} \end{aligned} \tag{2.13}$$

and

$$\begin{aligned} S_c(m,w) &= \sum_{n=0}^{N-1} \hat{R}_c(k_c) w(n-m) e^{-iwk} = \sum_{n=0}^{N-1} \\ &\{ \frac{1}{P} \sum_{p=0}^{P-1} x(M(n_1+Np)) x^*(N(n_2+Mp)) w(n-m) e^{-iwk} \} \end{aligned} \tag{2.14}$$

We detect the target through the power of AC values $P_n(m)$ and $P_c(m)$ respectively in NS-STFT method and CS-STFT method.

Several important variables in the new algorithms are listed in Table 2.1.

2.2.3 Simulation Results

2.2.3.1 NS-STFT approach

Firstly, we show the results of existing STFT method in Figure 2.3. Along with the moving of slicing window, we can acquire the power values of the echo $P(m)$ from sample 10,000 to 15,000. In [31], it has pointed out that generally the clutter has Gaussian distribution in the frequency domain. Therefore, when there is a target in the range, the power of AC values will behave like random noise. In Figure 2.3(a) and 2.3(b), we plot the good quality signal. It's clearly to see that in Figure 2.3(b), when there is target on range, the curve around 14,000 sample index is smooth. But in Figure 2.3(a), the curve is like chaotic impulses.

When the Barth pulse source was operated at low amplitude and the sample values are not obtained based on sufficient pulse response averaging (averaged over 35 pulses for each collection), significant pulse-to-pulse variability is noted and the return signal quality is poor. In this situation, a single radar cannot tell where the target is, since pulse-to-pulse variability exists in the echos at different time or different site, this motivates us to explore the spatial and time diversity using Radar Sensor Networks (RSN). In this paper, the RAKE structure is proposed in [30]. There are 30 radars combined in the simulation and the echo of each cluster-member radar sensor is combined by the clusterhead using a weighted average, which is determined by the power of each echo $x_i(m)$ (m is the sample index),

$$w_i = \frac{E_i}{\sum_{i=1}^{n} E_i} \tag{2.15}$$

and

$$E_i = var(x_i(m)) + [mean(x_i(m))]^2 \tag{2.16}$$

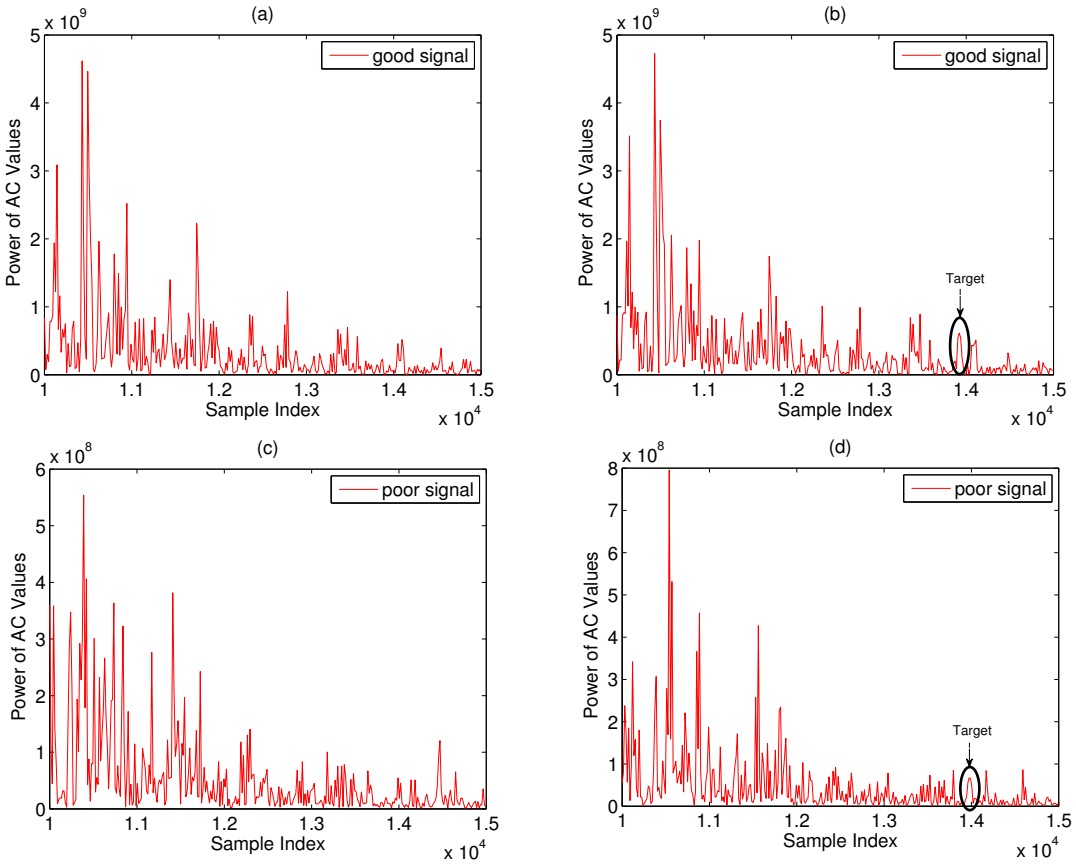

Figure 2.3. The power of AC values versus sample index of good quality data with window length $L = 30$, step size $M = 16$ and poor quality data with window length $L = 25$, step size $M = 15$, (a)(b) no target on range, (c)(d) with target on range.

The power of AC values are plotted in Figure 2.3(c) and 2.3(d), where the target is circled in the figure.

According to (2.13), we can plot the power spectral density of NS-STFT approach and the results are shown in Figure 2.4 and Figure 2.5. As property 3 states, the auto-correlation $\hat{R}_n$ will approximately equal to R_x, so we can detect the target based on (2.13). From the simulations we find that the window length L will affect the performance of target detection. When NS-STFT approach is employed on good

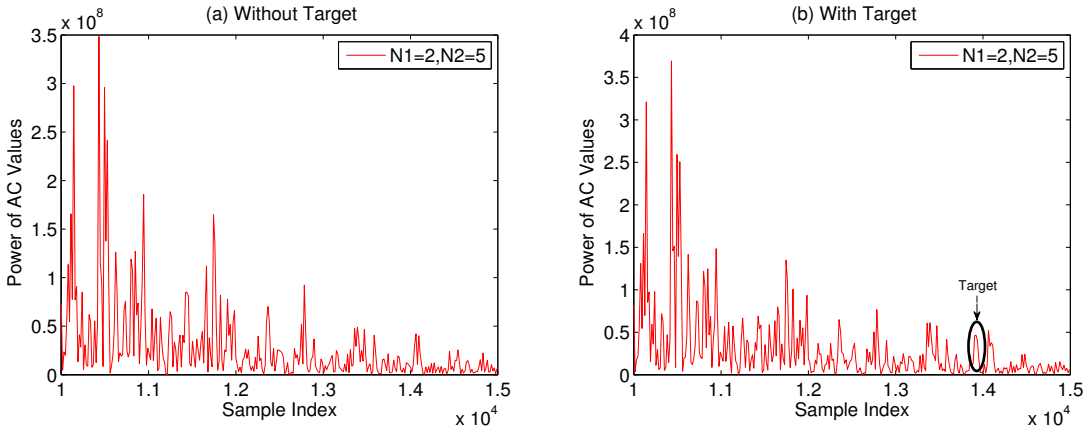

Figure 2.4. The power of AC values versus sample index of good quality data after nested sampling, with sampling pairs $N_1 = 2, N_2 = 5$, (a) no target on range, (b) with target on range (target appears at around sample 14,000).

quality data, $L = 24$ is a little smaller than 30. This is because the existing variations of estimated auto-correlation.

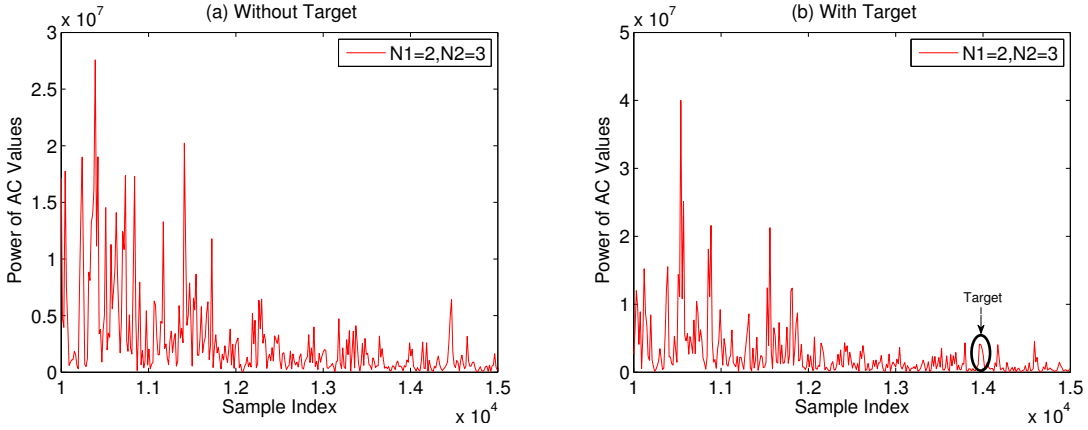

Figure 2.5. The power of AC values versus sample index of poor quality data after nested sampling, with sampling pairs $N_1 = 2, N_2 = 3$, (a) no target on range, (b) with target on range (target appears at around sample 14,000).

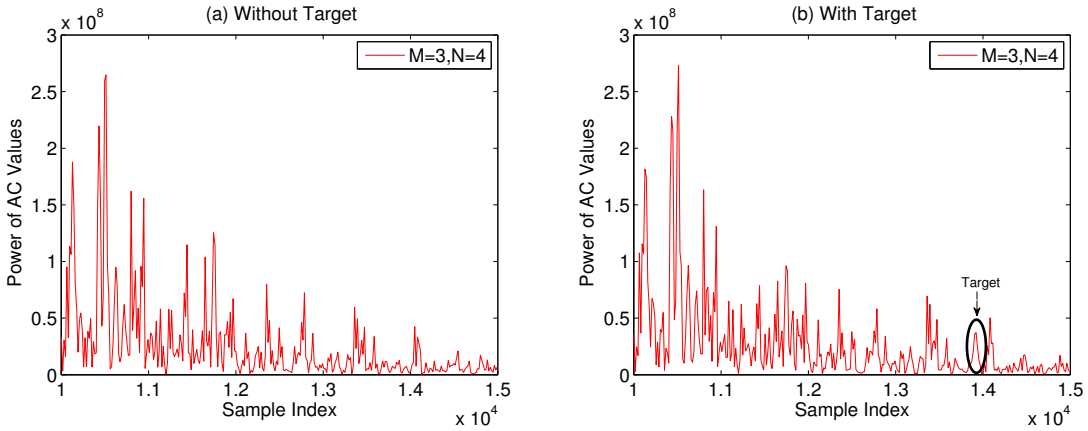

Figure 2.6. The power of AC values versus sample index of good quality data after co-prime sampling, with sampling pairs $M = 3, N = 4$, (a) no target on range, (b) with target on range (target appears at around sample 14,000).

Based on the sampling rate (1.3), we can calculate the compression ratio of nested sampling. For example, in Figure 2.5(a), the pair of nested sampling is $N_1 = 2, N_2 = 5$. Therefore, the compression ratio is decreased to about 46.67%, this saves almost half of the space, which is quite desirable for large amount of data.

2.2.3.2 CS-STFT approach

The results of CS-STFT on good quality data and poor quality data are presented in Figure 2.6 and Figure 2.7. For good data, co-prime pairs $M = 3, N = 4$ are chosen and for poor quality signal, we use the sampling pair (2,3). When target appears, the curve around 14,000 behaves like a Gaussian pdf as circled in Figure 2.6(b) and 2.7(b). The window length L in CS-STFT method is almost the same as in NS-STFT method, which is 23 for good quality data. The compression ratio of co-prime sampling in Figure 2.6 could be calculated by (1.7) and it is 58.3%. If the sampling rate f_s keeps increasing, the window length L must decrease. However, in

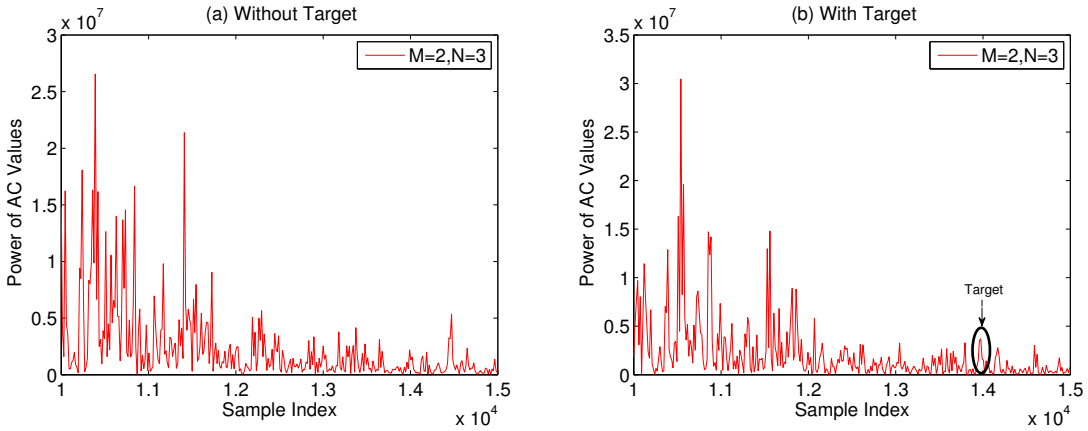

Figure 2.7. The power of AC values versus sample index of poor quality data after co-prime sampling, with sampling pairs $M = 2, N = 3$, (a) no target on range, (b) with target on range (target appears at around sample 14,000).

the case of poor quality signal, compression becomes more difficult since there will be more noise included in the data, so we only choose the sampling pair (2,3).

2.3 Singular-Value Decomposition-QR (SVD-QR) Algorithm

SVD-QR algorithm is proposed in [24] [25], which is a preferable method in rank deficient problems. In a least-square sense, it chooses a subset from the independent data which have the minimum residual error. Here the main mathematical notations are:

1) Given the phase history data set matrix $\mathbf{P} \in R^{N \times M}$, $r = \text{rank } (\mathbf{P}) \leq M$ and r' is the numerical estimation of rank r through

$$P = \mathbf{U} \begin{bmatrix} \Sigma & 0 \\ 0 & 0 \end{bmatrix} \mathbf{V}^T \tag{2.17}$$

where $\mathbf{U}$ is a size $N \times N$ matrix of orthonormalized eigenvectors of $\mathbf{P}\mathbf{P}^T$, $\mathbf{V}$ is an $M \times M$ matrix of orthonormalized eigenvectors of $\mathbf{P}^T\mathbf{P}$, and Σ is the diagonal matrix which is

$$\Sigma = diag(\sigma_1, \sigma_2, ..., \sigma_r), \sigma_i = \sqrt{\lambda_i}. \tag{2.18}$$

here λ_i is the ith eigenvalue of $\mathbf{HH}^T$ and select $\hat{r} \leq r'$.

2) Compute a permutation matrix $\mathbf{E}$ such that the columns of the matrix $\Gamma_1 \in R^{N \times \hat{r}}$ in

$$\mathbf{PE} = [\Gamma_1, \Gamma_2] \tag{2.19}$$

are independent. The permutation matrix $\mathbf{E}$ is obtained from the QR decomposition of the sub-matrix comprised of the right singular vectors, which correspond to the $\hat{r}$ ordered most significant singular values.

The specific procedures of this algorithm could be presented as following:

Step 1: Create a matrix $\mathbf{P}$ which is selected from the phase history data.

Step 2: Execute SVD-QR as describing above to the slow-time history phase data and decide the most important collections to be used in the image formation.

Step 3: Partition

$$V = \begin{bmatrix} V_{11} & V_{12} \\ V_{21} & V_{22} \end{bmatrix} \tag{2.20}$$

where $V_{11} \in R^{\hat{r} \times \hat{r}}$, $V_{12} \in R^{\hat{r} \times (M-\hat{r})}$, $V_{21} \in R^{(M-\hat{r}) \times \hat{r}}$ and $V_{22} \in R^{(M-\hat{r}) \times (M-\hat{r})}$. For $\hat{r}$, it could be selected smaller than r' in many practical cases.

Step 4: Pivoting the column by using QR decomposition, determine $\mathbf{E}$ such that

$$\mathbf{Q} \times \mathbf{R} = [V_{11}^T, V_{21}^T]\mathbf{E} \tag{2.21}$$

here $\mathbf{Q}$ represents a unitary matrix, $\mathbf{R}$ forms an upper triangular matrix with decreasing elements and $\mathbf{E}$ is the permutation matrix.

After decomposition and pivoting, the most significant $\hat{r}$ can be decided, which in short is the set used to construct the image.

2.4 Implementation in Synthetic Aperture Radar (SAR)

2.4.1 Background of Gotcha Data Set

Gotcha SAR Dataset is an open source for radar algorithm research, which collects signal at a 640MHz bandwidth and the on-board radar covers eight different elevation angles of phase history data with full polarization. The trace of the aircraft is a circle over an area of parking lot and the on-board, side-looking radar transmits and receives electromagnetic waves at a constant pulse repetition interval (PRI). We choose the Pass 1 data with HH polarization and there are total 360 data sets.

2.4.2 Theoretical Analysis

In Figure 2.8, we illustrate the circular SAR geometry as an example. The civilian vehicles and calibration target locate in the monitored area.

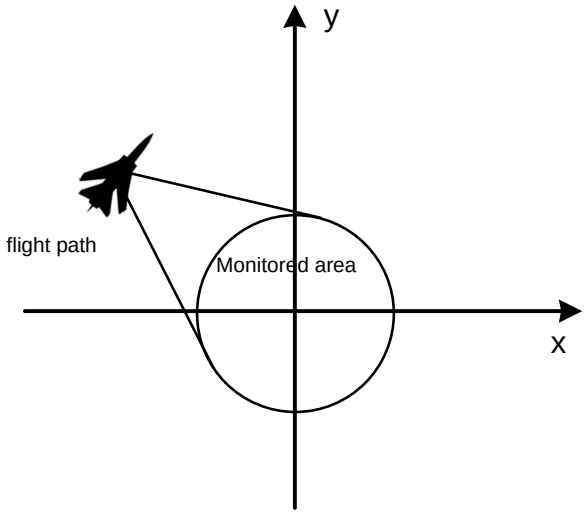

Figure 2.8. Imaging system geometry in circular SAR .

The real path in the figure can be written as

$$\mathbf{r}_a(\tau) = (x_a(\tau), y_a(\tau), z_a(\tau)) \tag{2.22}$$

where τ denotes the slow-time domain.

If we define the distance with respect to the origin (0,0,0), it is

$$d_a(\tau) = \sqrt{(x_a(\tau))^2 + (y_a(\tau))^2 + (z_a(\tau))^2} \tag{2.23}$$

A target in the range is located at

$$\mathbf{r}(\tau) = (x(\tau), y(\tau), z(\tau)) \tag{2.24}$$

We assume this target is stationary, as a result, the distance between the antenna phase center and the target can be calculated by

$$d_{a0}(\tau) = \sqrt{(x_a(\tau) - x)^2 + (y_a(\tau) - y)^2 + (z_a(\tau) - z)^2} \tag{2.25}$$

Along the flight path, the radar transmits and receives pulses. In a given synthetic aperture, N_p pulsed used to construct the image and the transmission time of each pulse is $\{\tau_n, n = 1, 2, ..., N_p\}$. There are K frequency samples per pulse, which are $\{f_k, k = 1, 2, ..., K\}$.

Furthermore, we assume the output of the receiver at a given time τ, which is the time delayed by the round-trip to the target, sampled on band-limited frequency domain of a pulse and the scene center has zero phase. Therefore the receiving signal is written as

$$S(f_k, \tau_n) = e^{-2\pi f(2(d_{a0}(\tau_n) - d(\tau_n))/c)} \tag{2.26}$$

Assuming at a discrete range bin m, (2.26) is rewritten as

$$s(m, \tau_n) = \sum_{k=1}^{K} S(f_k, \tau_n) e^{(2\pi f(2(d_{a0}(m,\tau_n) - d(m,\tau_n))/c)} \tag{2.27}$$

The imaging formation result is decided by the reflectivity of the target scene, for instance, some areas with small reflectivity values can be considered as no target, which are shown in dark color in the figure. This motivates us to separate a space into principle and sub-principle subspaces.

2.4.3 Simulation Results

Firstly, we show an example of data reduction in phase history. SVD a matrix P and get $diag(\Sigma) = (0.059510004, 0.042771991, \cdots, 0.0043679429, 0.0041228784)$. It's necessary to decide the value of $\hat{r}$, here in Figure 2.9, we plot the singular values Σ.

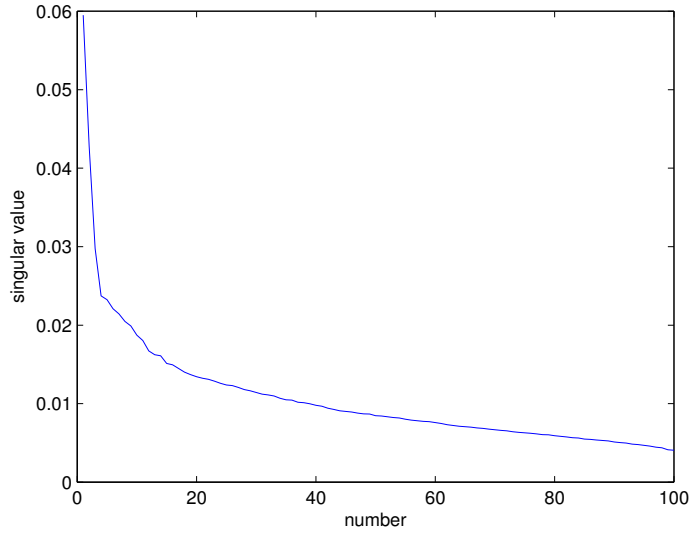

Figure 2.9. Applying SVD-QR algorithm, the results of singular values. .

It's clearly to see that the slope of the curve changes from steeply to slightly, and around after 40, the singular values are much smaller than before. As a result, in the simulation we define $\hat{r} = 40$. In order to get V_{11} and V_{21}, V needs to be partitioned before QR decomposition. V_{11} is a size of $R^{40\times 40}$ matrix and V_{21} is $R^{(M-40)\times 40}$.

With column pivoting and QR decomposition, the economy matrix $\mathbf{E}$ is determined. In this instance, $\hat{r} = 40$, we only care about forty columns of $\mathbf{E}$. For example, if

$$\mathbf{E} = \begin{bmatrix} 0 & 0 \\ 0 & 0 \\ 0 & 1 \\ 1 & 0 \\ 0 & 0 \\ 0 & 0 \\ 0 & 0 \\ 0 & 0 \end{bmatrix}$$

the values of 1 appears in the forth and third columns of the input matrix $\mathbf{P}$, which means that the data collected only from these two angular are the most significant, and they can effectively represent all the others.

In [32], a challenging problem of two dimensional image formation of stationary targets is released, which aims to construct an area of numerous civilian vehicles and calibration targets. In the simulations, we randomly choose 21 files of the history data with total number of 2462 sets data and no windowing is applied to the data before imaging. After the SVD-QR algorithm, the scenario is recovered through about half of the original data. In Figure 2.10, the original image formation result by using backprojection algorithm is presented.

If we employ the SVD-QR method before backprojection algorithm, the phase history data could be compressed by a ratio about 2:5. The output of the image is plotted in Figure 2.11(a).

We can see that even if some information is lost, the main properties of the scenario are preserved well. It proves the validity of SVD-QR algorithm in 2D SAR environment. In order to show the importance of correctly selecting echoes, in Figure

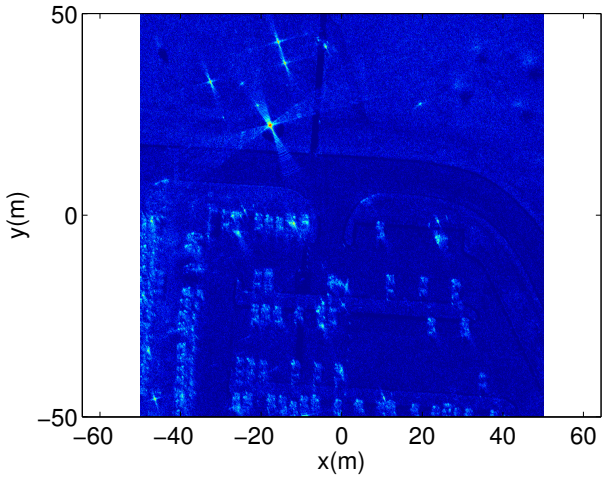

Figure 2.10. Original image formation via backprojection algorithm using volumetric challenge problem data set. .

2.11(b), we compare it with the uniform down sampling of the data, which achieves the compression ratio as 1:2. It seems that if we uniformly sample the data, we will miss more significant information than SVD-QR algorithm.

2.5 Conclusions

In this chapter, two target detection algorithms in foliage environment are developed, which are NS-STFT approach and CS-STFT approach. Since nested sampling and coprime sampling are sub-Nyquist sampling, the NS-STFT methods and CS-STFT method can save about half the quantity of the data comparing with the original approach. The results show that as long as we choose suitable window length and step size, the new methods can achieve the same performance. The window length falls when the sampling frequency increases. The poorer the quality of the signal is, the more difficult to compress. Besides, if the signal quality is poor, with the help of RSN and RAKE structure, it's easy to detect target on range intuitively.

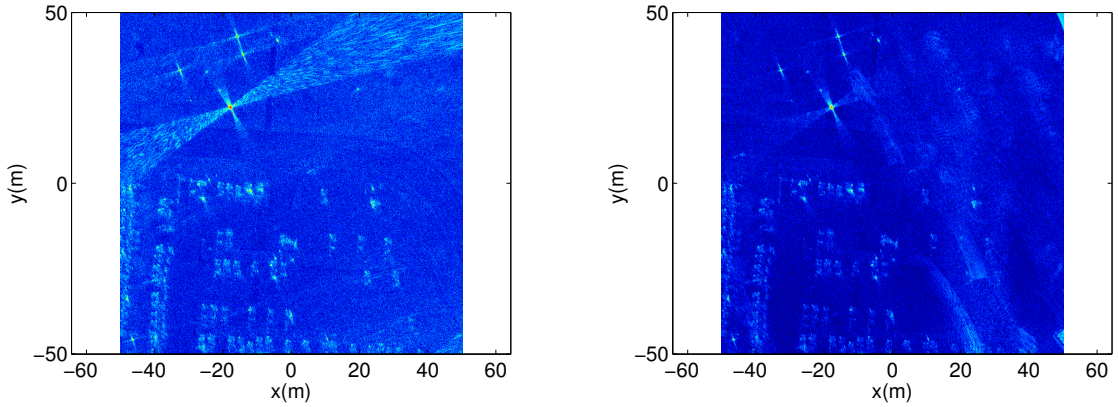

Figure 2.11. Compression image formation via Volumetric Challenge Problem data set, (a) SVD-QR algorithm, (b) uniform down sampling .

In addition, the high redundant SAR raw data of the signal echoes is compressed by exploiting SVD-QR algorithm in slow-time domain of the data set before using backprojection image reconstruction method. This is less complicated than many compressive sensing algorithms and can achieve better performance than uniform down sampling method. We test our algorithm and compare it with uniform down sampling on Volumetric Challenge Problem data set, which is collected in a real scenario. The results show that this algorithm can successfully recover the image without losing important information such as the vehicles and calibration targets and the compression ratio could achieved by 2:5 overall. This is the first time that SVD-QR algorithm is applied to the real 2D SAR data.

CHAPTER 3

Sensing with Application to Greenland Bed Elevation Assessment

3.1 Introduction

The Greenland Ice Sheet is about 1,710,000 square kilometers (656,000 square miles), covering 80% of the island of Greenland, which is almost three times the size of Texas [33]. Since the ice sheets could rise the sea level, influence the weather and climate, finding a possible method to improve the resolution of Greenland bed elevation map is very essential.

Broadly speaking, there are three ways to increase resolution level. One direct approach is to decrease the pixel size by sensor manufacturing techniques. If the pixel size is reduced, the number of pixels in one unit area of an image will increase and thus more detailed information is offered. However, this will generate shot noise that degrades the image quality severely [34]. Another approach is mentioned in [35], where the author enlarged the chip size to achieve high resolution performance. However, the expensive high precision hardware sometimes is not affordable. Subsequently, people find the third direction – signal processing techniques – to obtain HR image from low-resolution images. In [36] and [37], the authors applied discrete cosine transform and wavelet transform for HR images. For many imaging systems such as visual charge coupled device (CCD) cameras, since some extent aliasing from under-sampling is allowed, in [38], a maximum a posterior (MAP) framework for jointly estimating image registration parameters and the high-resolution image was proposed. In addition, [39] presented a way of multiple-frame image restoration and registration. Interpolation was also involved with HR images [40]-[42], and some

popular interpolation algorithms such as the nearest neighbor interpolation, bilinear interpolation and bicubic interpolation were provided in [43], [44] and [45] respectively.

Among signal processing studies, compressive sensing has been investigated for several years and currently has a wide range of application such as imaging, radar signal processing and channel coding [11]-[13]. In [46], CS was successfully applied in MRI scanning to generate HR images. The theory is to reconstruct certain signals or images based on samples from sub-Nyquist sampling. The advantage of CS is that it only requires a small number of samples and has a relative robust performance in reconstruction. However, when the compression ratio is too high, the reconstruction errors of CS could be very large. As a consequence, we want to combine CS with other techniques to overcome the large errors in high compression ratio scenario. The difficulties of compressive sensing lies in the efficiency and accuracy of the construction algorithms. In many existing works [47]-[50], ℓ_1-minimization methods such as basis pursuit (BP) and greedy algorithm like matching pursuit (MP) and orthogonal matching pursuit (OMP) have been explored. The author in [51] proposed a new gradient projection (GP) approach to reduce the complexity of the previous algorithms such as OMP and it is easy to be implemented. In this paper, we introduce co-prime sampling to the gradient projection method in order to improve the resolution of Greenland elevation map.

In [9] and [10], co-prime sampling had been applied to estimation of multiple frequencies and synthetic aperture radar of moving targets. Besides, co-prime sampling combined with DFT filter banks was applied to obtain a high resolution beamformer. All these works focused on stationary signals. For non-stationary signal, [52] also studied co-prime sampling in radar signal processing. Co-prime sampling is usually applied in under-sampling process and calculating correlation, while there is another

property of co-prime sampling – orthogonality, which could be used to complementary combine two co-prime images [14]. Since co-prime structure is easy to built and has the closed form expressions, introducing co-prime sampling into CS to improve the performance is desirable. Unlike other previous papers on compressive sensing, we first propose an interpolation structure based on co-prime sampling. Then we estimate the missing pixels by GP algorithm and finally the high resolution picture is presented.

The main contribution of this work is that we extend the co-prime structure to interpolation and compressive sensing. To the best of our knowledge, this is the first time that co-prime sampling is exploited in interpolation process. One advantage of this approach is to achieve smaller RMSE and higher PSNR in the reconstructed images. Furthermore, the blurry parts in the recovered images could also be removed via orthogonal and complementary property of co-prime interpolation.

3.2 Preliminaries

In this section, we provide some preliminaries of co-prime sampling and compressive sensing. In addition, we also demonstrate the advantage of co-prime structure.

3.2.1 Co-prime Sampling for An Image

Assume $f(p_i)$ is the input signal where $i \in \mathbf{I} = \{0, 1, 2, \ldots, N\}$, if we use the co-prime pair (M_1, M_2) where M_1 and M_2 are prime numbers to do the sampling respectively, the interpolated locations are in sets $\mathbf{K}_1$ and $\mathbf{K}_2$

$$\begin{aligned}\mathbf{K}_1 &= \left\{0, M_1, 2M_1, 3M_1, \ldots, \left\lfloor \frac{N}{M_1} \right\rfloor \times M_1\right\} \\ \mathbf{K}_2 &= \left\{0, M_2, 2M_2, 3M_2, \ldots, \left\lfloor \frac{N}{M_2} \right\rfloor \times M_2\right\}\end{aligned} \tag{3.1}$$

For co-prime down-sampling, the values of locations in (3.1) are discarded, but in this work, we'll insert values in the sampling locations in (3.1). Because M_1 and M_2 have no other common divisors excluding one, the overlapping sampling locations only occur when

$$\frac{d_1}{d_2} = \frac{M_1}{M_2} \tag{3.2}$$

where $d_1 \in \mathbf{K}_1$ and $d_2 \in \mathbf{K}_2$, so that the number of overlapping sampling locations is

$$q = \left\lfloor \frac{N-1}{M_1 M_2} \right\rfloor + 1 \tag{3.3}$$

If (M_1, M_2) are large prime numbers, then q is small. As a result, the co-prime sampling process could be treated as orthogonal interpolation. In Figure 3.1, we illustrated the sampling process for a $m \times n$ image with co-prime pair $(3, 5)$ in one period. The sampling positions are stored in the form of two vectors in (3.1). Since image data usually stores in a matrix, in order to apply the co-prime sampling, we reshape the matrix into a vector. Except for the index 0, there's no overlapped samples between sequence s_1 and s_2.

Property 6. *Given co-prime pair (M_1, M_2) and any integer h, then h can be obtained by*

$$h = a_1 M_1 + a_2 M_2 \tag{3.4}$$

where a_1 and a_2 are any integers as well.

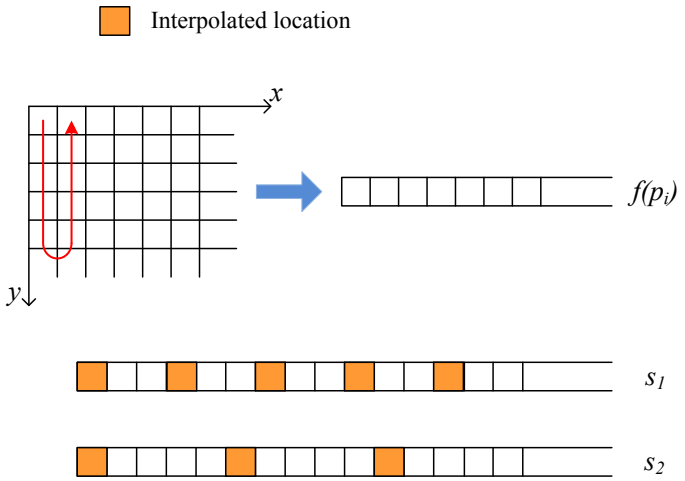

Figure 3.1. Image f and co-prime sampling with pair $(3, 5)$.

Proof. If $1 = a_1M_1 + a_2M_2$ exists for any co-prime pair, and we compute the value of a_1, a_2 as

$$\begin{aligned} gcd(M_1, M_2) = h_n &= h_{n-2} - h_{n-1}q_n \\ &= h_{n-1}(q_nq_{n-1} + 1) - h_{n-3}q_n \\ &= h_{n-3} \times * + h_{n-4} \times * \\ &\vdots \\ &= M_1 \times * + M_2 \times * \end{aligned} \tag{3.5}$$

So we can find a_1 and a_2 satisfying $1 = a_1M_1 + a_2M_2$, then any h can be obtained. □

In property 6, we prove that the sum of two prime numbers can be any integer. This complementarity brings the advantage of reducing the replicas in two under-sampling images. It is because that at the same location, the image value is different in two co-prime sequences and only one should be the correct image value. The replicas could be removed by choosing the largest image value. Besides, co-prime

sampling structure can be expressed in closed forms, which makes it convenient to do the numerical analysis.

3.2.2 Compressive Sensing

CS provides a nonlinear reconstruction approach that combines sensing and compression of compressible signals. Let f still denotes the signal of interest, which is a K-sparse vector with respect to the sparsing basis Ψ, so

$$f = \Psi\theta, \quad \theta \in \mathbb{R}^N, \quad \|\theta\|_0 = K \tag{3.6}$$

Then the object y is obtained by correlating x with a measurement matrix Φ

$$y_k = \langle f, \phi_k \rangle, \quad k = 1, \ldots, M \tag{3.7}$$

The main result solved by compressive sensing is that if $\Phi\Psi$ satisfies the restricted isometry property [12][53], then the K-sparse vector θ could be represented in a linear program

$$\min_{\theta} \|\theta\|_{\ell 1} \quad \text{subject to} \quad y = \Phi\Psi\theta \tag{3.8}$$

This is the classic BP algorithm. In our following derivation, (3.6) is modified by the new proposed GP algorithm [51] as

$$\begin{aligned} \min_{u,v} \quad & \frac{1}{2}\|y - \Phi\Psi(u - v)\|_2^2 + \tau u + \tau v \\ \text{subject to} \quad & u \geq 0 \\ & v \geq 0 \end{aligned} \tag{3.9}$$

where $\theta = u - v$.

3.3 Co-prime Interpolated Compressive Sensing

In this section, with the purpose of improving the performance of compressive sensing, we propose the co-prime interpolated compressive sensing (CopCS) approach.

Assume g is the corresponding interpolation function, then $g(p_i) = y(p_i)$ where p_i is the location of interpolation and y is the image data. After interpolation, y becomes

$$\widetilde{y} = \Phi f + g \tag{3.10}$$

The interpolation function is defined by the nearest neighbor algorithm. Nearest neighbor interpolation is a simple interpolation method in one or multiple dimensions. In the following, a simplified nearest neighbor algorithm is proposed to build the interpolation function.

For the image, we utilize two dimensional interpolation where the row is the x-direction and column is the y-direction. Let $\mathbf{K}_1$ be the set of indices as shown in (3.1) and $(\mathbf{P}_k)_{k\in\mathbf{K}_1}$ is the point needs to be interpolated, $\mathbf{R}_k$ is the subset in $\mathbf{I}$ associated with $\mathbf{P}_k$ in which all the points' distance is less or equal to r_0. r_0 is the radius of the region. This relationship can be expressed as

$$\mathbf{R}_k = \{i \in \mathbf{I} | D(i, \mathbf{P}_k) \leq r_0 \text{ except for k}\} \tag{3.11}$$

where function D is the distance between two pixel, and it could be measured by Euclidean distance. If assume their coordinates are $p_1 = (x_1, y_1)$ and $p_2 = (x_2, y_2)$, then

$$D(p_1, p_2) = \sqrt{(x_1 - x_2)^2 + (y_1 - y_2)^2} \tag{3.12}$$

The interpolation function is defined as the average of all values in $\mathbf{R}_k$,

$$g(p_i) = \overline{\sum_{p_i \in \mathbf{R}_k} f(p_i)}, \quad f(p_i) \neq 0 \tag{3.13}$$

Suppose every pixel size is 1×1 and the image size is $m \times n$, if we let $r_0 = 1.5$ and select co-prime pair (M_1, M_2) to do the interpolation, for M_1 and $k = 1$, the index subset $\mathbf{R}_1$ is

$$\begin{aligned} \mathbf{R}_1 = &\{p_i - m - 1, p_i - m, p_i - m + 1, p_i - 1, \\ &p_i + 1, p_i + m - 1, p_i + m, p_i + m + 1\} \end{aligned} \tag{3.14}$$

and thus the interpolation equation could be rewritten to

$$g(p_i) = \overline{\sum_{p_i \in \mathbf{R}_1} f(p_i)}, \quad f(p_i) \neq 0 \tag{3.15}$$

For M_2, the result is similar. Now the compressive sensing equation (3.9) is modified with the new generated object $\widetilde{y}$ as

$$\begin{aligned} \min_{u,v} \quad & \frac{1}{2}\|\widetilde{y} - \Phi\Psi(u - v)\|_2^2 + \tau u + \tau v \\ \text{subject to} \quad & u \geq 0 \\ & v \geq 0 \end{aligned} \tag{3.16}$$

As a consequence, the input signal after interpolating by M_1 and M_2 is referred to as f_1 and f_2.

$$\begin{aligned} f_1 &= \Psi\hat{\theta} \\ f_2 &= \Psi\hat{\theta}' \end{aligned} \tag{3.17}$$

Therefore, if we choose the largest pixel value in f_1 and f_2, the final recovered data $\hat{f}$ could be obtained, which is expressed as

$$\hat{f}(p) = \begin{cases} f_1(p) & if \quad |f_1(p)| \geq |f_2(p)| \\ f_2(p) & otherwise \end{cases} \tag{3.18}$$

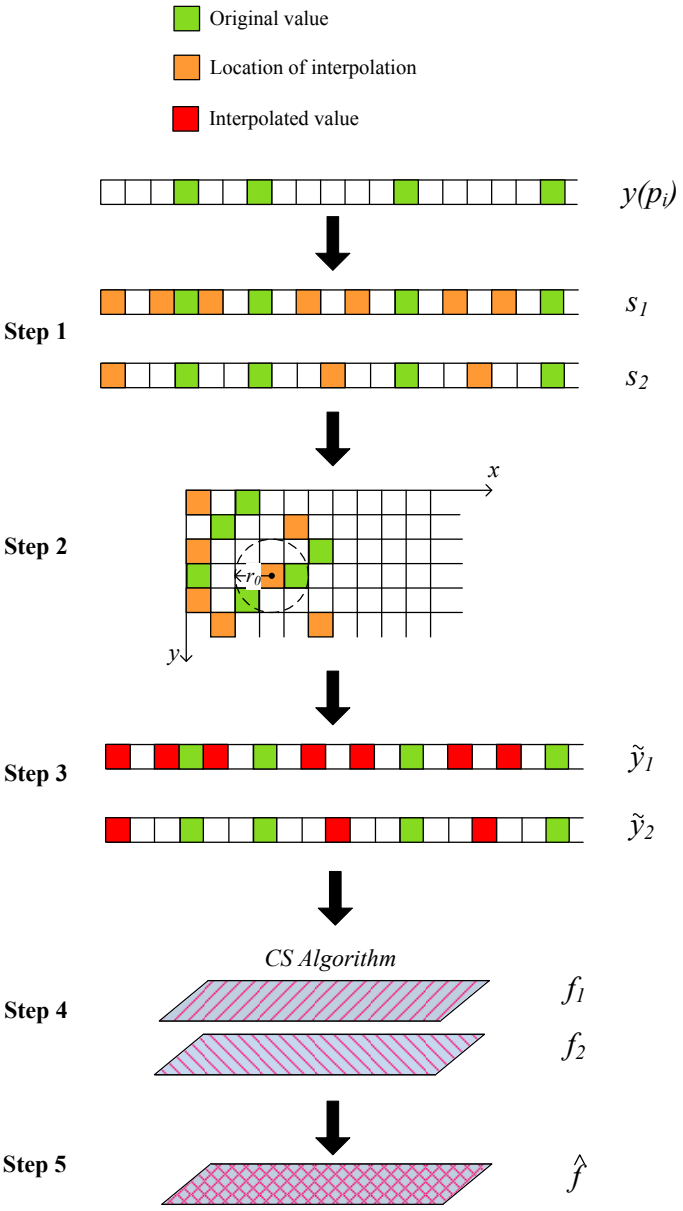

Figure 3.2. Process of CopCS algorithm.

The complete process of CopCS algorithm is shown in Figure 3.2 and the corresponding steps are explained as follows.

Step 1 : Calculate the locations in the vector that need to be interpolated with co-prime pair (M_1, M_2).

Step 2 : Use the interpolation function to estimate the value for every position in Step 1.

Step 3 : Synthesize the estimated values into the vector, get the new object $\tilde{y}_1$, $\tilde{y}_2$.

Step 4 : Recover the sparse vector $\hat{\theta}$, $\hat{\theta}'$ for M_1, M_2 respectively and compute the corresponding f_1, f_2.

Step 5 : Choose the largest amplitude of each pixel in f_1 and f_2, build the final recovered sequence $\hat{f}$.

3.4 Numerical Analysis of CopCS Algorithm with Different Co-prime Pairs

The operation principle of CopCS has been illustrated in the previous section, but there is no numerical analysis of the proposed algorithm. In this section, we first provide two well-known image quality metrics – root mean square error (RMSE) and peak signal-to-noise ratio (PSNR), to measure the difference between original image and reconstructed image. After that, the relationship between compression ratio and co-prime pair is discussed.

3.4.1 RMSE and PSNR

Root mean square error and peak signal-to-noise ratio are widely used as the image and video quality metrics because of the low complexity. PSNR is computed through the result of mean square error (MSE) and usually a higher PSNR indicates higher quality of the reconstructed picture. Assume an image F is the reference image and the comparing image is $\widetilde{F}$, both size are $m \times n$. The MSE is defined as

$$MSE = \frac{1}{mn} \sum_{i=0}^{m-1} \sum_{j=0}^{n-1} [F(i,j) - \widetilde{F}(i,j)]^2 \tag{3.19}$$

and the RMSE is the direct square root of MSE

$$RMSE = \sqrt{MSE} \tag{3.20}$$

If RMSE is small, it means that the difference between image F and $\widetilde{F}$ is small. In addition, the PSNR is defined as

$$\begin{aligned} PSNR &= 10\log_{10}\left(\frac{MAX_F^2}{MSE}\right) \\ &= 20\log_{10}\left(MAX_F\right) - 10\log_{10}\left(MSE\right) \end{aligned} \tag{3.21}$$

where MAX_F is the maximum pixel value of image F.

3.4.2 Analysis of Compression Ratio

It is worth noting that since interpolation process is involved, the compression ratio will be changed by different choice of co-prime pair (M_1, M_2). The compression ratio is specified as

$$CR = \frac{\text{uncompressed size of image}}{\text{compressed size of image}} \tag{3.22}$$

For a traditional image, it may be made of millions of pixels but in compressive sensing, only a very small fraction, like 20% is selected. If we keep $a\%$ of the pixels and the size of the image is still $m \times n$, without co-prime interpolation, the compression ratio should be $\frac{mn}{a\%mn} = \frac{100}{a}$. As a result, the more pixels we discard, the higher compression ratio is. When co-prime pair (M_1, M_2) is applied and $M_1 < M_2$, the CR in (3.22) could be rewritten as

$$CR = \frac{M_1}{a\%M_1 + 1} \tag{3.23}$$

Table 3.1. Theoretical and Practical Compression Ratio with $a\% = 10\%$

co-prime pair	**theoretical CR**	**practical CR**
(2,3)	1.6667	3.8039
(3,4)	2.3077	4.5755
(4,5)	2.8571	6.0870
(5,6)	3.3333	7.5916
(6,7)	3.7500	9.1168
(7,8)	4.1176	10.6075
(8,9)	4.4444	12.1402

Property 7. *For a pairwise co-prime sequence $M_1, M_2, \ldots, M_r$, $M_1 < M_2 < \ldots < M_r$, compression ratio is mainly decided by M_1 when $a\%$ is determinate. Furthermore, if M_1 increases, CR will increase.*

Property 7 explains the relationship between co-prime sampling and compression ratio. In Table 3.1, we show the theoretical and practical compression ratio for different co-prime pairs when $a\% = 10\%$.

However, the theoretical CR listed in Table 3.1 is relied on two very important preconditions, which are (1) the interpolated value $g(p_i)$ computed by (3.13) is non-zero, (2) there's no sampled pixel at the location of multiple of M_1. If $g(p_i)$ is zero, we should not insert a value. Considering that the pixels are randomly selected, the practical CR should be larger than the theoretical ones. Another thing should be pointed out is that the interpolated values are estimated values, which may not be equal to the true pixels. As a result, if we compare conventional interpolation with co-prime interpolation, since no complementarity exists in traditional interpolation process, its performance should be worse.

Taking above consideration into account, the practical compression ratio is re-computed in Table 3.1. Comparing these two columns, we find that practical CR

Table 3.2. Compression Ratio with and without co-prime interpolation when different a applies

$a\%$	**CR without interpolation**	**CR with co-prime pair** $(2, 3)$
6%	16.6667	5.6343
8%	12.5000	4.6103
10%	10.0000	3.8039
12%	8.3333	3.6324
14%	7.1429	3.3879
16%	6.2500	3.2213
18%	5.5556	3.1118
20%	5.0000	3.0389

values are greater than the theoretical ones, just as we explained previously. Although the theoretical values are different from the practical ones, the growth trend is the same. Therefore the theoretical values could still provide a guide for us to choose suitable co-prime pairs.

In Table 3.2, when $a\%$ is changed from 6% to 20%, the value of CR is calculated. From Table 3.2 we can see that the compression ratio is decreasing with the increase of $a\%$. If no interpolation method is applied, the CR is listed in the second column and when co-prime interpolation applied, it is given in the third column. We can find that the values in the second column are larger than those in the third column. What's more, the CR gap between the second column and the third column is reducing with the growth of $a\%$. Table 3.2 indicates that if a is very small, the proposed approach CopCS will have a better performance because the compression ratio will be improved more comparing with large a.

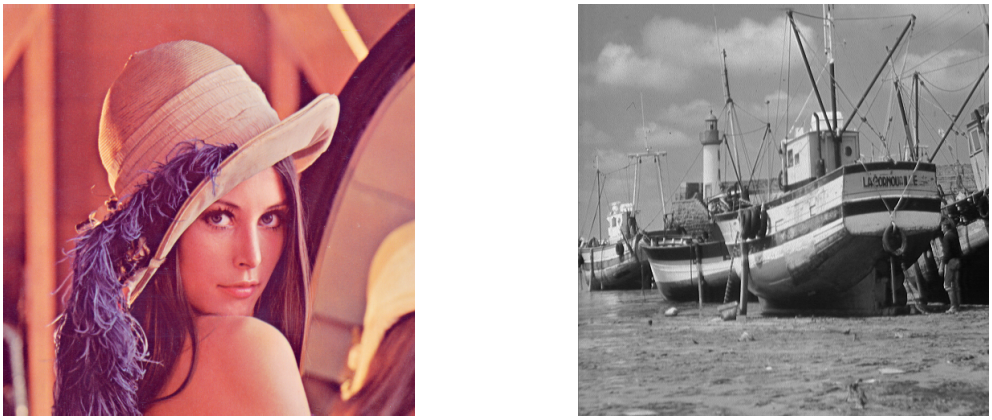

(a) (b)

Figure 3.3. Test images. (a) Lena image (RGB), (b) boat image (black & white).

3.4.3 Simulation Results of Test Images

In order to validate our analysis, we apply the proposed algorithm on two test images. The test images are plotted in Figure 3.3(a) and 3.3(b) respectively. One is an RGB Lena image and the other is a black and white boat image. Both size are 512×512. In Figure 3.4, we show the performance of direct CS method and CopCS method for $a\% = 15\%$ and $a\% = 10\%$ respectively. When $a\% = 15\%$, Figure 3.4(a) and Figure 3.4(b) are the recovered images via direct CS approach and CopCS with co-prime pair equals to $(6, 7)$. If $a\%$ reduces to 10%, the images recovered by the two methods are drawn in Figure 3.4(c) and 3.4(d) individually. It's straightforward to see that Figure 3.4(c) includes a lot of black dots and has a low resolution, while Figure 3.4(d) recovered by CopCS approach has a high resolution and has no black dots. Because $a\% = 10\%$ is very small, the co-prime pair used in Figure 3.4(d) is chosen as $(2, 3)$.

If we use RMSE and PSNR as the comparison standard between Figure 3.3(a) and the recovered images, let $a = 10$ and M_1 from $0, 1, \ldots, 15$, the root mean square

error calculated via regular interpolation and co-prime interpolation is shown in Figure 3.5. $M_1 = 0$ means the direct CS method, which has the highest RMSE. The blue line is regular interpolation method, which only uses f_1 (in Figure 3.2) to recover the image. The red line is co-prime interpolation method, where the co-prime pair is chosen from Table 3.1 ($(8, 9)$ is followed by $(9, 10), (10, 11), \ldots, (15, 16)$) and both f_1, f_2 are used to recovery. From Figure 3.5 we can see that RMSE of co-prime interpolation is smaller than conventional interpolation when compression ratio is the same. Besides, they're both better than direct CS method since the RMSE is reduced by a half.

Figure 3.6 visualizes the PSNR result of direct CS method and CopCS method by choosing a from 6% to 20%. If a is very small, the PSNR difference between direct CS and CopCS is much obvious. For example, when $a\% = 6\%$, CopCS improves the performance about 4 dB. With the increasing of a, the improvement is decreasing. In the scenario with small a, the proposed CopCS algorithm outperforms its counterpart. In addition, Figure 3.6 also proves the analysis of Table 3.2 from the perspective of PSNR.

The proposed CopCS algorithm not only works on RGB images, but also applicable to black and white pictures as shown in Figure 3.7. When $a\% = 10\%$, Figure 3.7(a) is the recovered images via direct CS and the recovered picture through CopCS with co-prime pair $(3, 4)$ is shown as Figure 3.7(b). As we can see from Figure 3.7(a) and Figure 3.7(b), the resolution of CopCS method is much better than the results of direct CS method.

3.5 Application to Greenland Bed Elevation Assessment

In this section, we apply the proposed algorithm to Greenland bed elevation data. Since 1993, the University of Kansas has worked on collecting Greenland bed

elevation and ice thickness data [54][55]. However, even with some interpolation methods, the generated bed elevation and ice thickness maps are still very rough. Figure 3.8 shows the Greenland bed elevation map without interpolation where the area size is about 1.7 million square kilometers and the total number of samples is 357593. The color bar represents the elevation in meters. If we zoom into the red rectangular areas in Figure 3.8 (shown in Figure 3.9(a) and Figure 3.10(a)), we can see that they are sparsely sampled with a very poor resolution. The compression ratio in Figure 3.9(a) and Figure 3.10(a) is about $100 : 11$. In the following simulations, we will apply the proposed method on Greenland bed elevation data so as to improve resolution.

Figure 3.9(b) and Figure 3.10(b) show the two rectangular parts after using interpolation method. It's easy to notice that although after interpolation, the images still look very blurry. We need to apply other approaches to obtain a higher resolution picture from the existing database. Since Figure 3.9(a) and Figure 3.10(a) are treated as under sampled images, compressive sensing can be applied to reconstruct it. So in Figure 3.9(c) and Figure 3.10(c), we firstly show the results of directly applying CS algorithm. As the compression ratio of Figure 3.9(a) and Figure 3.10(a) are too low, direct CS method can't improve the resolution and even has a worse performance than interpolation method shown in Figure 3.9(b) and Figure 3.10(b).

Eventually the proposed CopCS algorithm is utilized and the final images are drawn in Figure 3.9(d) and Figure 3.10(d). The co-prime pair we used in Figure 3.9(d) and Figure 3.10(d) are $(3, 4)$ and $(2, 3)$ respectively. From Figure 9(d) and Figure 3.10(d) we can see that more detailed information are recovered through CopCS, no black dots appeared in the picture and the resolution has been significantly improved.

3.6 Conclusions

Motivated by the recent studies about co-prime down sampling and compressive sensing, a new co-prime interpolation based compressive sensing algorithm is proposed in this paper. Firstly, we demonstrate that co-prime structure has the orthogonal and complementary properties, which are meaningful in reconstructing images. Afterwards, the numerical analysis assisted by RMSE and PSNR of the proposed CopCS algorithm is also provided. When compression ratio is very high, the proposed method will have the best performance comparing with direct CS method and traditional interpolation method.

This algorithm is then validated on two standard test images downloaded from SIPI image database. The recovered images show that CopCS method could further increase the resolution comparing with direct CS method. In addition, the root mean square error and the peak signal-to-noise ratio are also plotted. When the proposed algorithm is used, RMSE of the recovered image becomes lower and PSNR also gets improved. It could be concluded that the proposed CopCS approach can improve the resolution relative to direct CS.

Furthermore, the CopCS has also been tested on real data – Greenland elevation map. For the reason that the collected Greenland bed map are very sparse, if interpolation method or compressive sensing are directly employed on the raw data set, it would generate a very blurry image with a low resolution. However, for CopCS method, we observe that the reconstructed images are much clear than both interpolated images and direct CS recovered images.

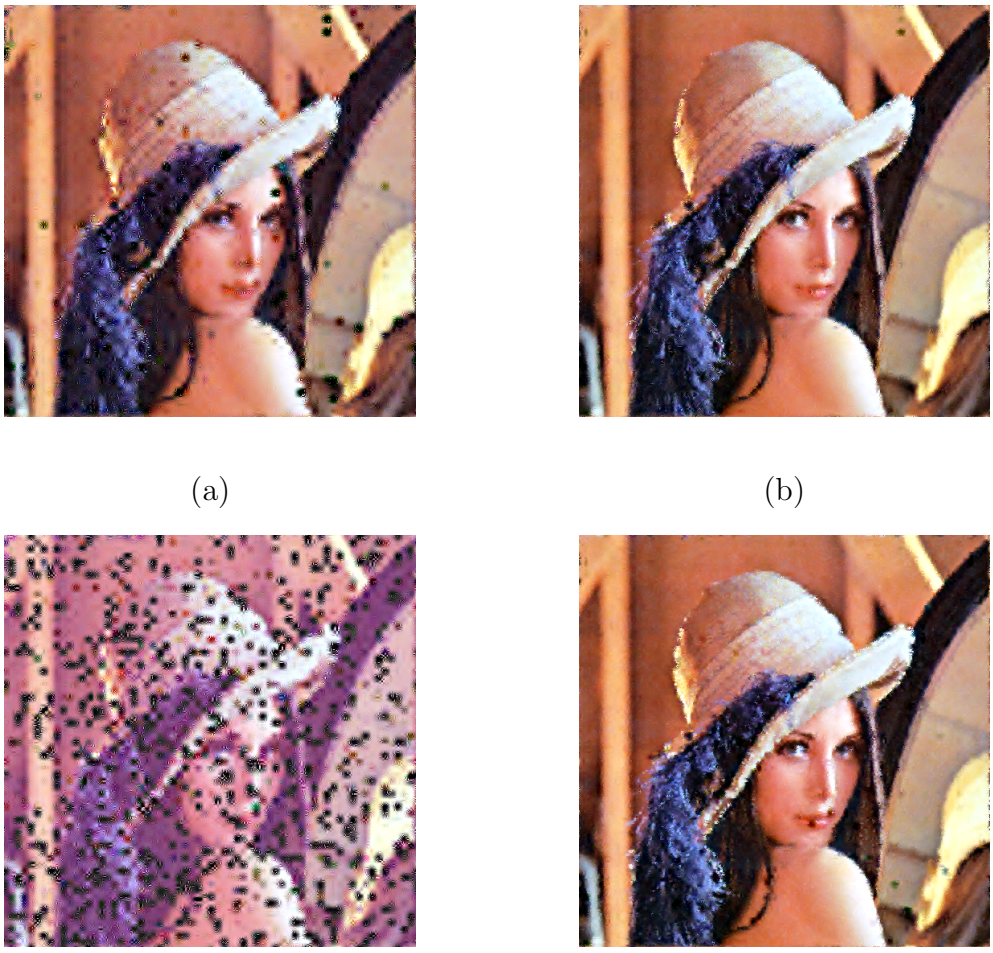

(a) (b)

(c) (d)

Figure 3.4. Comparison between direct CS and CopCS. (a) recovered image via direct CS, $a\% = 15\%$, (b) recovered image via CopCS with $(6, 7)$, $a\% = 15\%$, and (c) recovered image via direct CS, $a\% = 10\%$, (d) recovered image via CopCS with $(2, 3)$, $a\% = 10\%$.

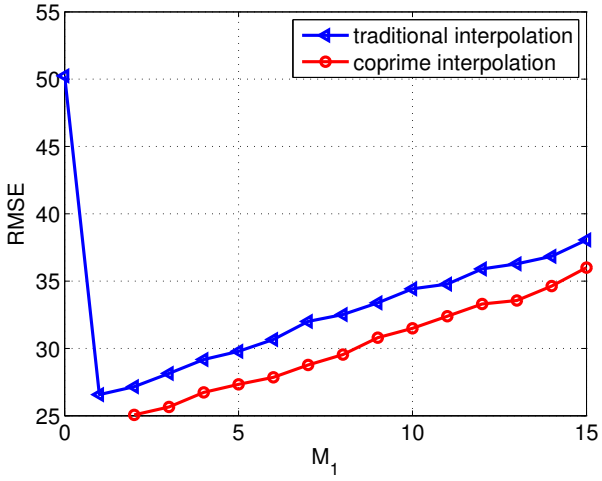

Figure 3.5. Root mean square error when $a\% = 10\%$.

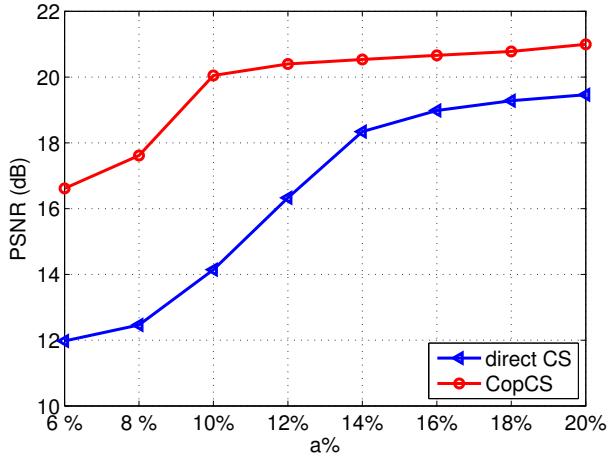

Figure 3.6. Peak signal-to-noise ratio when $a\%$ varies.

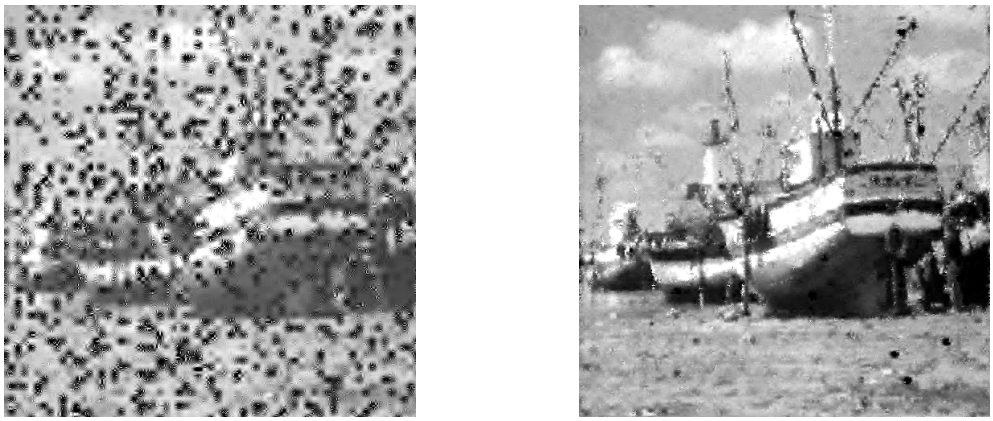

(a) (b)

Figure 3.7. Comparison between direct CS and CopCS, $a\% = 10\%$. (a) recovered image via direct CS, (b) recovered image via CopCS with $(3, 4)$.

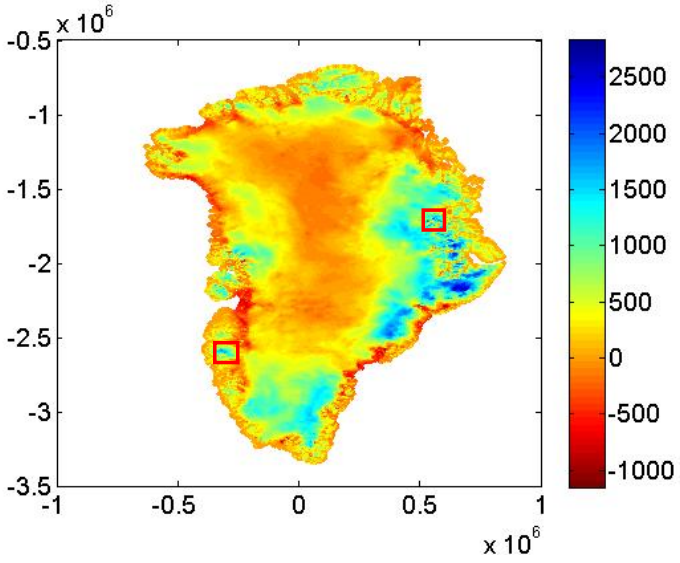

Figure 3.8. Greenland bed elevation map plotted without any interpolation method where the color bar means bed elevation.

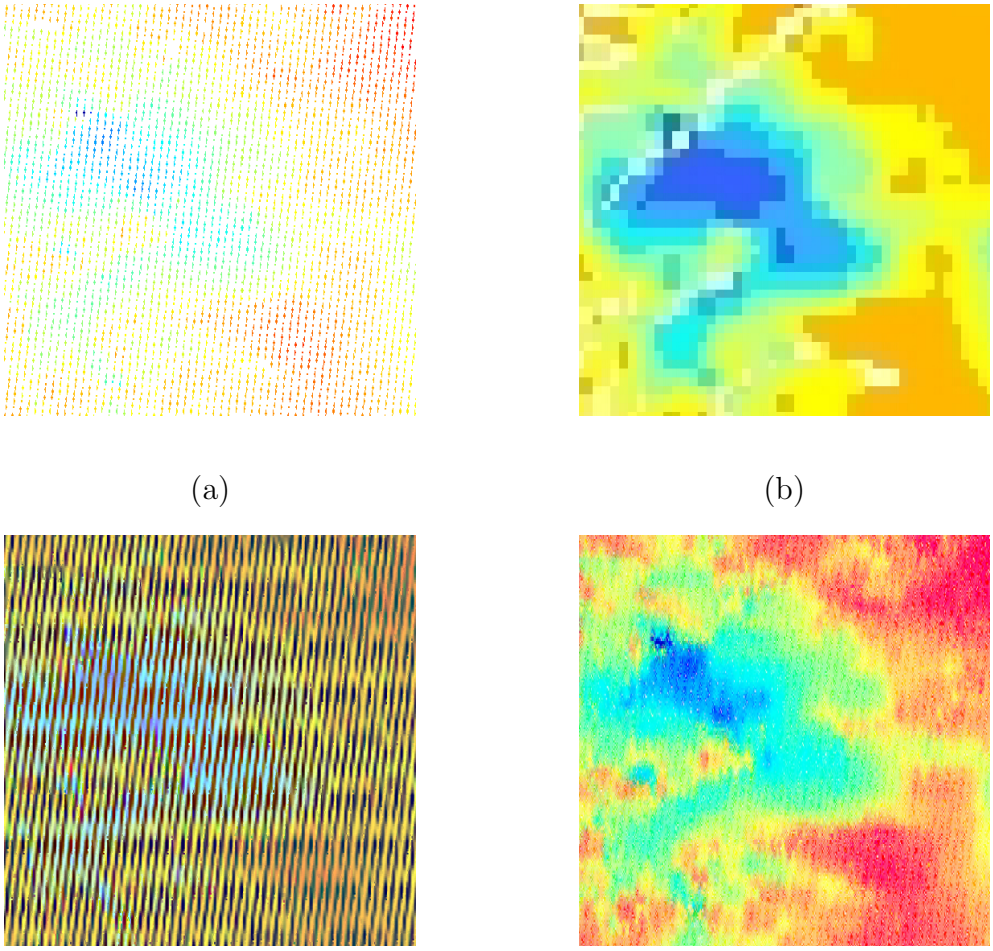

(a) (b)

(c) (d)

Figure 3.9. Recovered images via traditional interpolation method, direct CS method and CopCS method. (a) zoom into the left side in Figure 8, (b) traditional interpolation, (c) direct CS, and (d) CopCS method.

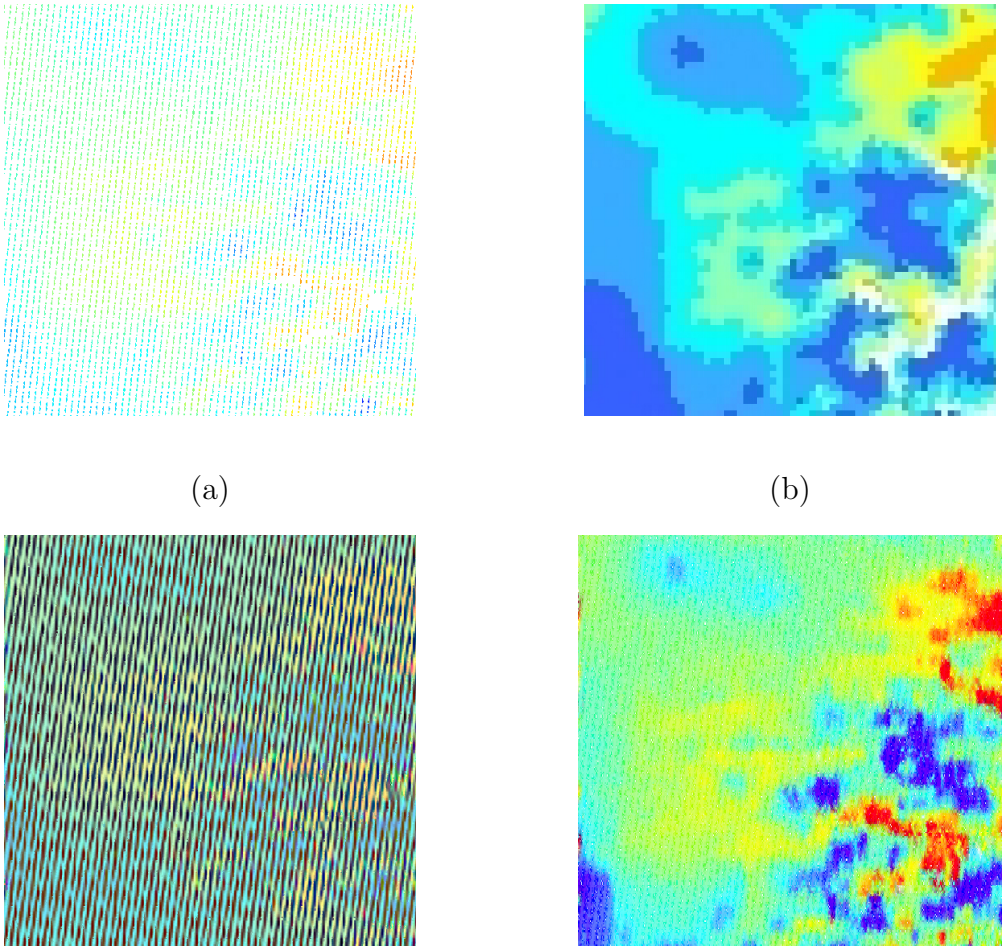

(a) (b)

(c) (d)

Figure 3.10. Recovered images via traditional interpolation method, direct CS method and CopCS method. (a) zoom into the right side in Figure 3.8, (b) traditional interpolation, (c) direct CS, and (d) CopCS method.

CHAPTER 4

DoA Estimation in Underwater Sensor Networks Based on Sparse Array

4.1 Introduction

In underwater sensor array networks (UWSANs), deployment of large scale wireless sensors are constrained by the practicability and power on each sensor. Design of the array involves trade-offs among the geometry and the number of sensors. High resolution of the array needs large aperture while keeping the spacing of the sensors less than half-wavelength. Many researches have proved that the location identification of uncorrelated sources is depending on the size of the array or the rank of the correlation matrix. Some kinds of non-uniform arrays satisfy this requirement, such as minimum redundancy array (MRA), nested array and co-prime array, which can keep the same spatial correlation lags and achieve larger apertures compared to the uniform linear arrays (ULAs). Since there is no closed form expression for MRA, if nested array and co-prime array can be proved efficient in DoA, they are better solutions.

Spectral estimations algorithms such as MUSIC method [56] have been widely applied in high-resolution DoA estimations. It is based on the eigendecomposition of the spatial auto-correlation matrix of the sampled signal. A lot of papers [57]-[59] have presented the wideband MUSIC and narrowband MUSIC performance analysis. In [60], a new approach of array geometry has been reported to improve the efficiency of spectrum estimation based on the augmented matrix. Different from the spatial smoothing MUSIC algorithm of non-uniform arrays [61], augmented matrix approach

has less complexity. Besides, it can find more sources than ULA with the same number of sensors and identify close sources.

In this work, the architecture of UWSAN is built by [62], and each sensor is active, which is able to compute the local direction of arrival and range of the targets. In addition, half of the wavelength λ is assumed to 1 in all the simulations. The statistical analysis of the Bartlett spatial spectrum estimator when utilize an augmented covariance matirx is firstly mentioned in [63]. The Cramér-Rao bound of the classic MUSIC estimation is proposed in [64]. We present the Cramér-Rao bound of the nested and co-prime arrays, which is lower than both ULA and the CRB of the classic MUSIC over non-uniform arrays. Furthermore, other advantages of the new algorithm are also studied, such as the improvement of resolvability of the closely spaced sources and larger range of the signal peaks to the background level.

4.2 2D co-prime array and acoustic model

4.2.1 2D co-prime array

2D co-prime array is based on the 1D co-prime linear array, which is described in definition 2 as follow:

Definition 2. *A 2D co-prime array is the extension of 1D co-prime array, which means that both in x-axis and y-axis, the locations of the sensors are followed by the rule of 1D co-prime array. If the array is under-sampled by the pair (P, Q), the spacing of x-axis and y-axis is d_c respectively.*

For example, we plot the 2D nested array with $\boldsymbol{N^{(d)}} = \begin{pmatrix} 1 & 0 \\ 0 & 1 \end{pmatrix}$, $\boldsymbol{P} = \begin{pmatrix} 3 & 0 \\ 0 & 3 \end{pmatrix}$, $N_1^{(s)} = 2$, $N_2^{(s)} = 3$ in Figure 4.1(a) and an instance of 2D co-prime array in Figure 4.1(c) with the co-prime pair is (2,3).

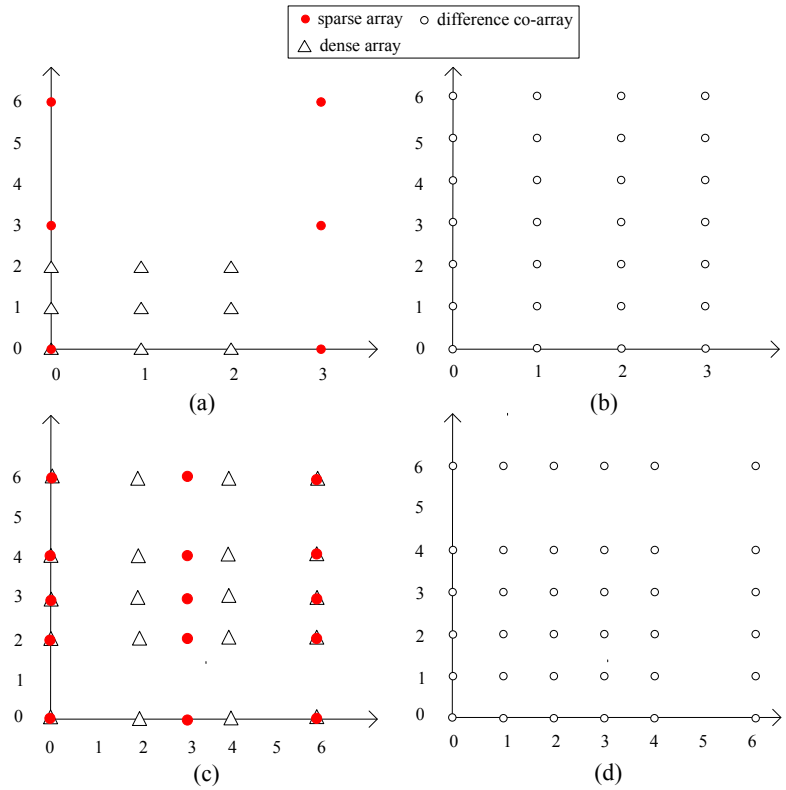

Figure 4.1. Examples of 2D non-uniform arrays. (a) Nested array, (b) difference co-array of (a), (c) Co-prime array, $L = 3$, (d) difference co-array of (c) .

4.2.2 Acoustic model

Assume an underwater wireless sensor array network consists of F sensor arrays and the acoustic signal is narrowband. Each array is 1D or 2D nested array or co-prime array with M sensors as we presented in the former context. The mth $(m = 1, 2, \cdots, M)$ sensor on the pth $(p = 1, 2, \cdots, F)$ array is designated as the (m, p)th sensor.

If the kth target $(k = 1, 2, ..., K)$ emits a signal with a carrier frequency f_0-Hz and the amplitude $a_k(t)$, since $w_0 = 2\pi f_0$, we can express the signal as

$$x_k(t) = a_k(t)e^{jw_0 t} \tag{4.1}$$

At time instant t, the (m,p)th sensor will receive a time delayed and attenuated signal from the target. We assume the noise $n_{mp}(t)$ is zero mean white Gaussian noise and the signal is uncorrelated with noise. The output of (m,p)th sensor will be:

$$y_{mp}(t) = \sum_{k=1}^{K} x_k(t) e^{jw_0\tau_m(\theta_k)} + n_{mp}(t) \tag{4.2}$$

K is the number of targets within the sensor field.

The signal delay of the (m,p)th sensor is represented by τ_{mp}, so the range between the sensor and the kth target can be expressed as:

$$r_k = \frac{\tau_{mp} \times c}{2} \tag{4.3}$$

where c=1500 m/s is the acoustic wave propagation speed in water.

(4.2) can be written in vector form

$$\boldsymbol{Y}(t) = \boldsymbol{A}(\boldsymbol{\theta})\boldsymbol{X}(t) + \boldsymbol{N}(t) \tag{4.4}$$

here $\boldsymbol{A}$ is the $M \times K$ array manifold matrix and each column of $\boldsymbol{A}$ is the steering vector aimed at the K sources direction

$$\boldsymbol{a}(\theta_i) = \begin{bmatrix} e^{jw_0\tau_1(\theta_i)} & e^{jw_0\tau_2(\theta_i)} & \dots & e^{jw_0\tau_M(\theta_i)} \end{bmatrix}^T \tag{4.5}$$

We also take 2D non-uniform array into consideration and the manifold matrix is related with the azimuthal angle θ and elevation angle ϕ, which is given by

$$\boldsymbol{A} = \begin{bmatrix} \boldsymbol{a(\theta_1, \phi_1)} & \boldsymbol{a(\theta_2, \phi_2)} & \cdots & \boldsymbol{a(\theta_K, \phi_K)} \end{bmatrix} \in \mathbb{C}^{2\times K} \tag{4.6}$$

The objective of DoA is to estimate θ_i and ϕ_i. Combined with the range information r_k, the position of the targets can be located.

4.3 Augmented Matrix Approach on Non-uniform Arrays

The classic MUSIC algorithm is based on the eigendecomposition of the correlation matrix R_y, which is

$$\begin{aligned} R_y &= E[\boldsymbol{Y}(t)\boldsymbol{Y}^*(t)] \\ &= \boldsymbol{A}(\boldsymbol{\theta})R_x\boldsymbol{A}^*(\boldsymbol{\theta}) + N_0\boldsymbol{I}_M \end{aligned} \tag{4.7}$$

N_0 is the noise variance, which is equal to σ^2. In practice, for zero mean Gaussian data $\boldsymbol{y}(t_i), i = 1, 2, ..., N$, this is estimated by

$$\hat{R} = \frac{1}{N}\sum_{i=1}^{N}\boldsymbol{y}(t_i)\boldsymbol{y}^*(t_i) \tag{4.8}$$

For linear array, if the noise subspace is denoted by $\boldsymbol{U}_N$, we can calculate the peaks in the estimator function

$$P_{MUSIC}(\theta)_{1D} = \frac{1}{\boldsymbol{a}^H(\theta)\boldsymbol{U}_N\boldsymbol{U}_N^H\boldsymbol{a}(\theta)} \tag{4.9}$$

$\boldsymbol{a}(\theta)$ is defined in (4.5) and $\boldsymbol{a}^H$ means the conjugate transpose of $\boldsymbol{a}$.

However, the spatial spectrum estimation in 2D array is a little different from (4.9), because the Kronecker product is introduced in the description of the array manifold matrix:

$$\boldsymbol{A} = \begin{bmatrix} \boldsymbol{a_y}(\boldsymbol{\theta_1}, \boldsymbol{\phi_1}) \otimes \boldsymbol{a_x}(\boldsymbol{\theta_1}, \boldsymbol{\phi_1}) \\ \boldsymbol{a_y}(\boldsymbol{\theta_2}, \boldsymbol{\phi_2}) \otimes \boldsymbol{a_x}(\boldsymbol{\theta_2}, \boldsymbol{\phi_2}) \\ \vdots \\ \boldsymbol{a_y}(\boldsymbol{\theta_K}, \boldsymbol{\phi_K}) \otimes \boldsymbol{a_x}(\boldsymbol{\theta_K}, \boldsymbol{\phi_K}) \end{bmatrix}^T \tag{4.10}$$

$\boldsymbol{a_x}(\boldsymbol{\theta_K}, \boldsymbol{\phi_K})$ and $\boldsymbol{a_y}(\boldsymbol{\theta_K}, \boldsymbol{\phi_K})$ are the kth vector in matrix $\boldsymbol{A_x}$ and $\boldsymbol{A_y}$. The detail of $\boldsymbol{a_y}$ and $\boldsymbol{a_x}$ is given in (3.12.a) and (3.12.b)[1].

Assume the noise subspace for 2D array is $\boldsymbol{E}_N$, then (3.11) can be expressed as:

[1] (3.12.a) and (3.12.b) are in the next page

$$\boldsymbol{A}_x = \begin{bmatrix} e^{-j2\pi d_0 sin(\phi_1)sin(\theta_1)/\lambda} & e^{-j2\pi d_0 sin(\phi_2)sin(\theta_2)/\lambda} & \dots & e^{-j2\pi d_0 sin(\phi_K)sin(\theta_K)/\lambda} \\ e^{-j2\pi d_1 sin(\phi_1)sin(\theta_1)/\lambda} & e^{-j2\pi d_1 sin(\phi_2)sin(\theta_2)/\lambda} & \dots & e^{-j2\pi d_1 sin(\phi_K)sin(\theta_K)/\lambda} \\ \vdots & \vdots & \ddots & \vdots \\ e^{-j2\pi d_{M_x-1} sin(\phi_1)sin(\theta_1)/\lambda} & e^{-j2\pi d_{M_x-1} sin(\phi_2)sin(\theta_2)/\lambda} & \dots & e^{-j2\pi d_{M_x-1} sin(\phi_K)sin(\theta_K)/\lambda} \end{bmatrix} \tag{3.12.a}$$

$$\boldsymbol{A}_y = \begin{bmatrix} e^{-j2\pi d_0 cos(\phi_1)sin(\theta_1)/\lambda} & e^{-j2\pi d_0 cos(\phi_2)sin(\theta_2)/\lambda} & \dots & e^{-j2\pi d_0 cos(\phi_K)sin(\theta_K)/\lambda} \\ e^{-j2\pi d_1 cos(\phi_1)sin(\theta_1)/\lambda} & e^{-j2\pi d_1 cos(\phi_2)sin(\theta_2)/\lambda} & \dots & e^{-j2\pi d_1 cos(\phi_K)sin(\theta_K)/\lambda} \\ \vdots & \vdots & \ddots & \vdots \\ e^{-j2\pi d_{N_y-1} cos(\phi_1)sin(\theta_1)/\lambda} & e^{-j2\pi d_{N_y-1} cos(\phi_2)sin(\theta_2)/\lambda} & \dots & e^{-j2\pi d_{N_y-1} cos(\phi_K)sin(\theta_K)/\lambda} \end{bmatrix} \tag{3.12.b}$$

$$\begin{aligned} &P_{MUSIC}(\theta,\phi)_{2D} \\ &= \frac{1}{[\boldsymbol{a_y}(\boldsymbol{\theta},\boldsymbol{\phi}) \otimes \boldsymbol{a_x}(\boldsymbol{\theta},\boldsymbol{\phi})]^H \boldsymbol{E}_N \boldsymbol{E}_N^H [\boldsymbol{a_y}(\boldsymbol{\theta},\boldsymbol{\phi}) \otimes \boldsymbol{a_x}(\boldsymbol{\theta},\boldsymbol{\phi})]} \end{aligned} \tag{4.11}$$

From [66] we know that the delay of the signal is related with the location of each sensor (d_i) and the direction θ_k, $k = 1, 2, ..., K$. When we calculate the correlation of ith and jth sensor, since the sources are independent, it will be

$$\begin{aligned} &E[y(t,d_i)y^*(t,d_j)] \triangleq R_y(d_i - d_j) \\ &= \sum_{k=1}^{K} P_k e^{-j2\pi(d_i-d_j)sin(\theta_k)/\lambda} + N_0\delta(i-j) \end{aligned} \tag{4.12}$$

Here P_k represents the power of the kth source. It's clear to see that even though the sensors are sparse, the covariance matrix can still be dense. Furthermore, if the difference co-array is a filled set as a ULA, the estimation performance should be the same while using less number of sensors. Inspired by the augmented matrix approach in [60], which is only applied on the MRA, we extend this algorithm to 1D and 2D nested and co-prime array. First of all, the theorem of the best choice for the nested array and co-prime array is provided.

Theorem 1. *In a linear nested array, the difference co-array is not a filled ULA if there are more than 2 stages of nesting. Besides, if the pair of a linear co-prime array is* $(M_1, M_2, \cdots, M_n)$*, the efficiency will decrease with the increase of* n*.*

Proof. For K-level nested array in [16], the optimum nested array has sensors located at $S_{op} = \{d, 2d, 4d, 8d, \cdots, 2^K d\}$. It's straightforward to see that the co-array is not a filled ULA. For the co-prime array, the efficient rate is defined $f = \sum_{i=1}^{n} \frac{1}{M_i}$, if $n \to \infty$, the efficient rate is 1, which means the number of sensors in the co-prime array is equal to a ULA.

□

As a result, we'd better construct 2-level nested array and co-prime array.

Before deriving the expressions of auto-correlation for nested and co-prime array, there are two properties about the difference co-array:

Property 8. *In 1D situation, a 2-level nested array with* N_1 *and* N_2 *sensors respectively can achieve full coverage in* $[0, N_1 N_2]$*. While for a co-prime array with prime pair* (P, Q)*, there are some 'holes' between 0 and* PQ*. When one sub-array double the number of the sensors, the difference co-array will be a filled set in* $[0, PQ]$*.*

Property 9. *In 2D situation, for the nested array, any point among the sparse array is* $\boldsymbol{N}^{(s)}[k_1\ k_2]^T - \boldsymbol{N}^{(d)}\boldsymbol{n}^{(d)}$ *and there are up to* $N^{(d)} \times N^{(s)}$ *elements. For the co-prime array which is sampled by* (P, Q)*, there are* $(P+Q) \times (P+Q)$ *points filling the array, located within* $FPD(\boldsymbol{V})$*, where* $\boldsymbol{V} = \begin{pmatrix} 0 & 0 \\ PQ & PQ \end{pmatrix}$.

The detailed proof of property 8 is presented in [16][17] and the parameters in property 9 are from section II. It's straightforward to see from Figure 4.1(a) and 4.1(c) that there are more than 1 sensors are located in the same position.

Based on property 8, we can derive the auto-correlation function of 1D sparse array, which is Toeplitz matrix generated by the difference co-arrays. If there are M different values in the co-array, use $r(m)$ to represent the auto-correlation lags, the function is:

$$\begin{aligned} r(n) &= \sum_{k=1}^{K} P_k e^{-j2\pi d_m sin(\theta_k)/\lambda} + N_0\delta(m) \\ n &\in \{0, 1, 2, \cdots, M\} \end{aligned} \tag{4.13}$$

We assume that there is a size of $M_x^s \times N_y^s$ non-uniform 2D array, from the second property, it can be equal to a size of $M_x \times N_y$ filled 2D array and the covariance of ith column of $\boldsymbol{A}$ and jth row of $\boldsymbol{A}^H$ is

$$\begin{aligned} r(n') &= \sum_{k=1}^{K} P_k e^{j(d_i - d_i')w_{1k} + j(d_j - d_j')w_{2k}} + N_0\delta(n) \\ i' &\in \{0, 1, 2, \cdots, N_y^s\} \\ j' &\in \{0, 1, 2, \cdots, M_x^s\} \\ n' &\in \{0, 1, 2, \cdots, M_x N_y\} \end{aligned} \tag{4.14}$$

Here

$$w_{1k} = \frac{2\pi}{\lambda} sin(\phi_k) sin(\theta_k) \tag{4.15}$$

$$w_{2k} = \frac{2\pi}{\lambda} cos(\phi_k) sin(\theta_k) \tag{4.16}$$

As a result, we form the Toeplitz matrix of size $(M_x N_y + 1) \times (M_x N_y + 1)$ as:

$$R_{2D} = \begin{pmatrix} r(0) & r(1) & \cdots & r(M_x N_y) \\ r^*(1) & r(0) & \cdots & r(M_x N_y - 1) \\ \vdots & \vdots & & \vdots \\ r^*(M_x N_y) & r^*(M_x N_y - 1) & \cdots & r(0) \end{pmatrix} \tag{4.17}$$

4.4 Statistic Analysis of Non-uniform Arrays

The ability to place a lower bound on the DoA mean square error of any unbiased estimators is extremely necessary in practice. On the other hand, it helps us to determine which estimator is most efficient and accurate. In this section, we analyze the improvement of CRB over non-uniform arrays.

In [64], the authors derived the conditional CRB for the covariance error of a uniform linear array as shown below

$$CRB \approx \frac{6}{m^3 SNR} \tag{4.18}$$

and m is calculated by

$$m = \boldsymbol{A}^H \boldsymbol{A} \tag{4.19}$$

If the ULA is replaced by the nested array or co-prime array, it means that fewer real sensors but more virtual sensors are used. As a result, for the 1D sparse array, the expression of CRB becomes:

$$CRB = \frac{1}{2SNR}[\boldsymbol{D}^H(\boldsymbol{I} - \boldsymbol{A}(\boldsymbol{A}^H \boldsymbol{A})^{-1}\boldsymbol{A}^H)\boldsymbol{D}]^{-1} \tag{4.20}$$

here $\boldsymbol{D}$ is the first-order derivative of $\boldsymbol{A}$.

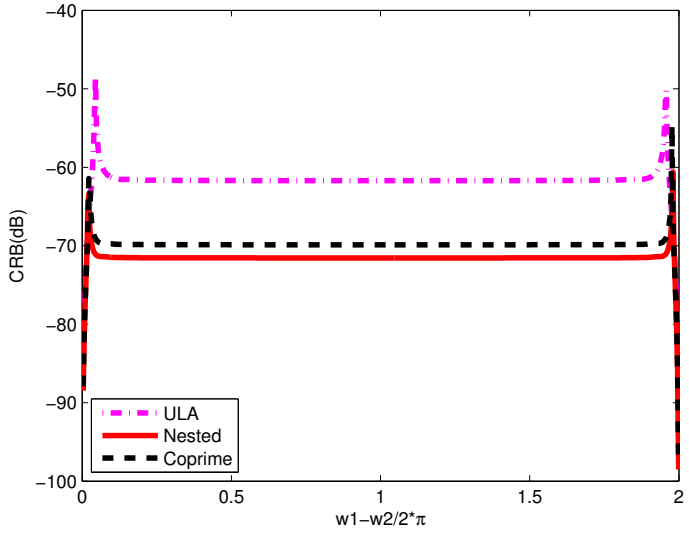

Figure 4.2. CRB comparison between 1D non-uniform arrays and uniform linear array.

In Figure 4.2, we show the CRBs of non-uniform arrays and the ULA. Assume there are two sources w_1, w_2 with SNR=0 dB, and the number of the sensors is 20. It's straightforward to see that the CRBs in the non-uniform arrays are much lower than the ULA. This is because the aperture in non-uniform arrays are larger than uniform spaced array.

Moreover, the asymptotic CRB for 2D DoA estimation can be found in [67], which illustrates that if the sensor locations are optimized with respect to both x-axis and y-axis, the CRB will be minimized.

4.5 Simulation Results

In this section, we perform several simulations to prove the advantages of this new algorithm. First of all, in both 1D and 2D non-uniform arrays, it can detect

more sources with fewer sensors. Moreover, since the aperture in the non-uniform array is larger than the uniform array, it can identify close sources.

In the first simulation, we generate three linear arrays as:

$$ULA = [0 \quad 1 \quad 2 \quad \cdots \quad 12]$$

$$nested\ array = [1 \quad 2 \quad 3 \quad 6 \quad 9 \quad 10 \quad 11 \quad 12]$$

$$coprime\ array = [0 \quad 2 \quad 3 \quad 4 \quad 6 \quad 8 \quad 9 \quad 12]$$

Notice that in every non-uniform array, it contains 8 sensors, but ULA has 13 sensors. This is because the non-uniform arrays can achieve the same performance of the ULA based on the difference co-arrays. In the non-uniform arrays, $(N_1, N_2) = (2, 3)$ and $(P, Q) = (2, 3)$. The detected sources are at $[0.4\ 0.5\ 0.6\ 0.7\ 0.8\ 0.9\ 1.2]\ \times\pi$, so $K = 7$. We know that a linear array can't find targets more than the number of the sensors, for instance, the ULA in the first simulation can at most detect 12 sources, the ratio between sources and sensors is $\frac{12}{13}$. However, this ratio in non-uniform arrays is $\frac{11}{8}$, which is greater than 1 and it indicates that nested array and co-prime array are more efficient in the detection. The result is plotted in Figure 4.3.

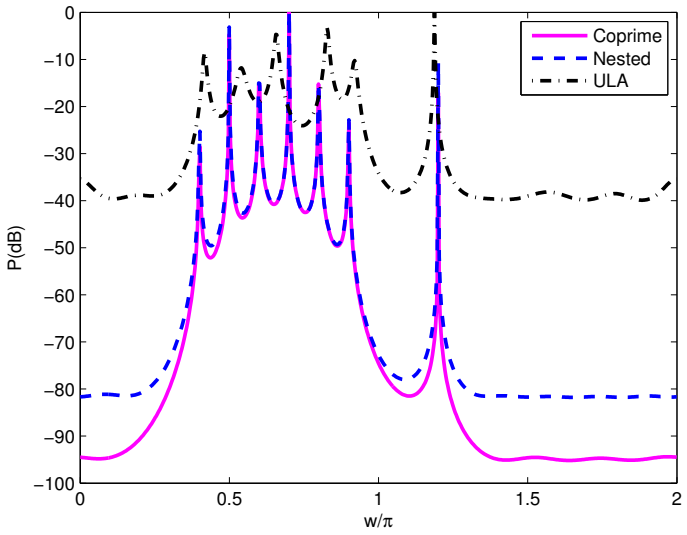

Figure 4.3. DoA estimation by the uniform linear array and non-uniform linear arrays and the SNR is 0 dB ($P_k/\sigma^2 = 1$).

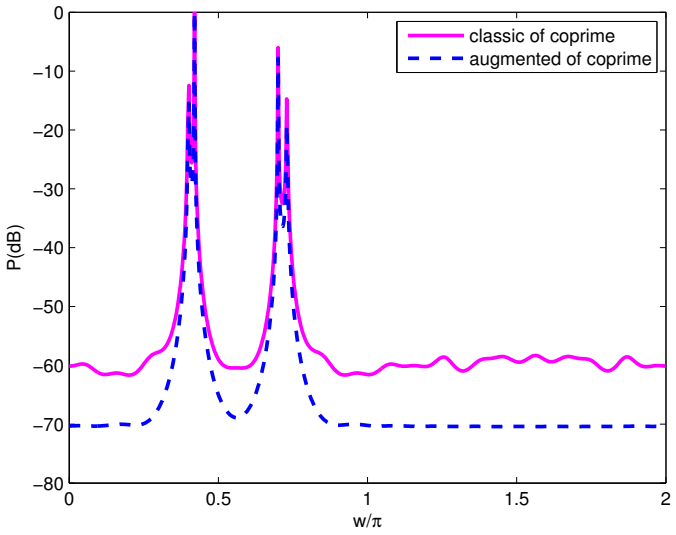

Figure 4.4. DoA estimation of close sources, co-prime array= [0 2 4 6 8 5 10 15 20].

The ULA is applied with the classic MUSIC method, however, it just detect six sources. The nested array and co-prime array successfully find all the sources in the range. In addition, the dynamic range of the signal peaks to the background level is larger in the augmented matrix approach.

In Figure 4.4 and Figure 4.5, we draw the DoA estimation of closely spaced sources, both classic MUSIC method and augmented matrix approach are used. There are four sources at [0.4 0.42 0.7 0.73] $\times\pi$, which contains two pairs of near spaced angles. The locations of the arrays are given in Figure 4.4 and Figure 4.5. The result shows that ULA can not resolve the sources but co-prime array with classic MUSIC and augmented matrix approach can successfully distinguish four sources, which is because that it has about 2.5 times larger aperture than the ULA.

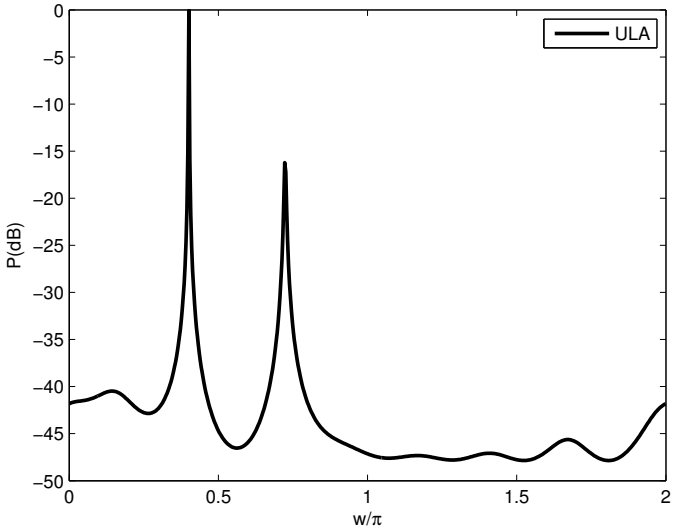

Figure 4.5. DoA estimation of close sources, ULA=[0 1 2 3 4 5 6 7 8].

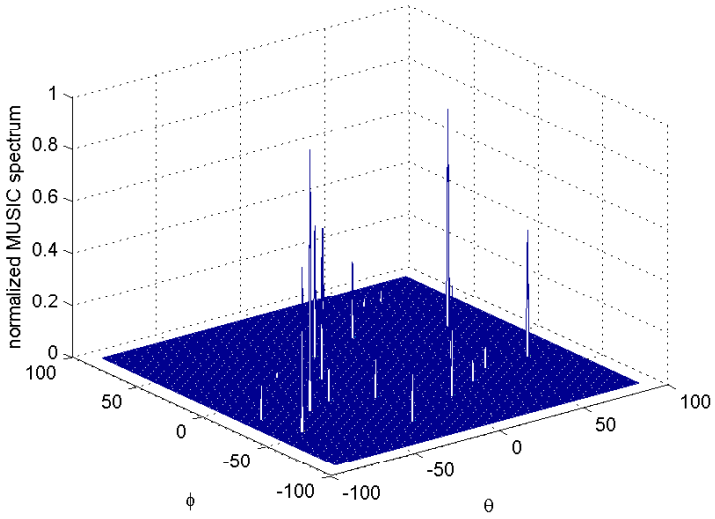

(a)

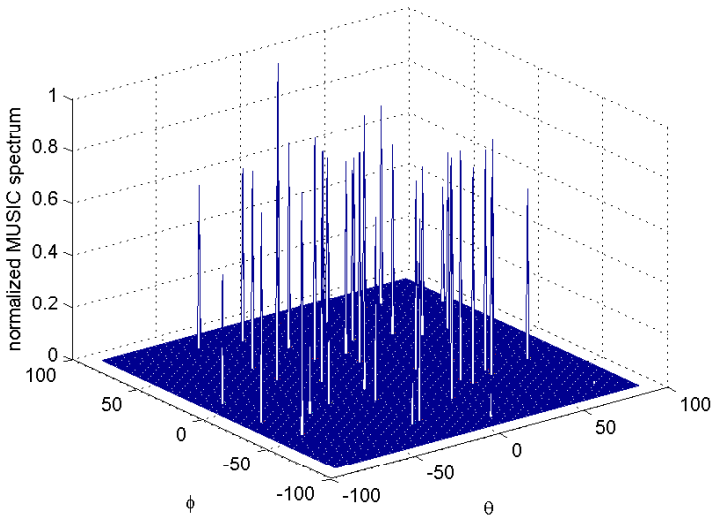

(b)

Figure 4.6. DoA estimation of 2D non-uniform nested arrays and the SNR is 0 dB, (a) detect 20 sources with 14 sensors, (b) detect 38 sources with 26 sensors.

The DoA evaluation over the 2D non-uniform array is a little complicated, as there are two parameters need to be estimated. In Figure 4.6(a), we show an example of 2D nested array, which is as illustrated in Figure 4.1(a). There are $det(\boldsymbol{P}) = 9$

sensors in the dense array and $N^{(s)} = 6$ sensors in the non-uniform array. Because both the non-uniform array and the dense array has the sensor locating at $(0, 0)$, there are total 14 sensors in the nested array. From property 9, this nested array is equal to a filled rectangular array with $4 \times 7 = 28$ sensors. Randomly distributed 20 (>14) sources in the range, the augmented matrix MUSIC approach of DoA estimation result is plotted.

If we increase the number of sensors in the range, more sources can be detected. For instance, $\boldsymbol{N^{(d)}} = \begin{pmatrix} 1 & 0 \\ 0 & 1 \end{pmatrix}$, $\boldsymbol{P} = \begin{pmatrix} 3 & 0 \\ 0 & 3 \end{pmatrix}$, $N_1^{(s)} = 3$, $N_1^{(s)} = 6$. There are 26 sensors in the nested array and can replace the performance of $16 \times 7 = 105$ sensors of the uniform distributed array. Assume there are 38 random sources, the result is shown in Figure 4.6(b).

4.6 Conclusion

In this work, we extend the augmented matrix approach from minimum redundancy array to 1D and 2D nested array and co-prime array in order to estimate the location of the targets. We also provide the structure definitions of these non-uniform arrays, which have not been given in the MRAs. It's clear to see that the nested and co-prime arrays are able to save the number of sensors. Moreover, accuracy is improved for the reason of large apertures and CRB in the non-uniform array is also decreased significantly.

The results indicate that this method can successfully detect the sources, even the number of sources is larger than the number of the sensors in the array. This algorithm is less complicated than the spatial smoothing DoA estimation, maintaining the same properties. Besides, the dynamic range of the signal peaks to the background level is larger in augmented matrix approach, which helps search the sources locations.

In 2D non-uniform arrays, the random distributed sources will affect the amplitudes of the estimation function.

CHAPTER 5

Underwater Mobile Co-prime Sensor Array for Angle of Arrival Estimation Based on Space-Domain Sensor Synthesis

5.1 Introduction

Underwater acoustic is a part of human activities and plays an important role both in science, industry and military. Acoustic signal is transmitted and finally reflected by the target, experiencing attenuated, deformed and overlaid with noise. It can be received by an array made of several active sonars or passive sonars. In Figure 5.1, the example of active sonar array and passive sonar array is plotted [72]. The classic problem in array signal processing is to estimate the angle of arrivals from the targets. Many existing papers are working on fixed position of sensors, named time-invariant array while in underwater environment, the array sometimes is placed on a moving platform (like AUV). In this paper, we focus on this kind of time varying array. The synthetic aperture radar is widely used in radar image formation and this concept of synthetic aperture processing also extends to sonar system [73] - [75].

Considering about the high expense of sonars and other limitations, sparse array is preferred to do the target localization. In [15] and [60], minimum redundancy array (MRA) is proposed and applied on direction of arrival estimation, which achieved a better performance than uniform linear array (ULA). The authors in [16] and [17] built two kinds of sparse arrays, namely nested array and co-prime array. Different from MRA, the closed form of sensor allocation in nested array and co-prime array is provided. In this work, the angle of arrival is studied based on the structure of co-prime array which can be extended to nested array as well. We assume the sensors

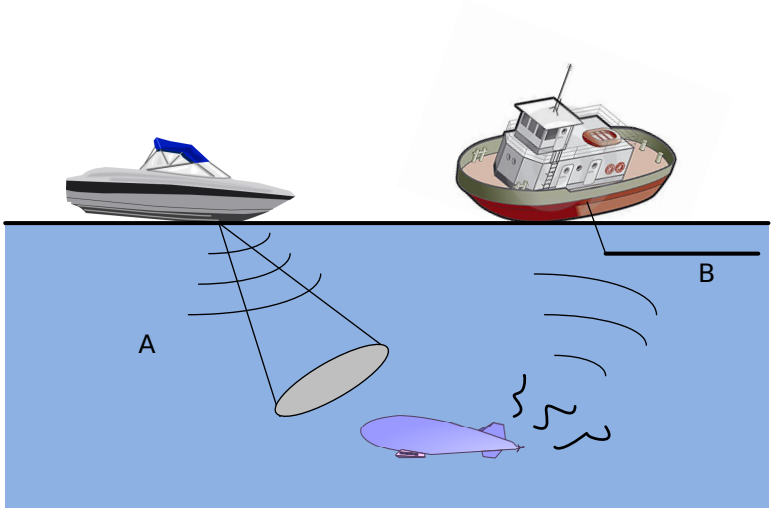

Figure 5.1. Example of sonar: A. active sonar; B. passive sonar .

are deployed as a two-level co-prime array with pair (M, N), where M, N are co-prime and the absolute values of difference co-array are calculated by

$$|Mk_1 - Nk_2|, 0 \leq k_1 \leq N-1, 0 \leq k_2 \leq M-1 \tag{5.1}$$

The example of a two-level co-prime array is shown in Figure 5.2.

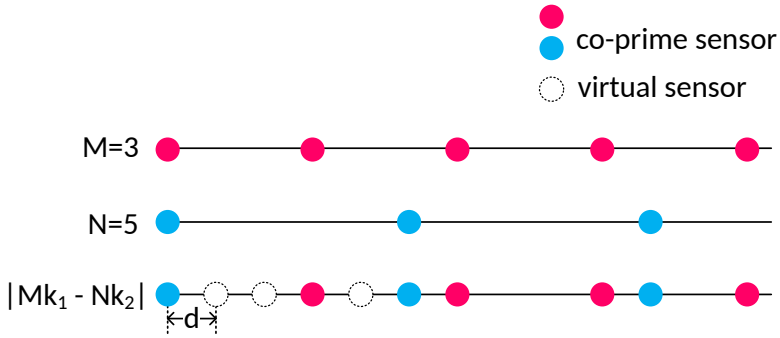

Figure 5.2. Example of 2-level co-prime array. .

In the tutorial paper [76], the author overviewed different high-resolution array processing algorithms for uncorrelated signal problem, such as maximum-likelihood

method, linear-prediction method and eigenvector method. The authors in [77] also applied augmented matrix approach on 1D and 2D sparse arrays. When the signal is coherent, several approaches have been developed in [78] and [79]. In [80], the author considered two situations when the directions of arrival are invariant or change during the observation period. The motivation of this paper is to localization underwater targets based on a co-prime array and meanwhile take advantage of the platform mobility to form a larger synthetic aperture.

Chapter 5 is organized as follows. In Section 5.2, we formulate the model of co-prime sonar array in motion. Then in Section 5.3, a new algorithm named space-domain sensor synthesis (SDS) algorithm and the gradient descent algorithm are introduced. After that in Section 5.4, multiple signal classification (MUSIC) method is applied on the spectral estimation based via augmented matrix. Some simulation results are presented in Section 5.5 and the conclusions are drawn in Section 5.6.

5.2 Sonar Array Motion Model Formulation

We assume the sensors are deployed as a two-level co-prime array with pair (M, N), where M and N are co-prime and the length of the array is $M + N$. At time instant t, each sensor position is $d_i, i = 0, 1, \ldots, M + N - 1$. If the kth target $(k = 1, 2, ..., K)$ emits a signal with angle θ_k and speed of the array is v, the signal received by the ith sensor is

$$y_i(t) = \sum_{k=1}^{K} x_k[t + \frac{(d_i + vt) \times cos\theta_k}{c}]e^{-j(d_i+vt)\cdot 2\pi sin\theta_k/\lambda} \tag{5.2}$$

Here λ stands for the carrier wavelength and c is acoustic speed in underwater. When it's narrowband signal, the second item in x_k could be ignored. Supposing that

the sensor array moves at a constant velocity v in the direction of the array placed as shown in Figure 5.3 and the additive noise is $N_m(t)$, (5.2) is reduced to

$$y_i(t) = \sum_{k=1}^{K} x_k(t) e^{-j(d_i+vt)\cdot 2\pi sin\theta_k/\lambda} + N_m(t) \tag{5.3}$$

In underwater environment, the noise can be grouped in four categories: ambient noise, self-noise, reverberation and acoustic interference. For majority of cases, we shall consider the noise degrading the nominal sonar performance as a random process. As a consequence, $N_m(t)$ is statistically independent of the signal. First if we let $v = 0$ in (5.3), for uncorrelated source, the correlation of the received signal is obtained as

$$\begin{aligned}
(R_{yy})_{ij} &= E\left[y_i(t) y_j^*(t)\right] \\
&= \sum_k \sum_l E\left[x_k(t) x_l^*(t)\right] e^{-j(d_i sin\theta_k - d_j sin\theta_l)2\pi/\lambda} + \sigma_n^2 I \\
&= \sum_k \sigma_k^2 e^{-j(d_i-d_j)2\pi sin\theta_k/\lambda} + \sigma_n^2 \delta(i-j)
\end{aligned} \tag{5.4}$$

where σ_k^2 is the variance of the kth process and σ_n^2 is the variance of the noise.

Observe (5.3), the sensor locations $d_i + vt$ is updating with time t because of array movement. Since the array moves in a straight line, the other variables in (5.3) would keep the same. Depending on this rule, we proposed a space-domain synthesis algorithm which is introduced in next section.

5.3 Space-Domain sensor Synthesis

From Figure 5.2, it's straightforward to see that if we only choose $M + N - 1$ sensors (because location 0 is overlapped), there would be some holes in the virtual array in the range $[0, MN - 1]$. Some authors suggest to double one of the array size

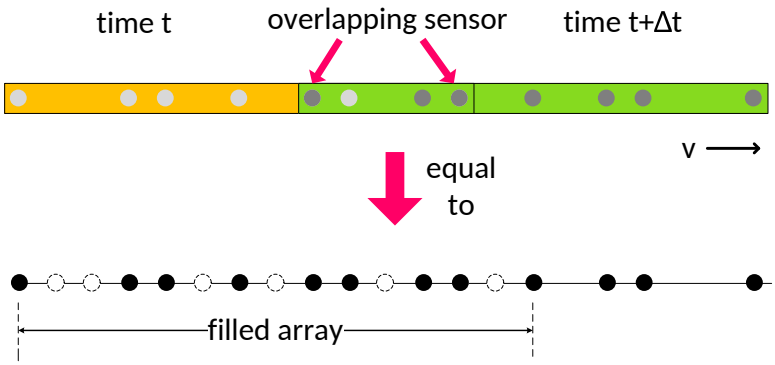

Figure 5.3. Mobility of co-prime array $(M, N) = (3, 4)$ and 1-step space-domain synthesis (SDS). .

in order to achieve a hole-free linear array, however, this would not be necessary when the array is in motion. For a moving array, the new information can be added to the former data with the estimation of time delay and it's possible to build a filled virtual array of $MN + 1$ sensors based only on $M + N$ physical sensors. Furthermore, if we continue adding the new received signals to the existing data, a much longer virtual array can be obtained. This process is similar to the synthetic aperture processing and in this paper, we call it as space-domain synthesis (SDS).

Assume at time instant t, the sensors are placed at $d_i, i = 0, 1, \ldots, M + N - 1$ and after an interval $\Delta\tau$, the array moves to a new position which is $v \times \Delta\tau = 2Nd$ (d is the inter-element spacing which equals to $\frac{\lambda}{2}$) away from the former location. As shown in Figure 5.3, if $M = 3, N = 4$, at time t, the sensors are located at $d\times$[0 3 4 6 8 9 12]. After the array moves, the new positions for the sensors are $d\times$[8 11 12 14 16 17 20]. The goal is to formulate an array with sensors at $d\times$[0 3 4 6 8 9 12 16 20], as a result, at time $t + \Delta\tau$, we need to extract the signal of sensors at $d\times$[16 20] and synthesizes it with the signal received at time t.

Lemma 1. *Let prime integer $N > M$ and the sparse array with spacing N has $M+1$ sensors, after the array moves distance of $(M-1)N \times d$ or $MN \times d$, the difference co-array would be a hole-free one in the range $[0, MN]$.*

Proof. Suppose at time t in the array of spacing N, the last sensor locates at MN. After time interval $\Delta\tau$, the new position of the last sensor becomes $MN+(M-1)N = 2MN-N$ or $MN+MN = 2MN$. If we divide it by N, the number of the sparse array is $2M$ or $2M+1$, both are at least twice of the number M which is the requirement to form a filled virtual array. □

Moreover, we can extend the 1-step SDS to multiple steps SDS.

Lemma 2. *If in 1-step SDS, the co-prime array moves distance of $(M-1)N \times d$. Then in the P steps SDS process, the array moves distance of $(M-1)N \times d \times P$ and the difference co-array would be a hole-free one in the range $[0, MN+(M-1)N \times (P-1)]$.*

Proof. It's easy to prove Lemma 2 because in 1-step SDS, the filled virtual array ranges from $[0, MN]$ and in each another $(P-1)$ SDS steps, this virtual array is still hole-free but moves $(M-1)N \times d$ away in each period. As a result, after P steps SDS, The whole difference co-array is filled in the range $[0, MN+(M-1)N \times (P-1)]$. □

When the array moves during period $\Delta\tau$, from (3) we know that at time $t+\Delta\tau$, the received signal is

$$\begin{aligned} &y_i(t+\Delta\tau) = \\ &\sum_{k=1}^{K} s_k(t+\Delta\tau) e^{-j(d_i+vt)\cdot 2\pi sin\theta_k/\lambda} + N_m(t+\Delta\tau) \end{aligned} \tag{5.5}$$

where

$$s_k(t+\Delta\tau) = x_k(t+\Delta\tau) e^{-jv\Delta\tau\cdot 2\pi sin\theta_k/\lambda} \tag{5.6}$$

Observe (5.3) and (5.5), the only inequality part is the phase shift $s_k(t + \Delta\tau)$. If we can estimate the phase delay between $y_i(t)$ and $y_i(t + \Delta\tau)$, it's easy to interleave signal at different moment into one set. In [81], the author proposed a way to evaluate the phase correction when the signal frequency ω_0 is known and in a noise free environment, which equals to $\omega_0\Delta\tau$. However, in real world, since the received signal is involved with noise and for the passive sonar, the signal frequency may be unknown, it's impossible to evaluate the phase shift directly.

In order to solve the problem, we propose an estimation method based on the gradient descent. In Figure 5.4, it shows the basic idea of this algorithm. For any signal, the maximal value of the auto-correlation is $R(0)$ and the first-order of R is one-direction. As a consequence, if we move the signal with various time delay, the auto-correlation result of the signal and its delay will increase to the maximal value then decrease. When the trend becomes reduce, the algorithm can stop and the time delay is found.

But from (5.4), even though the time delay $\Delta\tau$ is obtained, the arriving angle θ_k is still unknown. So as to make the problem easy to solve, there are some overlapping sensors during the interval when array is moving. For example, in Figure 5.3, at time $t + \Delta\tau$, the sensors moves from $d\times$[0 3 4 6 8 9 12] to $d\times$[8 11 12 14 16 17 20]. There are two overlapping locations $d\times$[8 12] and the signal received by the sensor at $d\times$[8] can be expressed as

$$\begin{aligned} y_4(t) &= \sum_{k=1}^{K} x_k(t) e^{-j(8\cdot\lambda/2)\cdot 2\pi sin\theta_k/\lambda} + N_m(t) \\ &= \sum_{k=1}^{K} x_k(t) e^{-j8\pi sin\theta_k} + N_m(t) \end{aligned} \tag{5.7}$$

and

$$
\begin{aligned}
& y_0(t+\Delta\tau) \\
&= \sum_{k=1}^{K} x_k(t+\Delta\tau) e^{-j(0+8\cdot\lambda/2)\cdot 2\pi sin\theta_k/\lambda} + N_m(t+\Delta\tau) \\
&= \sum_{k=1}^{K} x_k(t+\Delta\tau) e^{-j8\pi sin\theta_k} + N_m(t+\Delta\tau)
\end{aligned}
\tag{5.8}
$$

As a result, the cross-correlation of (5.7) and (5.8) can be used to estimate the phase shift and the maximum value represents the time delay.

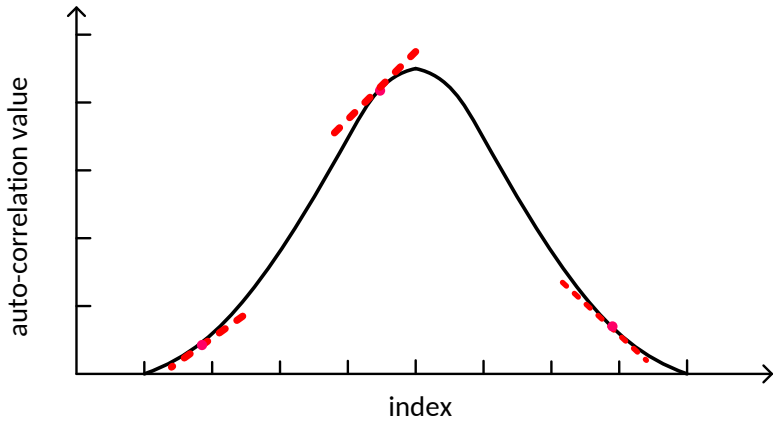

Figure 5.4. Gradient descent algorithm of auto-correlation function. .

The specific procedures of SDS algorithm could be presented as following:

Step 1: Collect the signal at time t and then move the co-prime array $(M-1)N \times d$ or $MN \times d$ away.

Step 2: Use the signal received by overlapping sensors to estimate the time delay. The delay is calculated through the cross-correlation of the signal.

Step 3: Remove the delay in the new signal and only choose the information from sensors with spacing N to interleave with the former information.

After the three steps above, a long synthetic aperture is formed and on the space-domain synthetic array, the difference co-array can be calculated, which would be applied on the spectral estimation. For a P-step SDS co-prime array, if the phase shift in each step is represented as $\Psi_p(p = 1, 2, \ldots, P)$, the synthetic signal can be expressed as

$$y_i'(t) = y_i(t) + \sum_{p=1}^{P} e^{-j\Psi_p} y_i(t + p\Delta\tau) + N_m'(t) \tag{5.9}$$

5.4 Spectral estimation on augmented matrix

If $v = 0$, the array manifold matrix as provided in Section 5.2 is

$$A(\theta_k) = \left[1, e^{-jd_1 2\pi sin\theta_k/\lambda}, \cdots, e^{-jd_{M+N} 2\pi sin\theta_k/\lambda}\right]^T \tag{5.10}$$

In a moving environment, for 1-step SDS, the expression in (5.10) can be modified to

$$\begin{aligned} \tilde{A}(\theta_k) &= e^{-jv\Delta t 2\pi sin\theta_k/\lambda} A(\theta_k) \\ &= \left[e^{-jv\Delta t 2\pi sin\theta_k/\lambda}, e^{-j(d_1 + v\Delta t) 2\pi sin\theta_k/\lambda}, \right. \\ &\quad \left. \cdots, e^{-j(d_{M+N} + v\Delta t) 2\pi sin\theta_k/\lambda}\right]^T \end{aligned} \tag{5.11}$$

Then the auto-correlation function of the synthetic received signal is

$$
\begin{aligned}
(\tilde{R}_{y'y'})_{ij} &= E\left[y'_i(t)y'^{*}_j(t)\right] \\
&= \tilde{A}R_{xx}\tilde{A}^{*} + \sigma_n^2 I' \\
&= \tilde{A}\begin{pmatrix} \sigma_1^2 & & & \\ & \sigma_2^2 & & \\ & & \ddots & \\ & & & \sigma_{MN+1}^2 \end{pmatrix}\tilde{A}^{*} + \sigma_n^2 I'
\end{aligned} \tag{5.12}
$$

where R_{xx} is the source correlation matrix and I' is the augmented identity matrix.

In [17], the difference co-array is calculated as in (5.1) and thus, we can form a Toeplitz matrix based on the difference co-array as

$$
\tilde{R}_{y'y'} = \begin{pmatrix} r(0) & r(1) & \cdots & r(MN) \\ r^{*}(1) & r(0) & \cdots & r(MN-1) \\ \vdots & \vdots & & \vdots \\ r^{*}(MN) & r^{*}(MN-1) & \cdots & r(0) \end{pmatrix} \tag{5.13}
$$

where $r(m)$ is

$$
r(m) = \sum_k \sigma_k^2 e^{-jm2\pi sin\theta_k/\lambda} + \sigma_n^2, m = 0, 1, 2, \ldots, MN \tag{5.14}
$$

If we apply multiple signal classification algorithm (MuSIC) on the augmented matrix $\tilde{R}_{y'y'}$, when the separation of eigenvectors is accurate into signal subspace and noise subspace, it can successfully detect all the sources.

5.5 Simulation results

In order to figure out the performance of the proposed time delay estimation algorithm, we apply it on two co-prime arrays: [0 3 4 6 8 9 12] and [0 3 5 6 9 10

12 15]. In Figure 5.5, the time-delay estimation error is calculated by 1000 Monte-Carlo simulations for each array when the SNR ranges from -10 to 15.In addition, the time delay assumed is 100 samples. It indicates that with the increase of SNR, better estimation result can be achieved and in fact, when the SNR is greater than 0, the error is mostly around 1 sample. This is because that if there's no noise in the received signal, it should be periodic. After cross-correlation, the peak should appear at the right estimation time-delay moment. Since the signal is periodic, there would be several peaks in the result. Even if considering the noise environment, for some peaks, it should still have the largest value among the set because the noise is random.

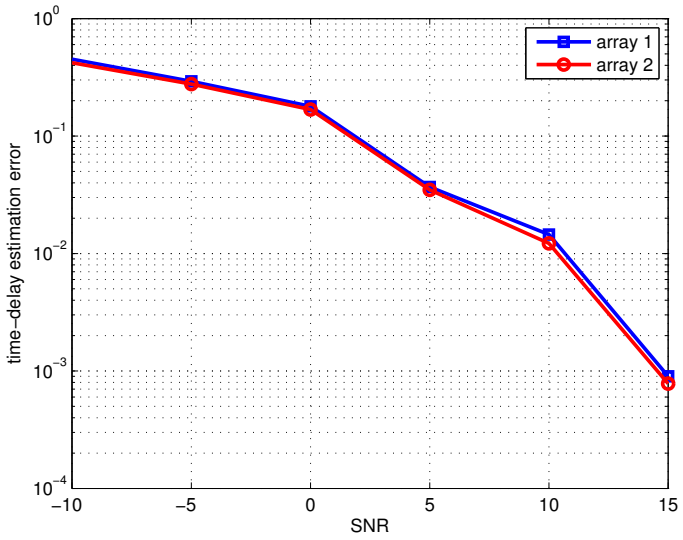

Figure 5.5. Estimation error of co-prime arrays. .

In a second experiment, we compare the moving co-prime array with static co-prime array. First, an 8 physical sensor co-prime array with $M = 3$, $N = 5$ is formed which is the same as the array 2 in the Figure 5.5. The virtual sensor number

are 16 and 8 respectively when the array is in motion or not. The signal-to-noise ratio is set to 0 and three sources are in the filed, they are $\theta_1 = -45°$, $\theta_2 = -10°$, $\theta_3 = 30°$. During the period of 5λ when platform is moving, two sets of data are collected at different locations. Assume the source signal is independent and a total of 500 snapshots are used in the estimation. As shown in Figure 5.6, when the co-prime array is in motion, the dynamic range from the signal peaks to the background level is larger than the array without motion. Besides, because the source number is much less than the virtual sensor number, in both situations, it can accurately find the direction of arrivals.

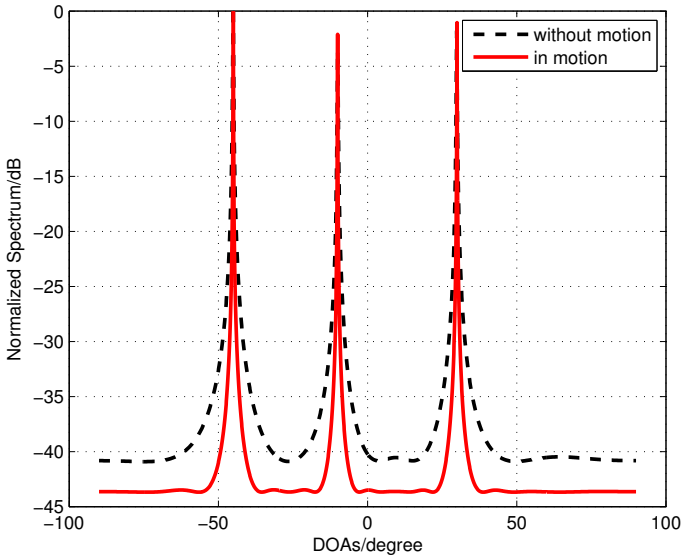

Figure 5.6. Estimation of arriving angles for static co-prime array and moving co-prime array. .

Furthermore, we also show the simulation with the same number of sensors (8 physical sensors) in uniform linear array in Figure 5.7. Seven sources are located at $\pi/180\times$ [-40 -30 -20 -10 10 20 30] with $SNR = 0$ as well. It's clearly to see that

if the number of sources is close to the number of sensors, ULA fails to detect all the sources while the moving co-prime array can still work successfully. Although we never double the size of one co-prime array, based on the phase correction proposed, the moving array shows a good performance.

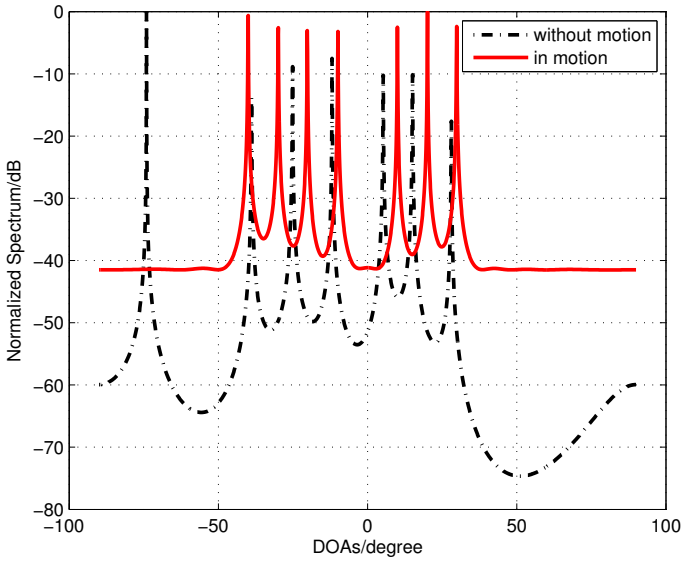

Figure 5.7. Estimation of arriving angles for static ULA and moving co-prime array.
.

To fully understand the properties of multiple steps space-domain sensor synthesis, we still choose the co-prime array with $M = 3$, $N = 5$ and the SNR is 0, the snapshots are 500 as well. In this experiment, 2-step SDS is applied to detect 14 sources in the field which are $\pi/180\times$ [-70 -60 -50 -40 -30 -20 -10 0 10 20 30 40 50 60] and the result is plotted in Figure 5.8. A 2-step SDS co-prime array equals to a $3 \times 5 + 1 + 10 = 26$ virtual sensors linear array. Observe Figure 5.8, although we estimate the phase shift twice, the synthetic data can successfully find all the arriving angles comparing with the 1-step SDS. Another advantage of multiple steps SDS is

that it can be used to find a much larger number of sources even with few physical sensors. In addition, the complexity of estimation process will not increase much in multiple steps SDS.

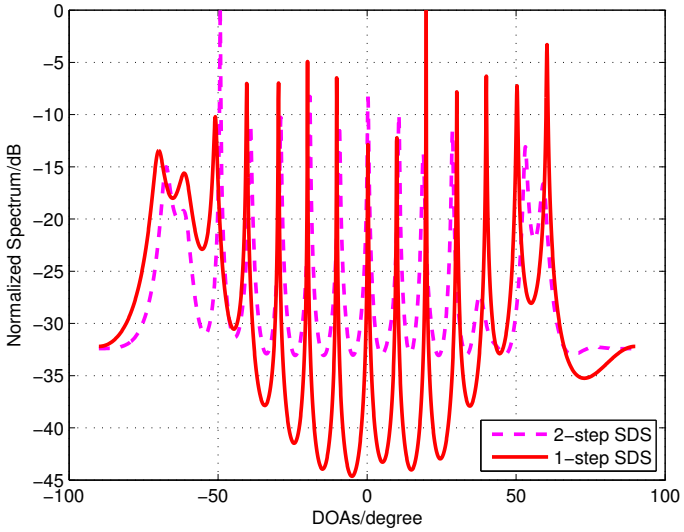

Figure 5.8. 1-step SDS algorithm and 2-step SDS algorithm. .

5.6 Conclusion

We have studied the co-prime array in motion and proposed an algorithm – SDS method. In order to accurately estimate the phase shift, a gradient descent algorithm is also applied in this work. In the lemmas, it proves that both 1-step SDS and multiple step SDS can formed a longer virtual array without holes. We also demonstrate that even the SNR is not high, this structure can still successfully find all the sources. If the number of sources is greater than the number of sensors, the array in motion performs better than the static array. This is due to the virtual sensors from the difference co-array. The simulation results indicate that an array in

motion has a larger dynamic range than the static array and performs better than the uniform linear array. There would be still some more aspects for further exploiting, such as the mobile array in multiple dimensions, the underwater target recognition based on sparse array and implementation on correlated signals.

CHAPTER 6

Evaluating Spatial Resolution and Channel Capacity of Sparse Cylindrical Arrays for Massive MIMO

6.1 Introduction

In recent studies, massive MIMO has become a hot topic in communication area. The reason is that this new technology would be possibly widely applied in the fifth generation (5G) wireless systems. Massive MIMO has a lot of advantages comparing with the 4G LTE [82]-[85], such as it could increase the capacity about 10 times or more and meanwhile improve the radiated energy-efficiency in the order of 100 times [86][87]. Another feature of massive MIMO is that latency reduced significantly compared to LTE. However, the challenges and price paid for massive MIMO are also inevitable, for example, the high complexity of the system and energy efficiency [88]-[90].

Massive MIMO is considered as a major 5G technology, and some experiments of massive MIMO have been measured in [91]-[95]. In addition, the study of antenna deployment in massive MIMO also attracts lots of interest. An overview of massive MIMO and the challenge of making a great number of antennas working together is introduced in [85]. The authors in [96] analyzed whether all antennas contribute equally in real-time massive MIMO environments. In [97], sparse massive MIMO channels are studied. Among those studies, few are about the sparse antenna array deployments. In [17][16], the authors proposed two sparse linear arrays, co-prime linear array (CLA) and nested linear array (NLA), which achieved large degrees of freedom. Moreover, in [98][99], the authors implemented irregular antenna arrays and

sparse cylindrical antenna array respectively. In massive MIMO scenario, because the base station (BS) usually contains hundreds of antennas, if the use of real antennas could be decreased while the capacity remains the same, it would save the space and cost to build the massive MIMO base stations.

Some possible antenna configurations of massive MIMO are the uniform linear array (ULA), uniform rectangular array (URA), uniform circular array and uniform cylindrical array (UCA). In this paper, we focus on the cylindrical array, which is one type of conformal arrays. The advantages of conformal array is that conforming the array to the surface not only saves the space, but also makes the elements less visually intrusive by integrating it into existing objects. A cylindrical array contains of elements in three directions and this provides wide cover in both the azimuth plane ϕ and the elevation plane θ. In massive MIMO scenario, the analysis of spatial resolution of 2D antenna arrays is presented in [100]. Besides, beamforming and DoA estimation in massive MIMO has also attracted lots of interest [101]-[104]. In [105], the authors derived the beam pattern of UCA, which is the product of ULA and uniform circular array. The beam pattern can also be applied to measure the spatial resolution of the cylindrical array.

Firstly, we provide a brief overview of the two sparse linear arrays CCA and NCA respectively. Usually for a ULA, in order to avoid spatial aliasing, the distance of the array elements must not be greater than half a wavelength. But in sparse arrays, since some elements have been removed, the space between some elements does not satisfy the requirement. This element reduction does not necessarily compromise the resolution of sparse array. On the contrast, some good designed sparse arrays could achieve better performance than ULAs, like the minimum redundancy array (MRA) proposed by Moffet in [15], nested linear array (NLA) and co-prime linear array (CLA) proposed by P.P. and Piya in [17][16]. After that, we come up with the

structure of sparse circular array, co-prime cylindrical array (CCA), nested cylindrical array (NCA) and sparse nested cylindrical array (SNCA).

One big difference between conformal arrays and traditional arrays is that the beam pattern can not be obtained by the product of array factor and element pattern. However, since the cylindrical array consists of a series of identical circular arrays, the whole array can be seen as a linear array whose elements are these identical circular arrays. As a result, CCA could be constructed by CLAs and uniform circular arrays. In a similar way, NCA could be constructed by NLAs and uniform circular arrays. Adhikari et al in [106] has analyzed beamforming with co-prime linear arrays and in this work, it's extended to CCA and NCA. Based on the beamforming analysis, we could evaluate the spatial resolution among CCA, NCA and SNCA, and also compare it with the corresponding UCA.

The main contribution of this paper is to extend co-prime linear array and nested linear array to cylindrical arrays. As to prove the advantages of the proposed sparse cylindrical arrays, the new beam patterns of the CCA and NCA are presented. Furthermore, when applied these sparse cylindrical antenna arrays at the BS, the uplink channel capacity could be improved obviously.

The rest of Chapter 6 is outlined as follows. In Section 6.2, we discuss about the co-prime linear array, nested linear array, proposed circular array and three different sparse cylindrical arrays. Then the massive MIMO system model of multiple users is introduced in Section 6.3. After that, in Section 6.4, beamforming analysis of CCA and NCA are provided and in Section 6.5, the spatial resolution performance of UCA, CCA and NCA is compared and the uplink channel spectral efficiency of different cylindrical arrays is provided as well. Finally, concluding remarks are given in Section 6.6.

6.2 Sparse Structure of Linear Array, Circular Array and Cylindrical Array

In this section, firstly two kinds of sparse linear arrays are provided, then we propose the structures of sparse circular array and three different sparse cylindrical arrays. For convenience, the elements used to calculate the difference co-array are referred as physical (or real) antennas and the elements in the difference co-array are called virtual antennas. In fact, the virtual antennas are not existed in the antenna arrays, however, after calculating the difference co-array, the positions of those virtual elements can be obtained.

6.2.1 Sparse Linear Arrays

Co-prime linear array and nested linear array are two kinds of sparse linear arrays, which are proposed in [17][16]. Co-prime linear array interleaves two uniform subarrays which are sampled by two prime integers C_1, C_2, and the locations of the elements are in set $\mathbf{K} = \{\mathbf{K}_1, \mathbf{K}_2\}$, where

$$\begin{aligned} \mathbf{K}_1 &= \{0, C_2\lambda/2, 2C_2\lambda/2, \ldots, (C_1-1)C_2\lambda/2\} \\ \mathbf{K}_2 &= \{0, C_1\lambda/2, 2C_1\lambda/2, \ldots, (C_2-1)C_1\lambda/2\} \end{aligned} \tag{6.1}$$

and λ is the wavelength.

The difference co-array of this pair of ULA has positions

$$z_{C_2p_1-C_1p_2} = C_2p_1 - C_1p_2, 0 \le p_1 \le C_1 - 1,\ 0 \le p_2 \le C_2 - 1 \tag{6.2}$$

Nested linear array is a little different from co-prime linear array, where the elements are placed with two-level density, and level 1 has N_1 elements, level 2 has N_2 elements,

$$\begin{aligned} &1 \le l \le N_1 \\ &(N_1+1)m, \quad 1 \le m \le N_2 \end{aligned} \tag{6.3}$$

The difference co-array of the nested linear array is calculated by

$$z_{(N_1+1)m-l} = (N_1+1)m - l, 1 \leq m \leq N_2,\ 1 \leq l \leq N_1 \tag{6.4}$$

In Figure 6.1(a), it plots an example of co-prime linear array with co-prime integers $(4, 5)$, where the physical antennas are located at $[0, 4, 5, 8, 10, 12, 15, 16]$ and the virtual antenna array calculated by (6.2) equals to $[0, 1, 2, 3, 4, 5, 6, 7, 8, \times, 10, 11, 12, \times, \times, 15, 16]$. $\times$ denotes the holes in the difference co-array and a direct method to solve this problem is to double the length of one uniform subarray.

In Figure 6.1(b), it shows an example of nested linear array with pair $(5, 4)$ and similarly, the physical antennas are located at $[1, 2, 3, 4, 5, 6, 12, 18, 24]$ and the virtual antenna array calculated by (6.4) equals to $[1, \ldots, 5, \times, 7, \ldots, 11, \times, 13, \ldots, 17, \times, 19, \ldots, 23]$. The holes $\times$ can be filled by the self-difference of the physical antennas at $[6, 12, 18, 24]$.

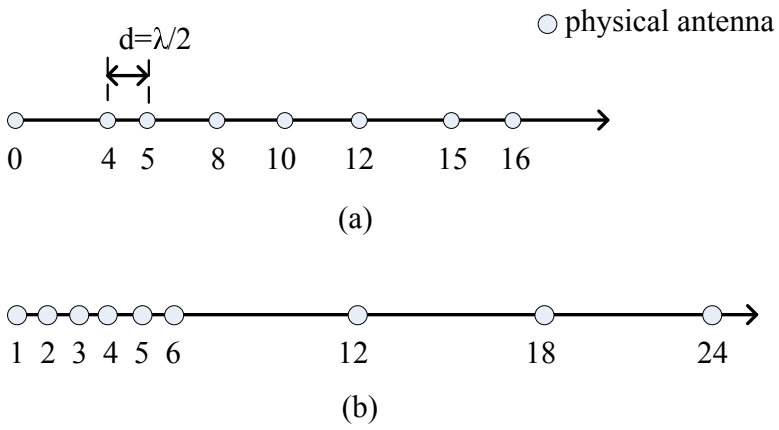

Figure 6.1. Example of co-prime linear array and nested linear array, (a) co-prime pair $(4, 5)$ and the two subarrays are $[0, 4, 8, 12, 16]$, $[0, 5, 10, 15]$, (b) nested pair $(5, 4)$ and the two subarrays are $[1, 2, 3, 4, 5]$, $[6, 12, 18, 24]$.

6.2.2 Sparse Circular Array

To begin with, let's look at a uniform circular array with M_u antennas ($M_u = 2^i, i \geq 2$). The perimeter of the uniform cylindrical array is known as M_u and thus the radius of the circular array $R = M_u/2\pi$. Then the position of the jth antenna $\mathbf{r}_j$ on the circular array equals to

$$(x_j, y_j) = (R - Rcos(\frac{2\pi}{M_u}j), Rsin(\frac{2\pi}{M_u}j)), 1 \leq j \leq M_u/2 \tag{6.5}$$

Besides, the locations of the $\frac{M_u}{2} + 1$th antenna $\mathbf{r}_{\frac{M_u}{2}+1}$ and $\frac{M_u}{2} + j$th antenna $\mathbf{r}_{\frac{M_u}{2}+j}$ are

$$(x_{\frac{M_u}{2}+1}, y_{\frac{M_u}{2}+1}) = (2R, 0) \tag{6.6}$$

and

$$\begin{aligned} &(x_{\frac{M_u}{2}+j}, y_{\frac{M_u}{2}+j}) = \\ &(R + Rcos(\frac{2\pi}{M_u}j), -Rsin(\frac{2\pi}{M_u}j)), \end{aligned} \tag{6.7}$$

It's straightforward to see that

$$(x_{\frac{M_u}{2}+j}, y_{\frac{M_u}{2}+j}) = (x_{\frac{M_u}{2}+1}, y_{\frac{M_u}{2}+1}) - (x_j, y_j) \tag{6.8}$$

Consequently, we can define the difference co-array of sparse circular array as

$$\begin{aligned} &(x_{\frac{M_u}{2}+j}, y_{\frac{M_u}{2}+j}) = (x_{\frac{M_u}{2}+1}, y_{\frac{M_u}{2}+1}) - (x_j, y_j), \\ &1 \leq j \leq M_u/2 \end{aligned} \tag{6.9}$$

In Figure 6.2, it shows an example of the sparse circular array where $M_u = 8$, which indicates that we could build an 8-element uniform circular array only with 5 real antennas.

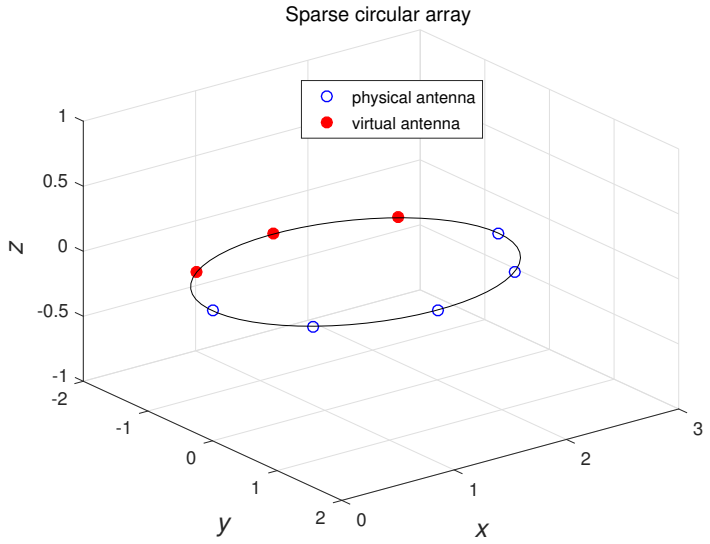

Figure 6.2. Example of sparse circular array with $M_u = 8$. The virtual antennas are shown in red dots and the physical antennas are in blue dots. All the virtual antennas can be calculated by the difference co-array of the physical antennas via (9) .

6.2.3 Different Structures of Sparse Cylindrical Arrays

Based on the sparse linear array and sparse circular array, we propose three different structures of sparse cylindrical arrays. Firstly, the geometries of co-prime cylindrical array (CCA) and nested cylindrical array (NCA) are illustrated in Figure 6.3 and Figure 6.4 respectively. In the z-axis direction, the elements are placed as co-prime linear array or nested linear array and for each circle, it is still a uniform circular array.

Since co-prime linear array starts from position 0 while nested linear array starts from position 1, so we modify nested linear array by adding one more element at position 0. As a result, the difference co-array of CCA could be written as

$$\begin{aligned}&(x_q, y_q, z_{C_2p_1 - C_1p_2}) = \\ &(x_{\frac{M_u}{2}+1}, y_{\frac{M_u}{2}+1}, z_{C_2p_1}) - (x_j, y_j, z_{C_1p_2}),\end{aligned} \tag{6.10}$$

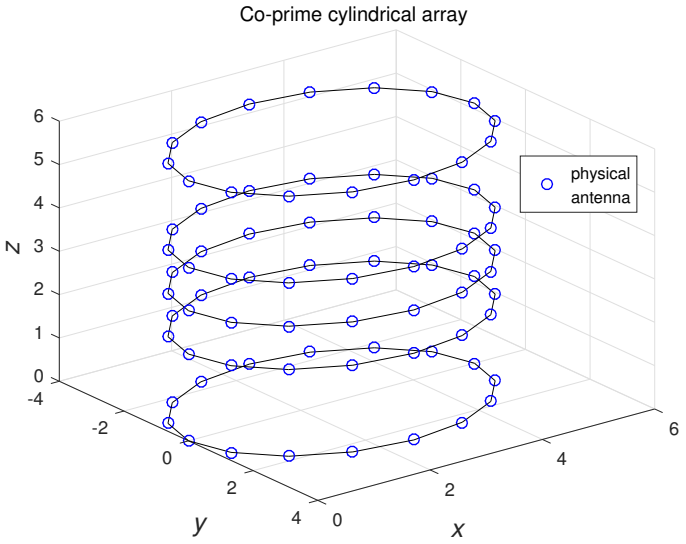

Figure 6.3. Example of co-prime cylindrical array with $M_u = 16$ antennas on each circular array and the vertical antennas are located at $[0, 2, 3, 4, 6]$. In this example, the vertical antennas are placed as co-prime linear array with pair $(2, 3)$.

where $0 \leq p_1 \leq C_1 - 1$, $0 \leq p_2 \leq C_2 - 1$, if $1 \leq j \leq M_u/2$, $q = \frac{M_u}{2} + j$ and if $M_u/2 < j \leq M_u$, $q = j - \frac{M_u}{2}$.

The difference co-array of NCA is

$$\begin{aligned} &(x_q, y_q, z_{(N_1+1)m-l}) = \\ &(x_{\frac{M_u}{2}+1}, y_{\frac{M_u}{2}+1}, z_{(N_1+1)m}) - (x_j, y_j, z_l), \end{aligned} \tag{6.11}$$

where $0 \leq m \leq N_2$, $1 \leq l \leq N_1$, if $1 \leq j \leq M_u/2$, $q = \frac{M_u}{2} + j$ and if $M_u/2 < j \leq M_u$, $q = j - \frac{M_u}{2}$.

Furthermore, if each circle is deployed as a sparse circular array, the vertical linear arrays at $x = 0, y = 0$ and $x = 2R, y = 0$ are placed as nested linear array, this kind of cylindrical array is named sparse nested cylindrical array (SNCA). In a similar way, we could build sparse co-prime cylindrical array, but in this paper we only discuss about SNCA. The difference co-array of SNCA is expressed as

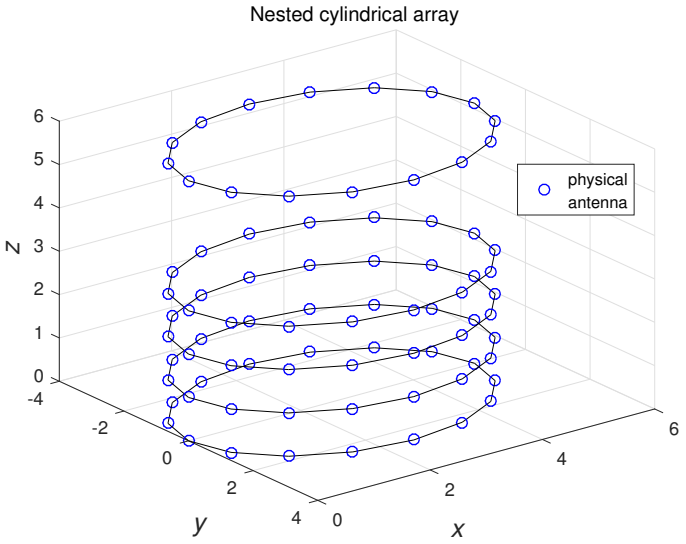

Figure 6.4. Example of nested cylindrical array with $M_u = 16$ antennas on each circular array and the vertical antennas are located at $[0, 1, 2, 3, 6]$. In this example, the vertical antennas are placed as nested linear array with pair $(2, 3)$, but with one more circular array at position 0 .

$$\begin{cases} (x_{\frac{M_u}{2}+j}, y_{\frac{M_u}{2}+j}, 0) \\ = (x_{\frac{M_u}{2}+1}, y_{\frac{M_u}{2}+1}, 0) - (x_j, y_j, 0), 1 \le j \le M_u/2, \\ (x_{\frac{M_u}{2}+j}, y_{\frac{M_u}{2}+j}, z_{(N_1+1)m-l}) \\ = (x_{\frac{M_u}{2}+1}, y_{\frac{M_u}{2}+1}, z_{(N_1+1)m}) - (x_j, y_j, z_l), \\ 1 \le m \le N_2,\ 0 \le l \le N_1,\ 1 \le j \le M_u/2+1 \end{cases} \tag{6.12}$$

and in Figure 6.5, it illustrates an example of SNCA.

For CCA, NCA, SNCA, when the virtual antennas are obtained by the difference co-array (6.10), (6.11) and (6.12) separately, we could add those virtual elements to the physical antennas and then plot the corresponding cylindrical array in Figure 6.6. It's straightforward to see that Figure 6.3 to Figure 6.5 have the same corresponding cylindrical array, which is a uniform cylindrical array with 16×7 antennas.

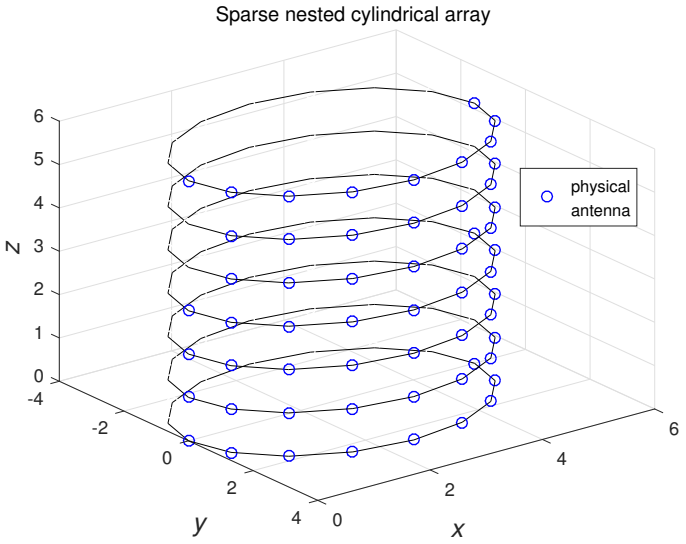

Figure 6.5. Example of sparse nested cylindrical array with $M_u = 16$ antennas on the corresponding uniform circular array. The vertical arrays when $x = 0, y = 0$ and $x = 2R, y = 0$ are located at $[0, 1, 2, 3, 6]$, with nested pair $(2, 3)$. In this example, the virtual antennas on each circular array can be calculated via (12) .

6.3 Massive MIMO System Model

6.3.1 MU-MIMO System Model

In Figure 6.7, a typical scenario of uplink transmission in massive MIMO is shown. A cylindrical array with $N_r (N_r = M_u \times N_u)$ physically small and non-directive antennas is located at the BS, which receives the signals from K single-antenna users. For massive MIMO, N_r is usually very large and greater than K. Let's consider the uplink transmission, then the $N_r \times 1$ vector received at the BS is

$$\mathbf{y} = \sqrt{\rho_u}\mathbf{G}\mathbf{x} + \mathbf{n} \tag{6.13}$$

where $\sqrt{\rho_u}$ is the average transmit power, $\mathbf{x} \in \mathbb{C}^{K\times 1}$ is the transmit vector by the K users, $\mathbf{G} \in \mathbb{C}^{N_r \times K}$ is the channel matrix between the BS and the K users, i.e.,

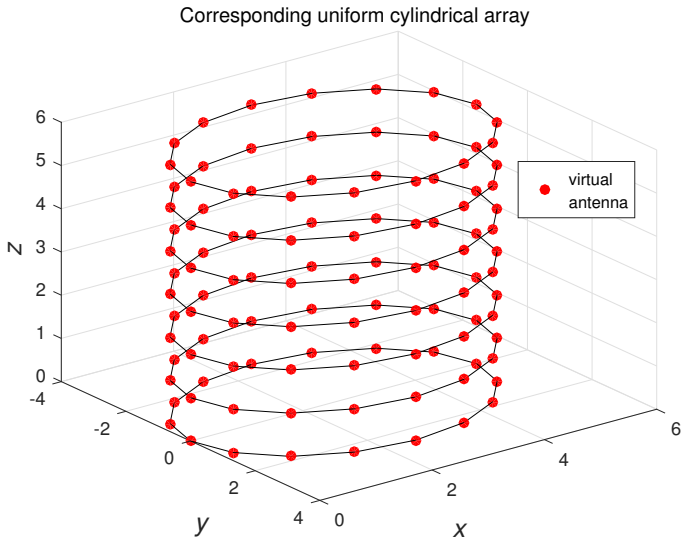

Figure 6.6. Example of the corresponding uniform cylindrical array of Figure 6.3 to Figure 6.5. In this example, the UCA has 8 circular arrays and each circular array has 16 antennas, so the total number of the UCA is $N_r = 16 \times 8$.

$g_{nk} \triangleq [\mathbf{G}]_{nk}$ represents the channel coefficient between the nth antenna from the BS and the kth user and $\mathbf{n} \in \mathbb{C}^{N_r \times 1}$ is the additive white Gaussian noise.

In wireless communication, channel often experiences fading caused by multi-path or shadowing. If we assume the channel matrix $\mathbf{G}$ models log-normal shadow fading, then we have

$$g_{nk} = h_{nk}\sqrt{\beta_k}, \quad n = 1, 2, \cdots, N_r \tag{6.14}$$

where h_{nk} is the fast fading coefficient from the kth user to the nth antenna of the BS and $\sqrt{\beta_k}$ represents the geometric attenuation due to shadow fading which is assumed independent over n and known a priori. So

$$\mathbf{G} = \mathbf{H}\mathbf{D}^{1/2} \tag{6.15}$$

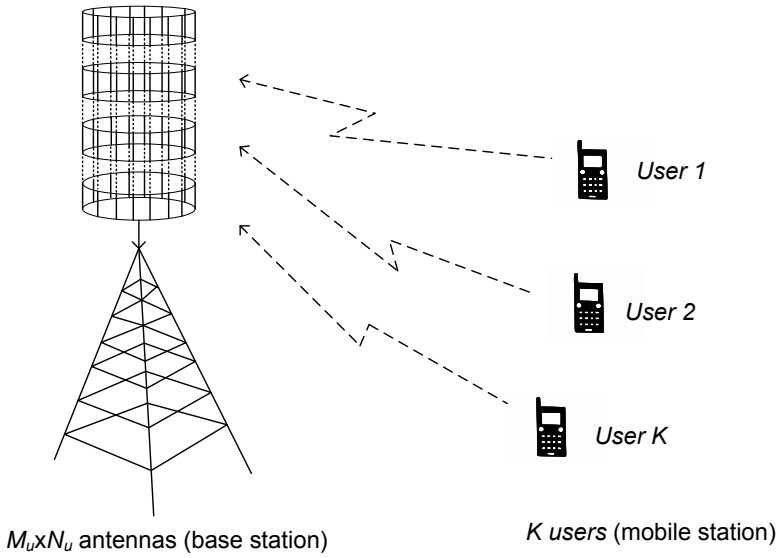

Figure 6.7. Uplink operation of a massive MIMO system. There're K users in a single cell and $M_u \times N_u$ antennas on the BS .

where $\mathbf{H} \in \mathbb{C}^{N_r \times K}$ denotes the fast fading matrix, i.e., $[\mathbf{H}]_{nk} = h_{nk}$ and $\mathbf{D}^{1/2} \in \mathbb{C}^{K \times K}$ is a diagonal matrix with $[\mathbf{D}]_{kk} = \beta_k$.

Supposing (θ_k, ϕ_k) is the AoD from the kth user to the BS, then

$$\begin{aligned} h_{nk} &= \alpha_{nk} e^{j2\pi(x_n sin\theta_k cos\phi_k + y_n sin\theta_k sin\phi_k + z_n cos\theta_k)/\lambda}, \\ & n = 1, 2, \cdots, N_r \end{aligned} \tag{6.16}$$

where α_{nk} is the path gain.

At the BS, the manifold matrix of the cylindrical array is denoted by $\mathbf{A} \in \mathbb{C}^{N_r \times K}$, where

$$\mathbf{A} = [\mathbf{e}_{r,1}, \mathbf{e}_{r,2}, \ldots, \mathbf{e}_{r,K}] \tag{6.17}$$

and

$$\mathbf{e}_{r,k} = \begin{bmatrix} e^{j\frac{2\pi}{\lambda}(x_1 sin\theta_k cos\phi_k + y_1 sin\theta_k sin\phi_k + z_1 cos\theta_k)} \\ e^{j\frac{2\pi}{\lambda}(x_2 sin\theta_k cos\phi_k + y_2 sin\theta_k sin\phi_k + z_2 cos\theta_k)} \\ \vdots \\ e^{j\frac{2\pi}{\lambda}(x_{N_r} sin\theta_k cos\phi_k + y_{N_r} sin\theta_k sin\phi_k + z_{N_r} cos\theta_k)} \end{bmatrix} \tag{6.18}$$

If α_{nk} is set to be 1, then

$$\mathbf{H} = \mathbf{A} \tag{6.19}$$

As a consequence, by substituting (6.15) and (6.19) into (6.13), we have

$$\mathbf{y} = \sqrt{\rho_u}\mathbf{A}\mathbf{D}^{1/2}\mathbf{x} + \mathbf{n} \tag{6.20}$$

and $\mathbf{G}$ is rewritten as

$$\mathbf{G} = \mathbf{A}\mathbf{D}^{1/2} \tag{6.21}$$

When maximum-ratio combining (MRC) is applied at the BS, from [88], we could obtain the ergodic achievable uplink rate of the kth user as

$$R_k^{mrc} = \mathbb{E}\left[log_2\left(1 + \frac{\rho_u \left\|\mathbf{g}_k\right\|^4}{\rho_u \sum_{i=1, i\neq k}^{K} \left|\mathbf{g}_k^H \mathbf{g}_i\right|^2} + \left\|\mathbf{g}_k\right\|^2\right)\right] \tag{6.22}$$

6.3.2 System Model Based on Difference Co-array

From Section A, we know that the received signal is

$$\mathbf{y} = \sqrt{\rho_u}\mathbf{A}\mathbf{D}^{1/2}\mathbf{x} + \mathbf{n} \tag{6.23}$$

and both the signal source and the noise are assumed to be temporally uncorrelated, so the source autocorrelation matrix $\mathbf{R_{xx}}$ is a diagonal matrix. The autocorrelation of the received signal is

$$
\begin{aligned}
\mathbf{R_{yy}} &= E[\mathbf{y}\mathbf{y}^H] \\
&= \rho_u \mathbf{A}\mathbf{R_{xx}}\mathbf{D}\mathbf{A}^H + \sigma_n^2\mathbf{I} \\
&= \rho_u \mathbf{A} \begin{pmatrix} \beta_1\sigma_1^2 & & & \\ & \beta_2\sigma_2^2 & & \\ & & \ddots & \\ & & & \beta_K\sigma_K^2 \end{pmatrix} \mathbf{A}^H + \sigma_n^2\mathbf{I}
\end{aligned} \tag{6.24}
$$

Following [16], the vector mapping operation could be applied on $\mathbf{R_{yy}}$ as

$$
\begin{aligned}
\mathbf{s} &= vec(\mathbf{R_{yy}}) \\
&= vec\left[\sum_{i=1}^{K} \rho_u\beta_i\sigma_i^2(\mathbf{e}(\theta_i,\phi_i)\mathbf{e}^H(\theta_i,\phi_i))\right] + \sigma_n^2 \overrightarrow{\mathbf{1}}_n \\
&= (\mathbf{A}^* \odot \mathbf{A})\,\mathbf{p} + \sigma_n^2 \overrightarrow{\mathbf{1}}_n
\end{aligned} \tag{6.25}
$$

where $\odot$ is the Khatri-Rao product, $\mathbf{p} = [\rho_u\beta_1\sigma_1^2, \rho_u\beta_2\sigma_2^2, \ldots, \rho_u\beta_K\sigma_K^2]^T$ and $\overrightarrow{\mathbf{1}}_n$ is the identity matrix. Comparing (6.23) and (6.25), the manifold matrix in (6.25) could be treated as $(\mathbf{A}^* \odot \mathbf{A})$, the source signal $\mathbf{x}$ now becomes $\mathbf{p}$ and the noise becomes $\sigma_n^2 \overrightarrow{\mathbf{1}}_n$. Because $(\mathbf{A}^* \odot \mathbf{A})$ calculates the difference co-array of the original array, thus $\mathbf{s}$ behaves like the received signal with a longer array where the positions of antennas are given by the distinct values whose sensor locations are given by the distinct values in the set $\{\mathbf{r}_j - \mathbf{r}_q, 1 \leq j, q \leq N_r\}$ where $\mathbf{r}_j$ denotes the position of the jth sensor of the original array and $\mathbf{r}_q$ denotes the position of the qth sensor of the original array.

6.4 Beamforming Analysis of Co-prime Cylindrical Array and Nested Cylindrical Array

For a uniform cylindrical array as shown in Figure 6.6, assuming all the elements are isotropic and are placed on the surface of a staggered grid. If there are N_u circular

arrays and M_u elements in each circular array, the far-field beam pattern in the generic direction (θ, ϕ) of the cylindrical array could be represented as [66]

$$B(\theta,\phi) = \sum_{n=0}^{N_u-1} \sum_{m=1}^{M_u} w_{nm}^* e^{-j\mathbf{k}^T \mathbf{r}_{nm}} \tag{6.26}$$

where w_{nm} is the weight value of the mth element on the nth circular array, $\mathbf{k}$ is the wavenumber defined in (6.27) and $\mathbf{r}_{nm}$ is the location of the mth element on the nth circular array.

$$\mathbf{k} = -\frac{2\pi}{\lambda} \begin{bmatrix} sin\theta\ cos\phi \\ sin\theta\ sin\phi \\ cos\theta \end{bmatrix} \tag{6.27}$$

where λ is the wavelength.

Substituting $\mathbf{k}$ into (6.26), it could be rewritten as

$$B(\theta,\phi) = \sum_{n=0}^{N_u-1} \sum_{m=1}^{M_u} w_{nm}^* e^{jk_0[Rsin\theta cos(\phi-\phi_m)+z_n cos\theta]} \tag{6.28}$$

here $k_0 = |\mathbf{k}| = 2\pi/\lambda$, R is the radius of the circular array and $\phi_m = 2\pi m/M_u$.

If we further expand (6.28), it's easy to see that the second term in the braces is the beam pattern of the nth circular array as following

$$B(\theta,\phi) = \sum_{n=0}^{N_u-1} e^{jk_0 z_n cos\theta} \left\{ \sum_{m=1}^{M_u} w_{nm}^* e^{jk_0 Rsin\theta cos(\phi-\phi_m)} \right\} \tag{6.29}$$

Replace the second term with $B_{cir,n}(\theta,\phi)$, then (6.29) is simplified as

$$B(\theta,\phi) = \sum_{n=0}^{N_u-1} e^{jk_0 z_n cos\theta} B_{cir,n}(\theta,\phi) \tag{6.30}$$

Assuming the array in the z-direction to be elements of a linear array and each column has uniform weighting, which means that w^*_{nm} can be separated as the product of the two array factors as

$$w^*_{nm} = w^*_n w^*_m \tag{6.31}$$

(6.30) could reduce to

$$\begin{aligned} B(\theta,\phi) &= \sum_{n=0}^{N_u-1} w^*_n e^{jk_0 z_n cos\theta} B_{cir}(\theta,\phi) \\ &= B_{lin}(\theta,\phi) B_{cir}(\theta,\phi) \end{aligned} \tag{6.32}$$

For the B_{lin} part, if it's a uniform linear array with length N_u, then the beam pattern is

$$\begin{aligned} B_{lin} &= \frac{1}{N_u} \sum_{n=0}^{N_u-1} e^{jn\pi u} \\ &= \frac{1}{N_u} \cdot \frac{1-e^{jN_u\pi u}}{1-e^{j\pi u}} \end{aligned} \tag{6.33}$$

where $u = cos(\theta)$.

When the elements in z-direction are placed as co-prime linear array with pair (C_1, C_2), the beam patterns of the two sub-arrays are

$$\begin{aligned} B_{lin,C_1} &= \frac{1}{C_1} \sum_{c=0}^{C_1-1} e^{jcC_2\pi u} \\ &= \frac{1}{C_1} \left(\frac{1-e^{jC_1C_2\pi u}}{1-e^{jC_2\pi u}} \right) \end{aligned} \tag{6.34}$$

$$\begin{aligned} B_{lin,C_2} &= \frac{1}{C_2} \sum_{c=0}^{C_2-1} e^{jcC_1\pi u} \\ &= \frac{1}{C_2} \left(\frac{1-e^{jC_1C_2\pi u}}{1-e^{jC_1\pi u}} \right) \end{aligned} \tag{6.35}$$

Through the beam patterns of the two subarrays, we can calculate the beam pattern of the (C_1, C_2) co-prime array as

$$
\begin{aligned}
B_{lin,C_1,C_2} &= B_{lin,C_1} \times B_{lin,C_2} \\
&= \frac{1}{C_1 C_2} \cdot \frac{(1 - e^{jC_1C_2\pi u})^2}{(1 - e^{jC_1\pi u})(1 - e^{jC_2\pi u})}
\end{aligned} \tag{6.36}
$$

B_{lin,C_1,C_2} has been derived in [107], but the authors did not provide the beam pattern of nested array. For the nested array with pair (N_1, N_2), we also apply uniform weighting and the beam pattern of two sub-arrays are

$$
\begin{aligned}
B_{lin,N_1} &= \frac{1}{N_1 + 1} \sum_{n=0}^{N_1} e^{jn\pi u} \\
&= \frac{1}{N_1 + 1} \cdot \frac{1 - e^{j(N_1+1)\pi u}}{1 - e^{j\pi u}}
\end{aligned} \tag{6.37}
$$

$$
\begin{aligned}
B_{lin,N_2} &= \frac{1}{N_2} \sum_{n=1}^{N_2} e^{jn(N_1+1)\pi u} \\
&= \frac{e^{j(N_1+1)\pi u}}{N_2} \cdot \frac{1 - e^{j(N_1+1)N_2\pi u}}{1 - e^{j(N_1+1)\pi u}}
\end{aligned} \tag{6.38}
$$

To be noticed is that, for the nested linear array, we add an element at position 0, i.e., the nested linear array with $N_1 = 5, N_2 = 4$ is located at $[0, 1, 2, 3, 4, 5, 6, 12, 18, 24]$ and the two subarrays are located at $[0, 1, 2, 3, 4, 5]$, $[6, 12, 18, 24]$ respectively.

Similarly, we can calculate the beam pattern of the (N_1, N_2) nested array as

$$
\begin{aligned}
B_{lin,N_1,N_2} &= B_{lin,N_1} \times B_{lin,N_2} \\
&= \frac{e^{j(N_1+1)\pi u}}{(N_1 + 1)N_2} \cdot \frac{1 - e^{j(N_1+1)N_2\pi u}}{1 - e^{j\pi u}}
\end{aligned} \tag{6.39}
$$

The absolute value of (6.39) is

$$
|B_{lin,N_1,N_2}| = \left| \frac{1}{(N_1 + 1)N_2} \cdot \frac{1 - e^{j(N_1+1)N_2\pi u}}{1 - e^{j\pi u}} \right| \tag{6.40}
$$

Comparing to (6.33), it's straightforward to see that (6.33) equals to the absolute value (6.40) if $N = (N_1 + 1)N_2$ sensors. As a matter of fact, nested linear array could achieve exactly the same beam pattern of a ULA. This property helps us to

further analyze the performance improvement of the beam pattern when comparing NCA, CCA and UCA.

The 3-dB beamwidth is an important parameter in measuring the array geometry because it's related with the array's ability to distinguish different signals arriving from different angles. A narrow 3-dB beamwidth means a high resolution of the array. We know that for a ULA, the width of the main beam is obtained by solving

$$\frac{\pi N_u d}{\lambda} u = 1.4 \tag{6.41}$$

If the co-prime linear array needs to achieve the same beamwidth, (6.41) is rewritten as

$$(\frac{\pi C_1 C_2 u}{2})^2 = 1.4 \tag{6.42}$$

and for nested linear array, it becomes

$$\frac{\pi(N_1+1)N_2 u}{2} = 1.4 \tag{6.43}$$

Let (6.42) equals to (6.43), the relationship between co-prime pair and nested pair is obtained as

$$\frac{C_1 C_2}{(N_1+1)N_2} \approx \frac{1}{\sqrt{1.4}} \tag{6.44}$$

By assuming C_1 and C_2 are known parameters, the goal is to find the value of N_1 and N_2. When $(N_1+1)N_2$ is minimized in the nested array, the difference between N_1 and N_2 should be 1. For example, if the co-prime pair is $(4, 5)$, calculating through (6.44), we can get $(N_1+1)N_2 \approx 24$. As a consequence, the nested pair should be $(5, 4)$.

In order to verify our analysis, the beam pattern of a co-prime linear array (with pair $(4, 5)$) and a nested linear array (with pair $(5, 4)$) is plotted in Figure 6.8, where the CLA is located at $[0, 4, 5, 8, 10, 12, 15, 16]$ with pair $(4, 5)$, the NLA is located at $[0, 1, 2, 3, 4, 5, 6, 12, 18, 24]$ with pair $(5, 4)$ and the ULA is located at $[0, 1, 2, \ldots, 23]$. We can see that their 3-dB beamwidth is exactly the same. Figure 6.8 also proves that the beam pattern of a nested linear array with pair (N_1, N_2) equals to a uniform linear array with $(N_1 + 1)N_2$ elements.

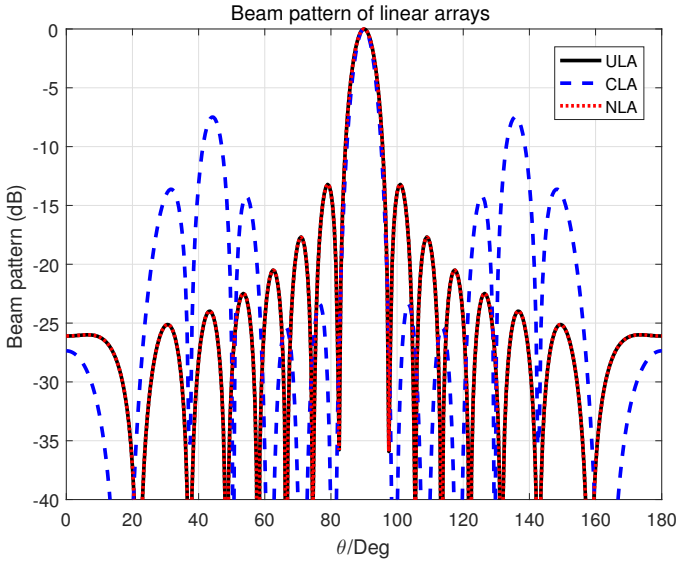

Figure 6.8. Example of beam patterns of ULA in black line, CLA in blue dashed line and NLA in red dashed line, In this example, all the three linear arrays have the same 3-dB beamwidth. Besides, since the length of ULA is $(N_1 + 1)N_2 = (5 + 1) \times 4$, the beam pattern of ULA is exactly the same with the beam pattern of CLA of pair (N_1, N_2) .

6.5 Simulation Results

In this section, we firstly simulate the scenario of two sources in the range. The spatial resolution of CCA and NCA is shown and compared with the UCA of

the same aperture on z-axis. Then the unplink spectral efficiency of CCA, NCA and SNCA is analyzed when those sparse cylindrical arrays are placed at the BS.

6.5.1 Spatial Resolution of CCA and NCA

Assuming the deployment of CCA and NCA is as shown in Figure 6.3 and Figure 6.4, where there're 16 antennas uniformly spaced on every circular array, since the azimuth resolution is determined by the circular array, if CCA and NCA have the same deployment of circular array, their beam pattern of azimuth angle should have identical performance as well. Supposing there're two sources coming from direction $\phi_1 = 80°$ and $\phi_2 = 100°$, then the 1D beam pattern is illustrated in Figure 6.9.

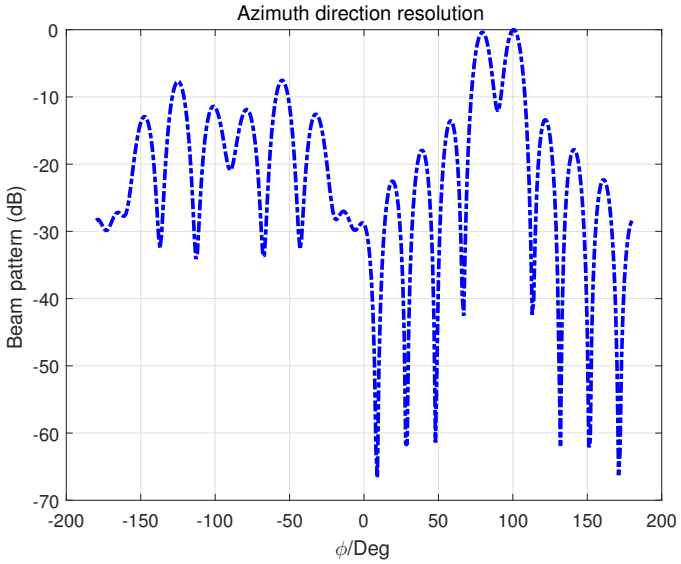

Figure 6.9. Example of azimuth direction resolution of CCA and NCA. In this example, the CCA and NCA are shown as Fig. 3 and Fig. 4. Besides, there're two sources coming from $\phi_1 = 80°$ and $\phi_2 = 100°$. Since the azimuth direction resolution is mainly decided by the circular arrays on the cylindrical array, when CCA and NCA have the same circular arrays, the azimuth beam pattern is identical .

Next, let's consider the resolution of elevation direction of CCA and NCA. If the CCA and NCA are still chosen as Figure 6.3 and Figure 6.4, we plot the 3-dB beamwidth in Figure 6.10. From Figure 6.10 we can see that when the length of vertical linear array is short, the 3-dB beamwidth of CCA and NCA is very wide, which will bring a low resolution of the elevation angle.

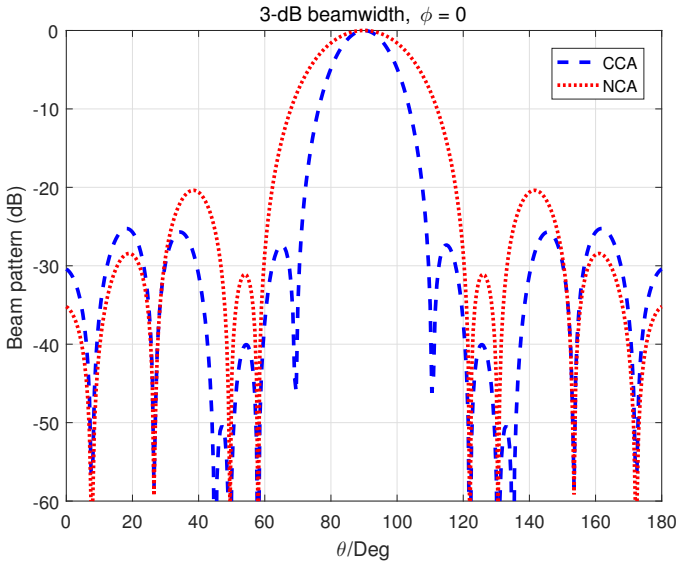

Figure 6.10. Example of 3-dB beamwidth of CCA and NCA. The CCA and NCA are as plotted in Figure 6.3 and Figure 6.4 respectively .

A possible way to increase the resolution of CCA and NCA is to extend the length of the vertical array. Assuming the number of elements on each circular array is also 16, choosing the co-prime pair of CCA as $(5, 6)$, then the positions of the vertical array on the z-axis is $[0, 5, 6, 10, 12, 15, 18, 20, 24, 25]$, and set nested pair of NCA to be $(4, 5)$, which means that the vertical array locates at $[0, 1, 2, 3, 4, 5, 10, 15, 20, 25]$. Apparently the number of physical antennas of CCA and NCA is the same (which equals to $160 = 16 \times 10$). By calculating the difference co-array of CCA and NCA, the corresponding vertical array of UCA should be placed at $[0, 1, 2, \ldots, 25]$ and the

number of antennas is $416 = 16 \times 26$. This indicates that CCA and NCA save about 62% antennas comparing with the corresponding UCA.

Supposing there're two far sources coming from $\theta_1 = 80°$ and $\theta_2 = 100°$, the beam pattern of CCA and NCA is shown in Figure 6.11, where the vertical antennas of CCA are placed at $[0, 5, 6, 10, 12, 15, 18, 20, 24, 25]$, the vertical antennas of NCA are placed at $[0, 1, 2, 3, 4, 5, 10, 15, 20, 25]$ and their corresponding UCA contains vertical antennas located at $[0, 1, 2, \ldots, 25]$.

Similarly, when the two sources are from $\theta_1 = 80°$ and $\theta_2 = 85°$, the beam pattern results are given in Figure 6.12 and the structures of UCA, CCA and NCA are the same as used in Figure 6.11. We also compare the performance with their corresponding UCA. It's straightforward to see that the two far sources are successfully detected by UCA, CCA and NCA, however, CCA and UCA fail to distinguish the two close sources while NCA successfully detects that.

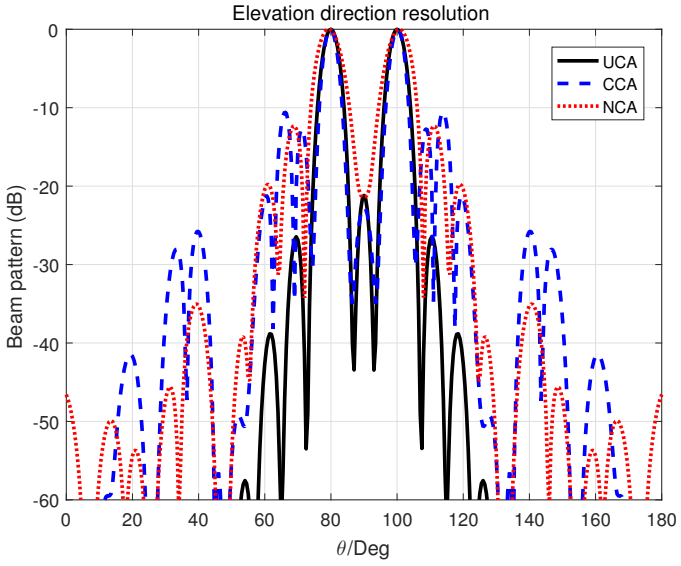

Figure 6.11. Example of elevation direction resolution of UCA, CCA and NCA, assuming there're two sources coming from $\theta_1 = 80°$ and $\theta_2 = 100°$.

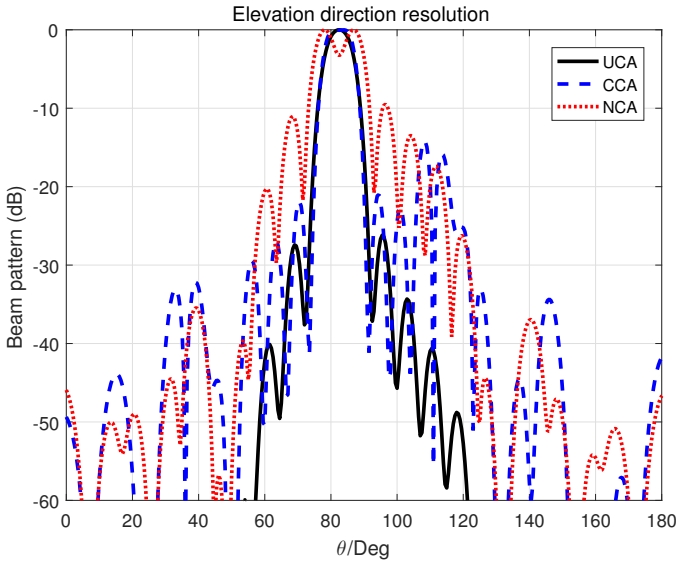

Figure 6.12. Example of elevation direction resolution of UCA, CCA and NCA, assuming there're two sources coming from $\theta_1 = 80°$ and $\theta_2 = 85°$. In this example, we can see that CCA and UCA fail to distinguish the two close sources while NCA successfully detects that .

6.5.2 MU-MIMO Capacity Analysis

In Section 6.3, it provides the ergodic achievable uplink rate for the kth user, based on R_k^{mrc}, we can define the spectral efficiency of the massive MIMO system as

$$R^{mrc} = \sum_{k=1}^{K} R_k^{mrc} \tag{6.45}$$

With the condition that CCA, NCA and SNCA have the same corresponding UCA, which is constructed by N_r antennas, via (6.25), a new matrix $\mathbf{A}_1$ of size $(N_r) \times K$ from $\mathbf{A}^* \odot \mathbf{A}$ can be obtained. Since there would be some repeated rows after vector mapping, we need to remove all the repeated rows. This is equivalent to removing the corresponding rows in vector $\mathbf{s}$ and finally a new vector of the received signal could be given by

$$\mathbf{y}_1 = \mathbf{A}_1\mathbf{p} + \sigma_n^2 \vec{\mathbf{1}}_n \tag{6.46}$$

and the expression of $\mathbf{G}$ is rewritten as

$$\widetilde{\mathbf{G}} = \mathbf{A}_1 \tag{6.47}$$

Consequently, the sum-rate capacity of the uplink is calculated as

$$\begin{aligned} \widetilde{R}^{mrc} &= \sum_{k=1}^{K} \widetilde{R}_k^{mrc} \\ &= \mathbb{E}\left[log_2\left(1 + \frac{\|\widetilde{\mathbf{g}}_k\|^4}{\sum_{i=1,i\neq k}^{K} \left|\widetilde{\mathbf{g}}_k^H \widetilde{\mathbf{g}}_i\right|^2} + \|\widetilde{\mathbf{g}}_k\|^2 \right) \right] \end{aligned} \tag{6.48}$$

In order to compare the channel capacity among different sparse cylindrical arrays, their number of antennas are given in Table 6.1 and Table 6.2. The first column of Table 6.1 and Table 6.2 means N_r on UCA. For instance, when $M_u = 8$ and $N_r = 48$, it represents a UCA with 6 circular arrays and on each circular array, there're 8 antennas. The columns of CCA, NCA and SNCA are the number of physical antennas plus the number of virtual antennas, where the number of physical antennas are the same as in the UCA, but the virtual antennas are calculated by different difference co-arrays. For example, when $M_u = 16$ and $N_r = 80$, the NCA is built by 5 circular arrays which located at $z = [0, 1, 2, 4]$ and on each circular array, there're 16 antennas. Therefore, this NCA equals to a UCA with 5×16 antennas.

Hence, in Figure 6.13 and Figure 6.14, we plot the spectral efficiency of the UCA, CCA, NCA and SNCA as listed in Table 6.1 and Table 6.2 respectively. Considering there're $K = 10$ users in a cell and the users are located uniformly at random. The radius of the cell is 1000 meters and the SNR is 2 dB. From Figure 6.13 and Figure 6.14, we can conclude that all the three structures of sparse cylindrical arrays perform

Table 6.1. Number of antennas on UCA, CCA, NCA and SNCA when $M_u = 8$

UCA(N_r)	**CCA**	**NCA**	**SNCA**
48	80	80	80
64	112	128	128
80	144	176	160
96	176	224	192
112	208	272	224
128	240	320	256
144	272	368	288
160	304	416	320

better than UCA. Besides, when $M_u = 8$ in Fig. 13, NCA has the highest spectral efficiency among UCA, CCA and SNCA, but when M_u increases to 16, NCA only outperforms CCA and NCA when N_r is larger than around 110. These trends are also reflected in Table 6.1 and Table 6.2.

6.6 Conclusion

Three kinds of sparse cylindrical antenna arrays, CCA, NCA and SNCA are proposed in this paper, which are generated from the co-prime linear array, nested linear array and sparse circular array correspondingly. To the best of our knowledge, this is the first time that co-prime array and nested array are combined with cylindrical array. The detailed analysis of the beam pattern for CCA and NCA is provided. Since beam pattern is related with the ability of resolution, we compared the perfor-

Table 6.2. Number of antennas on UCA, CCA, NCA and SNCA when $M_u = 16$

UCA(N_r)	**CCA**	**NCA**	**SNCA**
48	64	48	80
64	96	80	112
80	128	112	144
96	160	160	176
112	192	208	208
128	224	256	240
144	256	304	272
160	288	352	304

mance of beam pattern among UCA and CCA, NCA. UCA and CCA can distinguish sources which are far away from each other, but when two close sources come from the range, only NCA can recognize it. Moreover, we also simulate the uplink channel capacity in massive MIMO scenario and prove that all the three sparse cylindrical arrays could increase the channel capacity with fewer physical antennas. In the future study, we will focus on some other properties of the sparse cylindrical arrays, such as applying different weighting functions and the measurement of these sparse antenna arrays as well.

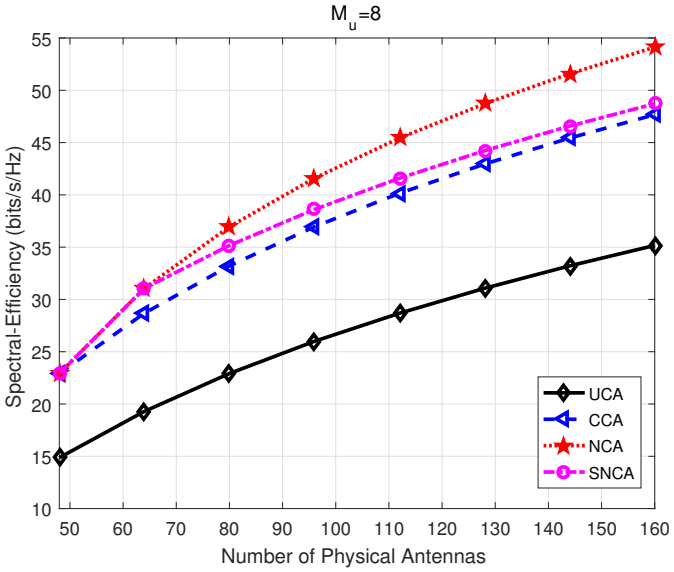

Figure 6.13. Spectral efficiency versus the number of physical BS antennas N_r when MRC is applied at the receiver. In this example, $K = 10$ and the numbers of antennas of UCA, CCA, NCA, SNCA are listed in Table 6.1. Averagely, the three structures of sparse cylindrical array, which are CCA, NCA and SNCA can double the number of antennas of the UCA .

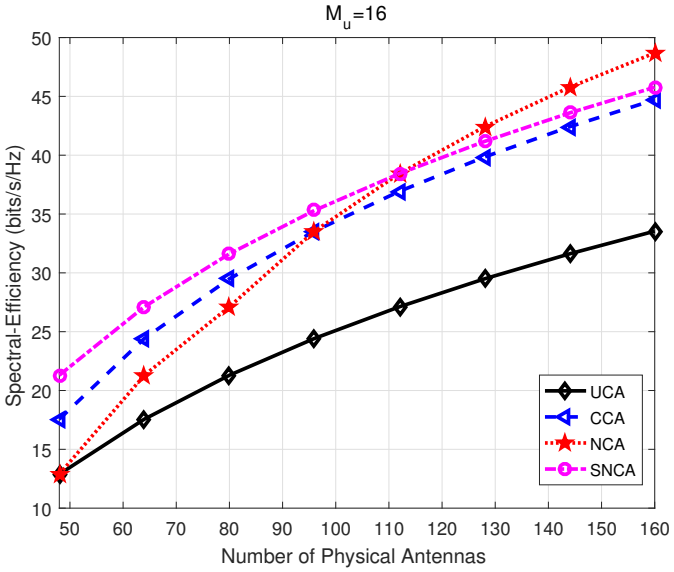

Figure 6.14. Spectral efficiency versus the number of physical BS antennas N_r when MRC is applied at the receiver. In this example, $K = 10$ and the numbers of antennas of UCA, CCA, NCA, SNCA are listed in Table 6.2. Averagely, the three structures of sparse cylindrical array, which are CCA, NCA and SNCA can increase the number of antennas of the UCA about 1.5 times .

CHAPTER 7

Conclusion and Future Works

In this chapter, the conclusion of this dissertation is presented and followed by is the future work.

7.1 Conclusion

This dissertation proposes several approaches of the sparse sampling and sparse arrays, meanwhile it also provides some applications of the proposed methods.

- Data Compression for UWB Radar and SAR[108]-[111]: In Chapter 2, two target detection algorithms in foliage environment are developed, which are NS-STFT approach and CS-STFT approach. Since nested sampling and co-prime sampling are sub-Nyquist sampling, the NS-STFT methods and CS-STFT method can save about half the quantity of the original data. In addition, the high redundant SAR raw data of the signal echoes is compressed by exploiting SVD-QR algorithm in slow-time domain of the data set before using backprojection image reconstruction method.
- Sensing with Application to Greenland Bed Elevation Assessment[112]: In Chapter 3, a new co-prime interpolation based compressive sensing algorithm is proposed. When the proposed algorithm is used, RMSE of the recovered image becomes lower and PSNR also gets improved. Furthermore, the CopCS has also been tested on real data – Greenland elevation map. The reconstructed images by CopCS approach are much clear than both interpolated images and direct CS recovered images.

- DoA Estimation in Underwater Sensor Networks Based on Stationary Sparse Array and Mobile Sparse Array[113][114]: In Chapter 4 and 5, we extend the augmented matrix approach from minimum redundancy array to 1D and 2D nested array and co-prime array in order to estimate the location of the targets. It's clear to see that the nested and co-prime arrays are able to save the number of sensors. Moreover, accuracy is improved for the reason of large apertures and CRB in the non-uniform array is also decreased significantly. For the co-prime array in motion, SDS method is proposed. The simulation results indicate that an array in motion by applying SDS method has a larger dynamic range than the static array and performs better than the uniform linear array.
- Evaluating Spatial Resolution and Channel Capacity of Sparse Cylindrical Arrays for Massive MIMO: In Chapter 6, three new sparse cylindrical arrays – co-prime cylindrical array, nested cylindrical array and sparse nested cylindrical array are proposed. Since beam pattern is related with the ability of resolution, we compare the performance of beam pattern among uniform cylindrical array and the two sparse cylindrical arrays. Simulation results prove our theoretical analysis, which is that CCA and NCA could achieve better performance with fewer elements comparing with uniform cylindrical array. Besides, we also analyze the the uplink channel capacity in massive MIMO scenario, when the three sparse cylindrical arrays are deployment at the base station. The results show that all the three sparse cylindrical arrays can improve the channel capacity compared with the uniform cylindrical array with same number of antennas.

7.2 Future Research

7.2.1 Sparse Cylindrical Arrays in Underwater Environment and Communication Networks

Cylindrical arrays have been used in several applications, including sonar, radar, and communication. Active sonars designed for detection of submarines and other objects located underwater and at sea bottoms are usually equipped with cylindrical arrays, allowing for simultaneous observation of targets at round angle. In fishery applications, the cylindrical sonar array is typically mounted below the hull of the vessel, to image the sea in a cone around the boat. In the future works, we want to apply sparse cylindrical arrays in underwater environment, in order to improve the performance of target detection.

In wireless communications, performance enhancements can be achieved by implementing an antenna array configuration that provides the capability of generating and electronically steering multiple high-resolution beam patterns over the entire coverage region in the azimuth plane as well as the elevation plane. Although a circular array antenna is a suitable choice to achieve such a task, it is more robust and efficient to consider a cylindrical array antenna. This is due to the fact that a cylindrical array antenna allows for the wide angular coverage in both the azimuth plane and the elevation plane. Furthermore, the cylindrical geometry of the antenna is attractive for achieving the capacity requirement of 5G communications. If we want to realization the sparse cylindrical antenna arrays in massive MIMO, more theoretical work has to do, such as considering the fading and channel modeling.

7.2.2 Multimodal Data Analysis Based on Sparse Sampling

Due to the rich characteristics of natural phenomena, it is rare that a single modality provides complete knowledge of the phenomenon of interest. In the 20th

century, the idea of data fusion was firstly laid in [115][116]. Since then, jointly analysis of multiple datasets have been studied for a long time. In [117], the authors provide an overview of multimodal data fusion. Some existing pattern recognition tools for multimodal data analysis and integration (MDAI) are as listed:

- Human-inspired pattern recognition
- Probabilistic reasoning
- Deep learning
- Bayesian approaches
- Graphical models
- High-dimensional regression
- Support vector machines
- Kernel methods
- Information theory

Motivation for data fusion are numerous, such as obtaining a global view of the environment, improving making decisions, security inspection or exploratory research. There're several challenges in data fusion [118][119], for example, the decision is usually depended on the data generated by different types (audio, visual and so on), as a consequence, there would be a large number of variables and samples which needs to be processed. In addition, with the development of the technology, the requirement on MDAI is increasing as well and sometimes it's desirable that the data fusion system could make accurate and real-time decisions. Introducing sparse sampling into multimodality may be an efficient approach to improve the performance of multimodal data fusion.

REFERENCES

[1] B. Ferrell, "Ultrawideband foliage penetration measurements," in *Proc. IEEE Nation Radar Conf*, pp. 80-84, Mar. 1994.

[2] X. Xu, and R. M. Narayanan, "FOPEN SAR imaging using UWB step-frequency and random noise waveforms," *IEEE Trans. Aerospace and Electronic Systems*, vol. 37, pp. 1287-1300, Oct. 2001.

[3] Q. Liang, S. W. Samn and X. Cheng, "UWB radar sensor networks for sense-through-foliage target detection," in *Proc. IEEE Int. Conf. Commun.*, pp. 2228-2232, May 2008.

[4] J. Liang and Q. Liang, "A differential based approach for sense-through-foliage target detection using UWB radar sensor networks," *Proc. IEEE Intl Conf. Comm.*, pp. 1952-1956, 2008.

[5] K. Strodl, U. Benz, F. Blaser, T. Eiting, and A. Moreira, "Comparison of several algorithms for on-board SAR raw data reduction," in *Proc. IGARSS94*, pp. 2197-2199, 1994.

[6] R. A. Baxter, "SAR image compression with the Gabor transform," *Trans. Geosci. Remote Sens.*, vol. 37, no.1, pp. 574-588, Jan. 1999.

[7] R. Baraniuk and P. Steeghsm, "Compressive radar imaging," *IEEE Radar Conference*, Waltham, Massachusetts, Apr. 2007.

[8] J. Chen, Q. Liang, J. Paden and P. Gogineni, "Compressive sensing analysis of synthetic aperture radar raw data," *IEEE Intl Conf. Comm.*, pp. 6362-6366, Jun. 2012.

[9] X. G. Xia, "On estimation of multiple frequencies in undersampled complex valued waveforms," *IEEE Trans. Signal Process*, vol. 17, no. 12, pp. 3417-3419, Dec. 1999.

[10] G. Li, J. Xu, Y. N. Peng and X. G. Xia, "Location and imaging of moving targets using nonuniform linear antenna array SAR," *IEEE Trans. Aerospace and Electronic Systems* vol. 43, no. 3, pp. 1214-1220, Jul. 2007.

[11] E. J. Cands and M. B. Wakin, "An Introduction To Compressive Sampling," *IEEE Signal Processing Magazing*, no. 2, pp. 21-30, Mar. 2008.

[12] D. Donoho, "Compressed Sensing," *IEEE Trans. Information Theory*, vol. 52, no. 4, pp. 1289-1306, Apr. 2006.

[13] M. A. Herman and T. Strohmer, "High-resolution radar via compressed sensing," *IEEE Trans. Signal Processing*, vol. 57, no. 6, pp. 2275-2284, Jun. 2009.

[14] G. Di Martino and A. Iodice, "Coprime Synthetic Aperture Radar (CopSAR): A New Acquisition Mode for Maritime Surveillance," *IEEE Trans. Geoscience and Remote Sensing*, vol. 53, no. 6, pp. 3110-3123, Jun. 2015.

[15] A. Moffet, "Minimum-redundancy linear arrays," *IEEE Trans. Antennas Propag.*, vol. 16, no. 6, pp. 172-175, Mar. 1968.

[16] P. Pal and P. P. Vaidyanathan, "Nested arrays: a novel approach to array processing with enhanced degrees of freedom," *IEEE Trans. Signal Process*, vol. 58, no. 8, pp. 4167-4181, Aug. 2010.

[17] P. P. Vaidyanathan and P. Pal, "Sparse sensing with co-prime samplers and arrays," *IEEE Trans. Signal Process*, vol. 59, no. 2, pp. 573-586, Feb. 2011.

[18] P. Pal and P. P. Vaidyanathan, "Nested arrays in two dimensions, Part II: Application in two dimensional array processing," *IEEE Trans. Signal Process*, vol. 60, no. 9, pp. 4706-4718, Sept. 2012.

[19] F. Harabi, A. Gharsallah and S. Marcos, "Three-dimensional antennas array for the estimation of direction of arrival," *Microwaves, Antennas and Propagation, IET*, vol. 3, no. 5, pp. 843-849, Aug. 2009.

[20] P. P. Vaidyanathan and P. Pal, "Theory of sparse coprime sensing in multiple dimensions," *IEEE Trans. Signal Process*, vol. 59, no. 8, pp. 3592-3608, Aug. 2011.

[21] Q. Liang, "Compressive sensing for synthetic aperture radar in fast-time and slow-time domains," *Proceedings of the IEEE*, pp. 1479-1483, Asilomar, 2011.

[22] Q. Liang and L. Wang, "Redundancy reduction in wireless sensor networks using SVD-QR," *IEEE Conference on Military Communications*, vol. 3, pp. 1857-1861, Oct. 2005.

[23] J. Liang and Q. Liang, "Channel selection in virtual MIMO wireless sensor networks," *IEEE Transactions on Vehicular Technology*, vol. 58, no. 5, pp. 2249-2257, Jun. 2009.

[24] G. H. Golub and C. F. Van Loan, "Matrix computations," Vol. 3. JHU Press, 2012.

[25] G. Golub, "Numerical methods for solving linear least squares problems," *Numerische Mathematik*, no. 3, pp. 206-216, 1965.

[26] C. Dill, "Foliage penetration (Phase II) field test: Narrowband versus wideband foliage penetration," *Final report of contract*, Jul. 2005.

[27] Q. Liang, "Radar sensor wireless channel modeling in foliage environment: UWB versus narrowband," *IEEE Sensors Journal*, no. 6, pp. 1448-1457, Jun. 2011.

[28] J. Liang, and Q. Liang, "Sense-Through-Foliage target detection using UWB radar sensor networks," *Pattern Recognit. Lett.*, vol. 31, no. 11, pp. 1412-1421, Aug. 2010.

[29] Q. Liang, B. Zhang and X. Wu, "UWB radar for target detection: DCT versus matched filter approaches," in *Proc. IEEE Global Telecommun. Conf. (Globecom)*, pp. 15, Dec. 2012.

[30] J. Liang, and Q. Liang, "UWB radar sensor networks detection of targets in foliage using short-time Fourier transform," *Proc. IEEE Intl Conf. Comm*, pp. 1-5, 2009.

[31] Barton, David Knox. Radar system analysis and modeling. Norwood, MA, USA: Artech House, 2005.

[32] C. Casteel, L. Gorham, M. Minardi, S. Scarborough, K. Naidu, and U. Majumder, "A challenge problem for 2D/3D imaging of targets from a volumetric data set in an urban environment," in *Proc. SPIEAlgorithms Synthetic Aperture Radar Imagery XIV*, vol. 6568, p. 65680D, 2007.

[33] [Online]. Available: https://en.wikipedia.org/wiki/Greenland_ice_sheet

[34] S. C. Park, M. K. Park, and M. G. Kang, "Super-resolution image reconstruction: a technical overview," *IEEE Signal Processing*, vol. 20, no. 3, pp. 2136, May 2003.

[35] T. Komatsu, K. Aizawa, T. Igarashi and T. Saito, "Signal-processing based method for acquiring very high resolution images with multiple cameras and its theoretical analysis," *IEEE Proc. Inst. Elec. Eng.*, vol. 140, no. 1, pp. 1925, Feb. 1993.

[36] S. H. Rhee and M. G. Kang, "Discrete cosine transform based regularized high-resolution image reconstruction algorithm," *Optical Engineering*, vol. 38, no. 8, pp. 13481356, Aug. 1999.

[37] R. H. Chan, T. F. Chan, L. Shen and Z. Shen, "Wavelet algorithms for high-resolution image reconstruction," *SIAM Journal on Scientific Computing*, vol. 24, no. 4, pp. 14081432, Feb. 2003.

[38] R. G. Hardie, K. J. Barnard and E. E. Armstrong, "Joint MAP registration and high-resolution image estimation using a sequence of undersampled images," *IEEE Trans. Image Processing*, vol. 6, no. 12, pp. 16211633, Dec. 1997.

[39] R. Y. Tsai and T. S. Huang, "Multiple frame image restoration and registration," *Advances in Computer Vision and Image Processing*, pp. 317339, Dec. 1984.

[40] R. E. Crochiere and L. R. Rabiner, "Interpolation and decimation of digital signalsA tutorial review," *IEEE Proc.*, vol. 69, no. 3, pp. 300331, Mar. 1981.

[41] M. Unser, A. Aldroubi and M. Eden, "Enlargement or reduction of digital images with minimum loss of information," *IEEE Trans. Image Processing*, vol. 4, no. 3, pp. 247258, Mar. 1995.

[42] A. M. Tekalp, M. K. Ozkan and M. I. Sezan, "High-resolution image reconstruction from lower-resolution image sequences and space-varying image restoration," *IEEE International Conference on Acoustics, Speech, and Signal Processing*, vol. 3, pp. 169172, Mar. 1992.

[43] R. G. Keys, "Cubic convolution interpolation for digital image processing," *IEEE Trans. Acoustics, Speech and Signal Processing*, vol.29, no.6, pp.1153-1160, Dec. 1981.

[44] X. Li and M. T. Orchard, "New edge-directed interpolation," *IEEE Trans. Image Processing*, vol.10, no.10, pp.1521-1527, Oct. 2001.

[45] R. E. Carlson and F. N. Fritsch, "Monotone piecewise bicubic interpolation," *SIAM journal on numerical analysis*, vol.22, no.2, pp.386-400, Apr. 1985.

[46] J. Ellenberg, "Fill in the Blanks: Using Math to Turn Lo-Res Datasets Into Hi-Res Samples," *Wired Magazine*, Feb. 2010.

[47] S. Chen, D. Donoho, and M. Saunders, "Atomic decomposition by basis pursuit," *SIAM J. Sci. Comput.*, vol. 20, pp. 3361, 1998.

[48] G. Davis, S. Mallat, and M. Avellaneda, "Greedy adaptive approximation," *J. Construct. Approx.*, vol. 12, pp. 5798, 1997.

[49] S. G. Mallat and Z. Zhang, "Matching pursuit with time-frequency dictionaries," *IEEE Trans. Signal Process*, vol.41, no.12, pp.3397-3415, Dec. 1993.

[50] Y. Pati, R. Rezaiifar and P. Krishnaprasad, "Orthogonal Matching Pursuit : recursive function approximation with application to wavelet decomposition," *IEEE Conference on Record of The Twenty-Seventh Asilomar*, vol.1, pp.40-44, Nov. 1993.

[51] M. A. T. Figueiredo, R. D. Nowak and S. J. Wright, "Gradient Projection for Sparse Reconstruction: Application to Compressed Sensing and Other Inverse Problems," *IEEE Journal of Selected Topics in Signal Processing*, vol. 1, no. 4, pp. 586-597, Dec. 2007.

[52] Q. Wu and Q. Liang, "Coprime sampling for nonstationary signal in radar signal processing," in *EURASIP Journal on Wireless Communications and Networking*, vol.2013, no.1, pp.1, 2013.

[53] E. J. Cands, "Compressive sampling," *Int. Congress of Mathematics*, vol.3, pp.1433-1452, Aug. 2006.

[54] J. L. Bamber, J. A. Griggs, R. T. W. L. Hurkmans, J. A. Dowdeswell, S. P. Gogineni, I. Howat, J. Mouginot et al, "A new bed elevation dataset for Greenland," *The Cryosphere*, vol.7, no.2, pp.499-510, Mar. 2013.

[55] [Online] https://www.cresis.ku.edu/content/research/field-programs/greenland

[56] R. O. Schmidt, "Multiple emitter location and signal parameter estimation," *IEEE Trans. Antennas and Propagation*, vol. 34, no. 3, pp. 276-280, Mar. 1986.

[57] B. Friedlander and A. J. Weiss, "Direction finding for wide-band signals using an interpolated array," *IEEE Trans. Signal Process*, vol. 41, no. 4, pp. 1618-1634, Apr. 1993.

[58] M. A. Doran, M. A. Doron and A. J. Weiss, "Coherent wide-band processing for arbitrary array geometry," *IEEE Trans. Signal Process*, vol. 41, no. 1, pp. 414, Jan. 1993.

[59] T. Pham, and B. M. Sadler, "Adaptive wideband aeroacoustic array processing," in *Proc. of the 8th IEEE Statistical Signal and Array Processing Workshop*, pp. 295-298, Jun. 1996.

[60] S. U. Pillai, Y. Bar-Ness and F. Haber, "A new approach to array geometry for improved spatial spectrum estimation," in *Proc. ICASSP*, pp. 15221524, Oct. 1985.

[61] P. Pal and P. P. Vaidyanathan, "Coprime sampling and the MUSIC algorithm," *IEEE Digital Signal Proc. Workshop*, Jan. 2011.

[62] Y. Ma and Y. H. Hu, "ML source localization theory in an underwater wireless sensor array network," *IEEE Wireless Communications, Networking and Mobile Computing (WiCom'09)*, 2009.

[63] S. U. Pillai and F. Haber, "Statistical analysis of a high resolution spatial spectrum estimator utilizing an augmented covariance matrix," *IEEE Trans. Acoustics Speech Signal Process*, vol. 35, no. 11, pp. 1517-1523, Nov. 1987.

[64] P. Stoica and N. Arye, "MUSIC, maximum likelihood, and Cramer-Rao bound," *IEEE Trans. Acoustics Speech Signal Process*, vol. 4, pp. 2296-2299, Apr. 1988.

[65] P. Pal and P. P. Vaidyanathan, "Nested arrays in two dimensions, part I: geometrical considerations," *IEEE Trans. Signal Process*, vol. 60, no. 9, pp. 4694-4705, Sept. 2012.

[66] H. L. Van Trees, "Detection, estimation, and modulation theory, optimum array processing," *John Wiley & Sons*, 2004.

[67] O. Lange and B. Yang, "Antenna geometry optimization for 2D direction-of-arrival estimation for radar imaging," *2011 International ITG Workshop on Smart Antennas (WSA)*, pp. 1,8, Feb. 2011.

[68] S. Stergiopoulos, A. C. Dhanantwari, and J. J. Grodski, "Implementation of adaptive processing in integrated active-passive sonars deploying cylindrical arrays," *IEEE Proc. of International Symposium in Underwater Technology*, pp. 289-294, Apr. 1998.

[69] N. Herscovici, Z. Sipus, and P.-S. Kildal, "The cylindrical omnidirectional patch antenna," *IEEE Trans. Antennas Propagat.*, vol. 49, pp. 1746-1753, Dec. 2001.

[70] M. G. Hussain, "Theory and analysis of adaptive cylindrical array antenna for ultrawideband wireless communications," *IEEE Trans. Wireless Comm.*, vol. 4, no. 6, pp. 3075-3038, Nov. 2005.

[71] R. Salamon, J. Marszal, and W. Lesniak, "Broadband sonar with a cylindrical antenna," *Acta Acustica united with Acustica*, vol. 92, no. 1, pp. 153-155, Jan. 2006.

[72] X. Lurton, *An introduction to underwater acoustics: principles and applications.* Springer Science and Business Media, 2002.

[73] N. C. Yen and W. Carey, "Application of syntheticaperture processing to towedarray data," *J. Acoust. Soc. A.*, vol. 86, no. 2, pp. 754-765, 1989.

[74] M. Karaman, P. C. Li and M. O'Donnell, "Synthetic aperture imaging for small scale systems," *IEEE Trans. Ultrasonics, Ferroelectrics, and Frequency Control*, no. 3, pp. 429-442, 1995.

[75] S. Stergiopoulos, "Implementation of adaptive and synthetic-aperture processing schemes in integrated active-passive sonar systems," *Proc. IEEE*, no. 2, pp. 358-398, 1998.

[76] Don H. Johnson, "The application of spectral estimation methods to bearing estimation problems," *Proc. IEEE*, vol. 70, pp. 1018-1028, 1982.

[77] N. Wu, and Q. Liang, "Underwater DoA estimation based on nested array," *IEEE MILCOM*, pp. 216-221, Oct. 2015.

[78] William F. Gabriel, "Spectral analysis and adaptive array superresolution techniques," *Proc. IEEE*, vol. 68, pp. 654-666, June 1980.

[79] A. Cantoni and L. C. Godara, "Resolving the directions of sources in a correlated field incident on an array," *J. Acoust. Soc. Am.*, vol. 70, pp. 1247-1255, Apr. 1980.

[80] F. Haber and M. Zoltowski, "Spatial spectrum estimation in a coherent signal environment using an array in motion," *IEEE Trans. Antennas and Propagation*, vol. 34, pp. 301-310, 1986.

[81] J. Ramirez, Jonathan Odom and Jeffrey Krolik, "Exploiting array motion for augmentation of co-prime arrays," *IEEE 8th In Sensor Array and Multichannel Signal Processing Workshop (SAM)*, pp. 525-528, 2014.

[82] J. Hoydis, S. ten Brink, and M. Debbah, "Massive MIMO: How many antennas do we need?," in *Proc. IEEE Annu. Allerton Conf. Commun.*, pp. 545-550, Sep. 2011.

[83] F. Rusek, D. Persson, B. D. Lau, E. G. Larsson, T. L. Marzetta O. Edfors, and F. Tufvesson, "Scaling up MIMO: Opportunities and challenges with very large arrays," *IEEE Signal Process. Mag.*, vol. 30, no. 1, pp. 40-69, Jan. 2013.

[84] L.Lu, G Y. Li, A L. Swindlehurst, A. Ashikhmin, and R. Zhang, "An overview of massive MIMO: Benefits and challenges," *IEEE J. Sel. Topics Signal Process.*, vol. 8, no. 5, pp. 742-758, Oct. 2014.

[85] E. G. Larsson, O. Edfors, F. Tufvesson, and T.-L. Marzetta, "Massive MIMO for next generation wireless systems," *IEEE Commun. Mag.*, vol. 52, no. 2, pp. 186-195, Feb. 2014.

[86] A. Pitarokoilis, S. K. Mohammed, and E. G. Larsson, "On the optimality of single-carrier transmission in large-scale antenna systems," in *IEEE Wireless Commun. Lett.*, vol. 1, no. 4, pp. 276279, Aug. 2012.

[87] T. L. Marzetta, "Noncooperative cellular wireless with unlimited numbers of base station antennas," in *IEEE Trans. Wireless Commun.*, vol. 9, no. 11, pp. 35903600, Nov. 2010.

[88] H. Q. Ngo, E. G. Larsson, and T L. Marzetta, "Energy and spectral efficiency of very large multiuser MIMO systems," *IEEE Trans. Commun.*, vol. 61, no. 4, pp. 1436-1449, Apr. 2013.

[89] A. Osseiran, F. Boccardi, V. Braun, K. Kusume, P. Marsch, M. Maternia, O. Queseth, M. Schellmann, H. Schotten, H. Taoka, and H. Tullberg, "Scenarios for 5G mobile and wireless communications: the vision of the METIS project," *IEEE Commun. Mag.*, vol. 52, no. 5, pp. 26-35, May 2014.

[90] C. X. Wang, F. Haider, X. Gao, X. H. You, Y. Yang, D. Yuan, H. Aggoune, H. Haas, S. Fletcher, and E. Hepsaydir, "Cellular architecture and key technologies for 5G wireless communication networks," *IEEE Commun. Mag.*, vol. 52, no. 2, pp. 122-130, Feb. 2014.

[91] Y. Han, Y. Chen, B. Wang, and K. R. Liu, "Time-Reversal Massive Multipath Effect: A Single-Antenna Massive MIMO Solution," *IEEE Trans. Commun.*, vol. 64, no. 8, pp. 3382-3394, Aug. 2016.

[92] X. Gao, F. Tufvesson, O. Edfors, and F. Rusek, "Measured propagation characteristics for very-large MIMO at 2.6 GHz," in *Proc. 46th ASILO-MAR*, pp. 295-299, Nov. 2012.

[93] X. Gao, O. Edfors, F. Rusek, and F. Tufvesson, "Massive MIMO performance evaluation based on measured propagation data," in *IEEE Trans. Wireless Commun.*, vol. 14, no. 7, pp. 3899-3911, Jul. 2015.

[94] J. Hoydis, C. Hoek, T. Wild, and S. ten Brink, "Channel measurements for large antenna arrays," in *IEEE Intl. Symp. Wireless Commun. Systems*, pp. 811-815, Aug. 2012.

[95] S. Hur, S. Baek, B. Kim, Y. Chang A. F. Molisch, T. S. Rappaport, K. Haneda, and J. Park, "Proposal on millimeter-wave channel modeling for 5G cellular system," *IEEE J. Sel. Topics Signal Process.*, vol. 10, no. 3, pp. 454-469, Apr. 2016.

[96] X. Gao, O. Edfors, F. Tufvesson, and E. G. Larsson, "Massive MIMO in real propagation environments: Do all antennas contribute equally?," in *IEEE Trans. Commun.*, vol. 63, no. 11, pp. 3917-3928, Nov. 2015.

[97] Z. Gao, L. Dai, C. Yuen, and Z. Wang, "Asymptotic orthogonality analysis of time-domain sparse massive MIMO channels," in *IEEE Commun. Lett.*, vol. 19, no. 10, pp. 1826-1829, Oct. 2015.

[98] X. Ge, R. Zi, H. Wang, J. Zhang, and M. Jo, "Multi-user massive MIMO communication systems based on irregular antenna arrays," in *IEEE Trans. Wireless Commun.*, vol. 15, no. 8, pp. 5287-5301, Aug. 2016.

[99] V. Voipio, and P. Vainikainen, "Narrowbeam cylindrical antenna array with sparse antenna spacing," *IEEE Vehicular Technology Conference*, vol. 48, no. 1, pp. 465-469, May 1998.

[100] F. Ademaj, M. Taranetz, and M. Rupp, "Evaluating the Spatial Resolution of 2D Antenna Arrays for Massive MIMO Transmissions," *??*, vol. 41, no. 4, pp. 1618-1634, Apr. 2016.

[101] T. E. Bogale, and L. B. Le, "Beamforming for multiuser massive MIMO systems: Digital versus hybrid analog-digital," in *Proc. IEEE GLOBECOM*, pp. 4066-4071, Dec. 2014.

[102] H. Huh, G. Caire, H. C. Papadopoulos, and S. A. Ramprashad, "Achieving" massive MIMO" spectral efficiency with a not-so-large number of antennas," *IEEE Trans. Wireless Commun.*, vol. 11, no. 9, pp. 3226-3239, Sept. 2012.

[103] Y. Zhu, L. Liu, A. Wang, K. Sayana, and J. C. Zhang, "DoA estimation and capacity analysis for 2D active massive MIMO systems," in *Proc. IEEE Int. Conf. Commun. (ICC)*, pp. 4630-4634, Jun. 2013.

[104] R. Shafin, L. Liu, J. Zhang, and Y. C. Wu, "DoA Estimation and Capacity Analysis for 3-D Millimeter Wave Massive-MIMO/FD-MIMO OFDM Systems," *IEEE Trans. Wireless Commun.*, vol. 15, no. 10, pp. 6963-6978, Oct. 2016.

[105] B. Friedlander, and A. J. Weiss, "Direction finding for wide-band signals using an interpolated array," *IEEE Trans. Signal Process.*, vol.41, no.4, pp.1618-1634, Apr. 1993.

[106] K. Adhikari, J. R. Buck, and K. E. Wage, "Extending coprime sensor arrays to achieve the peak side lobe height of a full uniform linear array," *EURASIP J. Adv. Signal Process.*, vol. 2014, no. 1, pp. 3592-3608, Sep. 2014.

[107] K. Adhikari, J. R. Buck, and K. E. Wage, "Beamforming with extended co-prime sensor arrays," in *Proc. IEEE Int. Conf. Acoust., Speech, Signal Process.*, pp. 4183-4186, May 2013.

[108] N, Wu, and Q. Liang, "Nested sparse sampling and co-prime sampling in sense-through-foliage target detection," *Physical Communication*, vol.13, pp. 230-238, Dec. 2014.

[109] N, Wu, and Q. Liang, "An Improved STFT Approach in Foliage Target Detection of UWB Radar Sensor Networks," *Proceedings of the 2015 International*

Conference on Communications, Signal Processing, and Systems, pp. 181-191, Dec. 2016.

[110] N, Wu, and Q. Liang, "Raw Data Reduction for Synthetic Aperture based on SVD-QR," *Proceedings of the 2015 International Conference on Communications, Signal Processing, and Systems*, pp. 507-520, Dec. 2016.

[111] N, Wu, and Q. Liang, "Data Compression for Synthetic Aperture Radar and Resolution Improvement," *IEEE Digital Signal Processing (DSP)*, pp. 227-231, Oct. 2016.

[112] N, Wu, and Q. Liang, "Greenland Bed Elevation Resolution Improvement via Compressive Sensing and Co-prime Up-sampling," *IEEE in Military Communications Conference (MILCOM)*, pp. 729-734, Nov. 2016.

[113] N, Wu, and Q. Liang, "Underwater DoA Estimation Based on Nested Array," *IEEE in Military Communications Conference (MILCOM)*, pp. 216-221, Oct. 2015.

[114] N, Wu, and Q. Liang, "Underwater Mobile Co-prime Sensor Array for Angle of Arrival Estimation Base on Space-Domain Sensor Synthesis," *IEEE in Computer Communications Workshops (INFOCOM)*, pp. 630-635, Apr. 2016.

[115] H. Hotelling, "Relations between two sets of variates," *Biometrika*, vol. 28, no. 3/4, pp. 321-377, Dec. 1936.

[116] R. B. Cattell, " Parallel proportional profiles and other principles for determining the choice of factors by rotation," *Psychometrika*, vol. 9, no. 4, pp. 267-283, Dec. 1944.

[117] D. Lahat, T. Adali, and C. Jutten, " Multimodal data fusion: an overview of methods, challenges, and prospects," *Psychometrika*, vol. 103, no. 9, pp. 1449-1477, Sep. 2015.

[118] I. Van. Mechelen, and A. K. Smilde, " A generic linked-mode decomposition model for data fusion," *Psychometrika*, vol. 104, no. 1, pp. 83-94, Nov. 2010.

[119] B. Khaleghi, A. Khamis, F. O. Karray, and S. N. Razavi, " Multisensor data fusion: A review of the state-of-the-art," *Information Fusion*, vol. 14, no. 1, pp. 28-44, Jan. 2013

BIOGRAPHICAL STATEMENT

Na Wu received her B.S. degree from University of Electronic Science and Technology of China, China, in 2012. From 2013, she worked toward the Ph.D. degree at the University of Texas at Arlington and earned the Ph.D. degree in Electrical Engineering at the Department of Electrical Engineering, University of Texas, Arlington, in 2017. Her research interests include radar signal processing, compressive sensing, wireless communications and array signal processing.